



Dottorato di Ricerca in Fisica

Ciclo XXXVI

*Organic Field-Effect Transistors Based on Organic
Semiconductor-Polymer Blends for X-Ray Detection*

Elisabetta Colantoni

Candidate

Signature

Dr. Paolo Branchini

Advisor

Signature

Dr. Luca Tortora

Co-advisor

Signature

Prof. Giorgio Matt

Ph.D. Coordinator

Signature



Ph.D. in Physics
36th Cycle

Ph.D. Thesis

Organic Field-Effect Transistors Based on Organic
Semiconductor-Polymer Blends for X-Ray Detection

Ph.D. candidate: Elisabetta Colantoni

Advisers: Dr. Paolo Branchini
Dr. Luca Tortora

Non più le foglie ma scrosciar la sabbia

Abstract

In the last few years, the study of Organic Field-Effect Transistors (OFETs) has become ever more important. The OFETs characteristics provide the opportunity to create flexible, cost-effective, and biocompatible electronic devices. This work was focused on the technique of molecular contact doping and the employment of Organic Semiconductors (OSCs) materials in X-ray detectors, determining a significant advancement in OFETs technology.

In the first part of this study, the efficiency of molecular contact doping to reduce the contact resistance in OFETs, was explored. A dopant layer was inserted between the OSC and the top gold contacts, to lower the energy barrier for charge injection/release. The main challenge of molecular contact doping is the proper diffusion of the dopant towards the OFETs channel over time, which could affect the device's switching capability. Applying a solution shearing technique, it was demonstrated that the insertion of a p-dopant layer significantly improves the device's performance. It was proven that dopant diffusion can be controlled by blending the OSC with polymers of different molecular weights. In addition, studies conducted employing comprehensive electrical characterization and Time-of-Flight Secondary Ion Mass Spectrometry (ToF-SIMS) confirmed that in films with high-molecular-weight polymer, the dopant remains confined into the contact areas, providing an enhanced long-term stability of the devices.

The second part of the research was focused on the application of OSCs materials in X-ray detectors. The construction of high-performance OFETs was realized by blending OSCs with a polymer. These films, printed using a low-cost and high-throughput deposition technique, exhibit remarkable electrical characteristics, including high mobility and a low density of hole traps. This could be a consequence of the advantageous herringbone packing and the vertical phase separation of the polymer in the blend films, as demonstrated by ToF-SIMS depth profiling studies. Remarkably, these devices demonstrate an exceptional sensitivity for X-ray detection, overtaking most of the existing perovskite film-based detectors. As a proof of concept, an X-ray image with a sub-millimeter pixel size is recorded using a 4-pixel array, highlighting the potential of these OFETs in medical dosimetry and diagnostic imaging.

Contents

Acronyms	vii
Introduction	1
1 Organic Electronics	5
1.1 Brief History of Organic Electronics	5
1.2 Organic Semiconductors	8
1.2.1 Atomic and Molecular Orbitals	9
1.2.2 Hybridization	10
1.2.3 Electronic Structure of Conjugated Units	12
1.2.4 Charge Transport	13
1.3 Organic Semiconductor Materials	16
1.3.1 Organic Semiconductor Deposition Techniques	18
1.4 Doping of Organic Semiconductor	20
1.4.1 Mechanisms of Doping	20
1.5 Organic Field-Effect Transistors (OFETs)	25
1.5.1 Operation Principle	27
1.5.2 OFETs in Sensing Applications	33
1.5.3 Objectives	37
2 Low Energy Ion Beam Analysis on Thin Film Devices	39
2.1 General Principles	39
2.2 Ion-Solid Interaction	41
2.2.1 Scattering Cross Section	43
2.2.2 Emission Phenomena	44
2.2.3 Secondary Ion Formation	45
2.3 Secondary Ions Detection and Analysis	47
2.4 Instrumental Setup	47

2.4.1	Primary Ion Beam Column	49
2.4.2	Dual-Source Ion Column	51
2.4.3	Electron Flood Gun	52
2.4.4	Analyzer	52
2.5	ToF-SIMS Analysis Mode	54
2.5.1	Static SIMS	54
2.5.2	Dynamic SIMS: Depth-Profiling	56
2.5.3	ToF-SIMS Analysis of Thin Film Devices	57
3	Molecular Contact Doping Effects in OSCs	61
3.1	Introduction and Objectives	61
3.2	Device Fabrication	65
3.3	Thin Films Characterization	66
3.4	Electrical Characterization	69
3.5	Chemical Characterization	76
3.6	Conclusions: The Impact of Polystyrene in Inhibiting Dopant Diffusion	82
4	Evaluation of Blended and Non-Blended Thin Films	85
4.1	Introduction and Objectives	85
4.2	Device Fabrication	86
4.3	Thin Films Characterization	87
4.4	Electrical Characterization	91
4.5	Chemical Characterization	95
4.6	X-Ray Detection	97
4.7	Conclusions: Role of Vertical Phase Segregation on Performance and Stability	101
5	Optimization of PS Concentration and PS Molecular Weight in Blended Thin Films	103
5.1	Ionizing Radiation Detectors	103
5.1.1	Detectors Based on Thin Films Organic Semiconductors	105
5.1.2	Photoconductive Gain Effect	107
5.2	Device Fabrication	109
5.3	Thin Films Characterization	110
5.4	Electrical Characterization	112
5.5	Chemical Characterization	118
5.6	X-ray Detection	122
5.7	Conclusions: PS Role for High X-Ray Sensitivity	123

Contents	vii
Conclusions	125
Bibliography	129

Acronyms

AFM Atomic Force Microscopy.

AOs Atomic Orbitals.

BAMS Bar-Assisted Meniscus Shearing.

BGBC Bottom-Gate Bottom-Contact.

BGTC Bottom-Gate Top-Contact.

BTBT benzothieno[3,2-b][1]benzothiophene.

C₈-BTBT-C₈ 2,7-dioctyl[1]benzothieno[3,2-b][1]benzothiophene.

CB Conduction Band.

CPX Charge Transfer complex.

DC Direct Current.

DFT Density Functional Theory.

EA Electron Affinity.

EG-OFET Electrolyte-Gated Organic Field-Effect Transistors.

ETL Electron-Transporting Layer.

F4TCNQ 2,3,5,6-tetrafluoro-7,7,8,8-tetracyanoquinodimethane.

HMWPS High-Molecular-Weight Polystyrene.

HOMO Highest Occupied Molecular Orbital.

HTL Hole-Transporting Layer.

IEs Ionization Energies.

IPA Ion Pair.

LCAOs Linear Combination of Atomic Orbitals.

LMIG Liquid Metal Ion Gun.

LMWPS Low-Molecular-Weight Polystyrene.

LUMO Lowest Unoccupied Molecular Orbital.

MOs Molecular Orbitals.

MOSFETs Metal-Oxide-Semiconductor Field-Effect Transistors.

MVA Multivariate Analysis.

OEs Organic Electronics.

OFETs Organic Field-Effect Transistors.

OLEDs Organic Light-Emitted Diodes.

OSCs Organic Semiconductors.

PCA Principal Component Analysis.

PFBT 2,3,4,5,6-pentafluorothiophenol.

PS Polystyrene.

PVD Physical Vapor Deposition.

R_C Contact Resistance.

RMS Root Mean Square.

SAMs Self-Assembled Monolayers.

SIMS Secondary Ion Mass Spectrometry.

SS Subthreshold Swing.

TCNQ Tetracyanoquinodimethane.

TGBC Top-Gate Bottom-Contact.

TGTC Top-Gate Top-Contact.

TIPS 6,13-bis(triisopropylsilylethynyl)pentacene.

TMTES 1,4,8,11-Tetramethyl-6,13-triethylsilylethynylpentacene.

TOF Time-of-Flight.

TOF-SIMS Time-of-Flight Secondary Ion Mass Spectrometry.

UHV Ultra-High Vacuum.

VB Valence Band.

VSEPR Valence-Shell Electron-Pair Repulsion.

XRD X-Ray Diffraction.

Introduction

In recent years, Organic Field-Effect Transistors (OFETs) have received considerable scientific attention for their properties and potential applications, making them key elements in the study of Organic Electronics (OEs).

The flexible nature of organic materials used in OFETs offers several advantages when compared with traditional inorganic semiconductors. This flexibility enables the fabrication of bendable and foldable electronic devices and opens up new possibilities in the field of wearable electronics and flexible displays. Such advancements are particularly relevant in an era where the demand for portable and lightweight electronics is continuously rising.

Furthermore, the low-temperature processing of OFETs, typically involving solution-based techniques, makes them compatible with a wide range of substrates, including plastics. This compatibility allows for cost-effective and large-scale production, making OFETs an economically attractive option for a variety of applications.

Moreover, the tunability of Organic Semiconductors (OSCs), at the molecular level, offers immense opportunities for customization. Researchers can modify the chemical structure of these materials to tailor the electronic properties, such as charge carrier mobility, threshold voltage, and stability. This level of control is fundamental for the development of OFETs in specific applications.

The environmental aspect is also really important. Organic materials are considered biocompatible and eco-sustainable compared to traditional semiconductor materials, which can contain toxic elements. The potential development of biodegradable or recyclable electronics using OFETs deals well with the growing environmental concerns and with more sustainable technology.

The performance of OFETs depends on several factors, such as the choice of organic semiconductors, dielectric materials, device geometry, and processing conditions. Therefore, a deep understanding of the underlying physics and chemistry of organic materials and interfaces is essential for the design and optimization of OFETs.

In this work, I focused my research on the study of p-type OFETs based on OSCs, with a particular emphasis on molecular contact doping and on the blending of OSCs with polymers to achieve stable and working devices over time.

The study is structured across five chapters, each chapter addresses a specific scientific aspect and contributes to the overall understanding of OFETs technology.

Chapter 1: Organic Electronics This chapter provides a comprehensive introduction to OEs, with a particular focus on the employment of OSCs. Charge transport mechanisms and the main deposition techniques, implemented for thin-film transistors construction, are discussed. Additionally, the operation characteristics and non-idealities of these devices are examined, laying the foundation for the understanding of the complexities of OFETs.

Chapter 2: Low Energy Ion Beam Analysis on Thin Film Devices This chapter explains the utilization of the Time-of-Flight Secondary Ion Mass Spectrometry (TOF-SIMS) technique for thin film devices. The significance of TOF-SIMS in characterizing thin films is explained, highlighting TOF-SIMS role in the progressive understanding of material properties and device structures.

Chapter 3: Molecular Contact Doping Effects in OSCs The experimental results of this work, related to molecular contact doping in OFETs, are presented. Optimization of molecular doping techniques is explored to enhance the device performance and to address one of the key challenges in organic electronics.

Chapter 4: Evaluation of Blended and Non-Blended Thin Films Focusing on the comparison between blended and non-blended films, this chapter emphasizes the key role of PS in the devices. It investigates how the incorporation of PS affects the overall performance and stability of the OFETs, providing insights into the benefits of blending OSCs with polymer materials.

Chapter 5: Optimization of PS Concentration and PS Molecular Weight in Blended Thin Films Starting from the outcome of the previous chapter, the final chapter extends the research to the implementation of these devices as detectors for ionizing radiation. This chapter explores the potential modifications and optimizations required to make OFETs suitable for high-energy radiation detection, opening new opportunities for the application of organic electronic devices also as biomedical sensors.

This research has been conducted primarily at the LASR3 laboratory, part of the Department of Physics at Roma Tre University, under the supervision of Dr. Paolo Branchini and Dr. Luca Tortora, in close cooperation with several international research groups.

In particular, I have had the opportunity to collaborate with esteemed researchers in this field. Notably, I worked closely with Prof. Marta Mas-Torrent at the Institut de Ciència de Materials de Barcelona (ICMAB) in Spain, as well as with Prof. Beatrice Fraboni and Dr. Laura Basiricò at the Department of Physics and Astronomy of the University of Bologna. These collaborations have been crucial in strengthening and broadening my knowledge and experience in the field of organic electronics and my future perspective.

A significant part of this research involved a five-month period in Barcelona at the ICMAB, under the supervision of Dr. Mas-Torrent. This period was particularly formative and constructive from a professional point of view.

1

Organic Electronics

This chapter provides an introduction to Organic Electronics (OEs), highlighting fundamental concepts of Organic Semiconductors (OSCs) with an overview of the principal mechanisms of Organic Field-Effect Transistors (OFETs). A brief review of Organic Electronics and Organic Semiconductors is included, outlining the improvement and development of OEs, analyzing the electrical architecture and charge transport dynamics inherent to OSCs, and detailing the materials constituting OSCs as well as the methodologies employed in their solution-based processing.

Then OFETs structural design, functional principles, and key electrical properties are explored. Considering that OFETs are a significant promise as innovative sensing platforms, at the end of the chapter a brief account of the status of art and the application in the realm of sensors is provided, introducing the objectives that this work wants to achieve.

1.1 Brief History of Organic Electronics

In 1947, John Bardeen, Walter H. Brattain, and William Shockley of Bell Laboratories developed the first transistor using germanium as the semiconductor material [1]. This germanium-based transistor is recognized as a key invention of the 20th century: for their contributions to the field of semiconductors and the invention of the transistor they received the Nobel Prize in Physics in 1956. Not long after germanium's introduction, silicon replaced germanium in transistor technology (Morris Tannenbaum in 1954 [2]), attracting a lot of interest from both the academic and industrial sectors.

Today, the main semiconductor material for transistors is silicon, serving as the fundamental building block for a variety of electronic devices, ranging from simple ones, like electronic timers, to more complex devices such as computers and mobile phones. However, the concerns associated with inorganic semiconductor technologies (high production costs and environmental impact) require the research of alternative materials and technologies [3].

Additionally, the demand for more flexible and lightweight materials has also limited the application of traditional silicon technology in conformable electronics [4].

As a consequence, the interest in OSCs and the associated field of OEs has greatly increased. Research on semiconductor-based technologies has employed the application of various organic materials. Organic materials, whether natural or synthetic, primarily contain carbon atoms bonded with various other elements including hydrogen, nitrogen, phosphorus, oxygen, sulfur, and occasionally, metals. These materials exhibit a range of mechanical, electrical, and optical properties, making them suitable for numerous applications in semiconductor technology.

In the field of Organic Electronics, several significant improvements are worth to be mentioned. In the 1950s, polycyclic aromatic compounds were discovered; these compounds form (with halogens) complex salts able to act as semiconducting charge transfer [5]. In 1973, Anderson and colleagues noted the presence of metallic conductivity in the organic metal complex tetrathiafulvalene-tetracyanoquinodimethane (TTF-TCNQ) [6]. A significant milestone was achieved in 1977 when controlled doping of a synthetic conjugated polymer was successfully demonstrated by Alan J. Heeger, Alan G. MacDiarmid, and Hideki Shirakawa [7]. Their innovative work demonstrated that organic semiconductors and conductors could function as electrically active materials, promoting the development of organic electronics. In 2000, for this innovative work and their pioneering efforts in the development of conductive polymers, they got the Nobel Prize in Chemistry [8].

The domain of OEs includes devices that employ organic materials as active components. Organic Semiconductors, in particular, have found applications in various devices, including Organic Light-Emitted Diodes (OLEDs) [9], Organic Solar Cells [10], and Organic Field-Effect Transistors (OFETs) [11].

OLEDs, for instance, are diodes designed to convert current directly into visible light. They are typically constructed with an organic active layer situated between two electrodes, one of which is transparent to permit light emission. The operational principle of OLEDs is based on the recombination of injected holes and electrons to produce excitons, which subsequently decay, emitting light as they revert to the ground states. The first OLEDs, realized by Tang and al. in 1987 [12], had a bilayer structure with an Electron-Transporting Layer (ETL) and a Hole-Transporting Layer (HTL), as shown in **Fig. 1.1a**. By selecting appropriate organic semiconductors, the color of emitted light can be controlled, offering several options such as red, green, and blue [13].

This technological innovation underwent significant improvement, culminating with the introduction of products like RGB digital displays into the commercial market. These displays rely on the use of three distinct OLEDs for each pixel to achieve the desired color

contrast, establishing them as a staple in contemporary technology. Furthermore, the recent unveiling of flexible smartphones, **Fig. 1.1b**, underscores the increasing incorporation and significance of flexible electronics in our everyday lives, highlighting the ongoing evolution and the potential of organic electronics in the modern era.

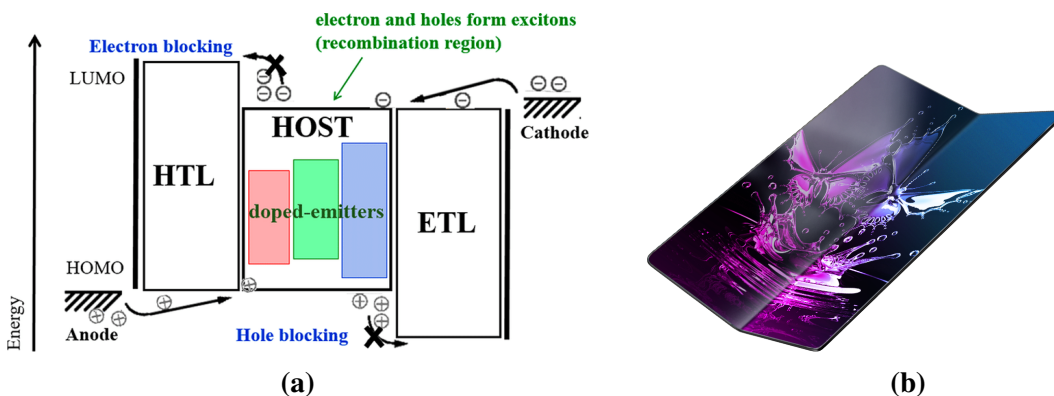


Figure 1.1 (a) Schematic energy level diagram for OLEDs devices [14]. (b) Flexible OLEDs displays. The image was taken from the website of Samsung (<https://oledera.samsungdisplay.com/eng/flex-oled/>).

The operating principle of organic solar cells is the opposite of the OLEDs ones: OLEDs convert electrical energy into light, while OSCs are engineered to transform light into Direct Current (DC). These devices incorporate an organic active layer nestled between two electrodes, with at least one transparent layer to allow the passage of visible light. The operational mechanism of organic solar cells can be delineated into five crucial stages, as depicted in **Fig. 1.2a**: firstly, the capture of photons and generation of excitons; secondly, the diffusion of excitons towards the donor/acceptor interface; thirdly, the dissociation of excitons at this interface; followed by the diffusion of carriers towards the respective electrodes; and finally, the collection of carriers by these electrodes [15].

While organic solar cells have demonstrated promising power conversion efficiency, currently peaking at around 17% [16], their market presence is yet to be established (a prototype is shown in **Fig. 1.2b**). One of the weaknesses of the commercial rollout is the short operational lifetime. The potential and efficiency observed in organic solar cells need further exploration and lifetime enhancement to make them potential competitors in the market of solar energy devices.

Organic Field-Effect Transistors (OFETs) represents another significant category of Organic Electronics devices. Within this device, the current flowing between the source and drain electrodes is effectively regulated by a third electrode, known as the gate through the mechanism of field effect; further details will be reported in the next sections. The origin of the first thiophene polymer-based OFETs can be traced back to the work of Tsumura et al. in

1986 [17]. OFETs permit the integration into flat panel displays employing flexible matrix elements and complementary circuits. These aspects are essential when applications have to cover extensive areas and production cost-effectiveness has to be considered.

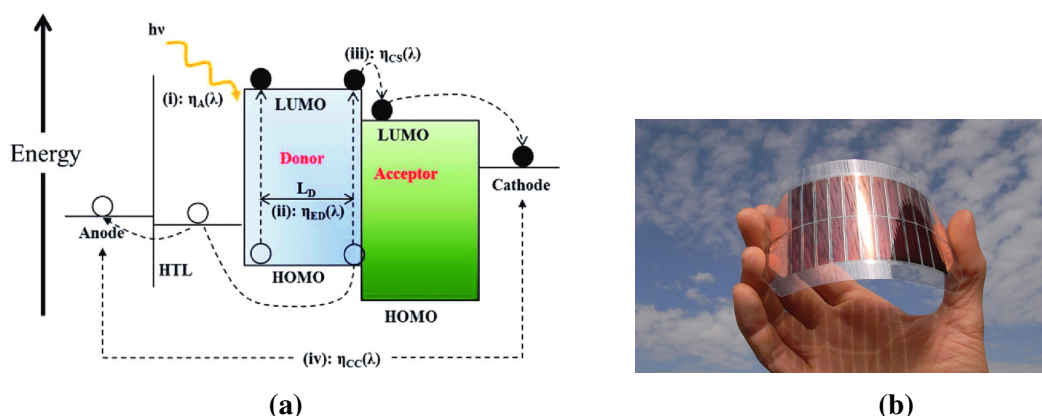


Figure 1.2 (a) Schematic energy level diagram for organic solar cells devices [15]. (b) Flexible organic solar cells. The image was taken from (<https://www.ise.fraunhofer.de/en/business-areas/photovoltaics/perovskite-and-organic-photovoltaics/organic-solar-cells-and-modules.html>).

Furthermore, OFETs find applications in various domains, including small integrated circuits, radio frequency identification tags, and devices that detect chemical and pressure variations. The research landscape in organic electronics also encompasses organic spin valves and organic lasers. Organic spin valves leverage the prolonged spin relaxation time of Organic Semiconductors (OSCs) due to their weak spin-orbit interaction, setting them apart from their inorganic counterparts. On the other hand, organic lasers take advantage of the high optical gain, intrinsic to the organic materials.

Currently, organic electronics continues to be of great interest within the research community, with several objectives: the design and synthesis of novel organic materials to enhance their solubility and electrical properties, the development of innovative deposition techniques to facilitate large-scale manufacturing, the improvement of device stability, and the exploration of new geometric and structural designs to promote the development of new applications.

1.2 Organic Semiconductors

Organic Semiconductors (OSCs) have got a lot of interest due to their complex electronic attributes and promising applications in a wide array of OEs applications. These compounds, primarily constructed of carbon-based molecules or polymers, exhibit the inherent flexibility

and adaptability characteristics of organic materials. Serving as a unique class of materials, OSCs efficiently integrate the electronic advantages found in semiconductors with the chemical and mechanical benefits typical of organic compounds, such as plastics. This resulted in a material with the capacity for light absorption, conduction of electricity, and light emission, with a structure that can be easily modified through chemical synthesis. The modifications enable the tailoring of their electronic properties, including the adjusting of the emission wavelengths and the solubility enhancement, facilitating the creation of thin films that are not only resilient, lightweight, and flexible but also easily tailored to specific needs. With these distinctive characteristics, OSCs are not only versatile but also ideal for crafting various semiconductor applications, including but not limited to displays, light panels, and solar cells [18].

1.2.1 Atomic and Molecular Orbitals

Atoms, the fundamental units of matter, have a structure with a positively charged nucleus, surrounded by a cloud of negatively charged electrons. The solutions of the Schrödinger equation for an atom give the wave function of the electrons in the atom. So, in accordance with quantum mechanics, electrons are represented by wave function $\psi(\vec{r}, t)$, and $|\psi(\vec{r}, t)|^2$ which represents the probability to find the electron at location \vec{r} at the time t . These wave functions define Atomic Orbitals (AOs), characterized by three quantum numbers: n , l , and m .

The principal quantum number (n) represents the main energy level of an electron within an atom, essentially determining the electron's energy and the distance from the nucleus. The azimuthal quantum number (l), also known as the angular momentum quantum number, defines the shape of the AOs. The value of l ranges is $[0, n - 1]$. Each value of l corresponds to a particular type of orbital: $l = 0$ represents s-orbitals, $l = 1$ corresponds to p-orbitals, and so on. The magnetic quantum number (m) indicates the orientation of the AOs in space. It can take integer values in the range $[-l, +l]$. The different values of m for a given l correspond to the different orientations that an AOs of a given shape can have. The s and p orbitals, representing angular momentum values of 0 and 1 respectively, have distinct shapes, with the s-orbital being spherical and p-orbitals exhibiting a dumbbell shape.

As atoms approach each other, their AOs overlap to form Molecular Orbitals (MOs), the behavior of electrons within these orbitals can be described using mathematical functions. The theory of MOs provides a quantitative description of the energetic structure of organic semiconductors [19]. According to this theory, the orbitals of a complex molecule can be described as a linear combination of the AOs corresponding to the single constituents. This approach is known as Linear Combination of Atomic Orbitals (LCAOs) and provides

mathematical calculations regarding the energetic structure of molecular systems [20]. This method identifies two categories of energy levels: the bonding and anti-bonding that together form a band-like structure. The occupied levels form the Highest Occupied Molecular Orbital (HOMO), while the unoccupied levels form the Lowest Unoccupied Molecular Orbital (LUMO). These represent respectively the outer shell occupied by electrons (analogous to the Valence Band (VB)) and the lowest energy level unoccupied (corresponding to the Conduction Band (CB)). The energy difference between the HOMO and LUMO represents the Energy Gap (E_G). For instance, in hydrogen, the MOs comprises bonding and antibonding orbitals with energy levels lower and higher than the original AOs, respectively as shown in **Fig. 1.3**.

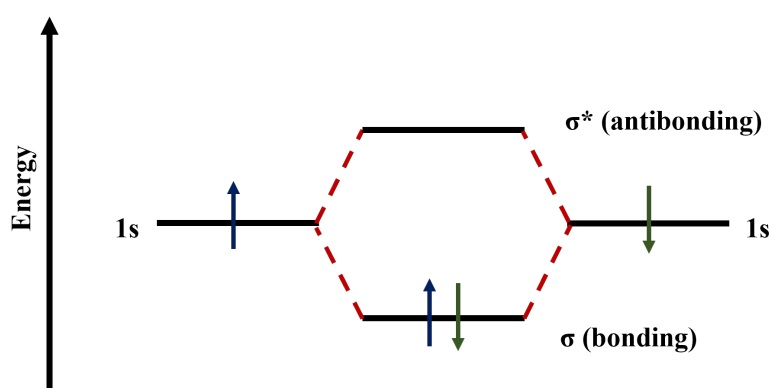


Figure 1.3 Formation of bonding and antibonding MOs in hydrogen.

1.2.2 Hybridization

Carbon, the basis of organic chemistry, has a ground state with two unpaired electrons available for forming bonds. However, traditional valence bond theory fails to predict even the simplest hydrocarbon compound (i.e. CH_4 , methane). In 1931, Linus Pauling introduced orbital hybridization to address this aspect, elucidating the molecular geometry of carbon compounds [21]. Through hybridization, atomic orbitals combine to form hybrid orbitals: this perfectly explains the tetrahedral structure of methane (CH_4). According to Valence-Shell Electron-Pair Repulsion (VSEPR) model, carbon can form three different types of hybrid orbitals: sp , sp^2 , and sp^3 , which are the combinations of s and p orbitals (**Fig. 1.4**). For example, in sp^2 hybridization, the $2s$ orbital combines with two of the $2p$ orbitals, forming three hybrid sp^2 orbitals that lie in the XY plane, while the fourth unhybridized orbital (in this case, $2p_z$) is orthogonal to the XY plane. The hybridization model is crucial for understanding the structures of various organic compounds (**Fig. 1.4**), such as ethylene (C_2H_4) and acetylene (C_2H_2): these compounds show specific bonding and

electron delocalization characteristics that influence their energy gaps and, consequently, their electronic and optical properties.

When two sp^2 -hybridized carbon atoms are in proximity, two different types of chemical bonds can be made, as shown in **Fig. 1.4**. The overlap between two sp^2 orbitals leads to a covalent bond called a σ -bond, formed along the line joining the two carbon atoms' nuclei. The partial overlap between the two unhybridized $2p_z$ orbitals forms another type of covalent bond called a π -bond. The σ -bond is much stronger than the π -bond due to the bigger overlapping between the two sp^2 orbitals compared to the two unhybridized $2p_z$ orbitals.

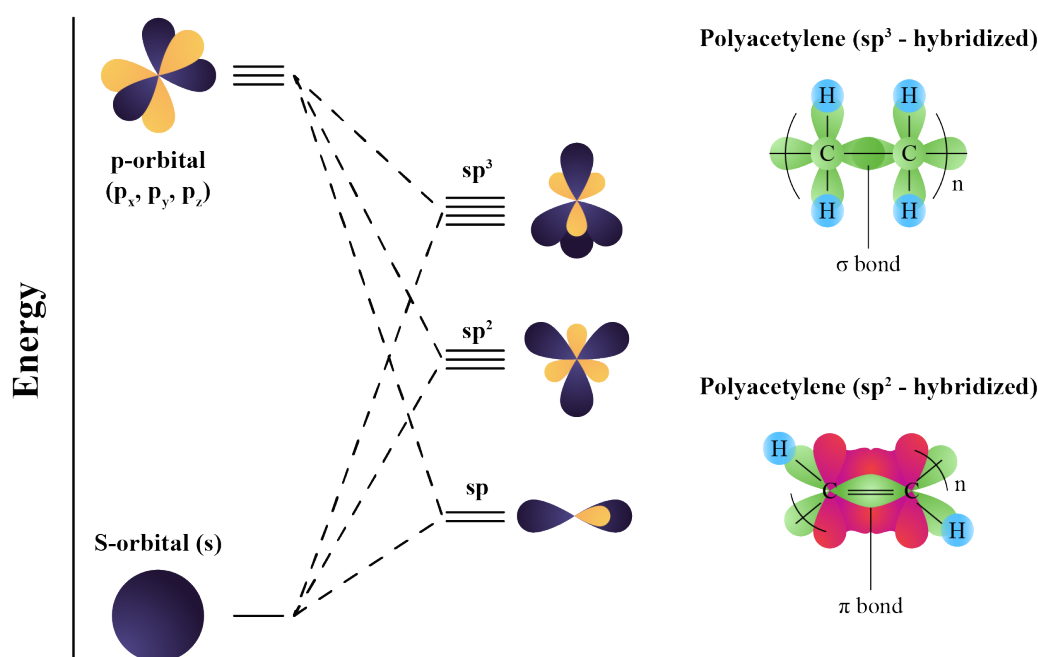


Figure 1.4 Schematic representation of orbital hybridization structures – sp (linear), sp^2 (trigonal planar) and sp^3 (tetrahedral) – and polymer examples for the sp^2 and sp^3 hybrid orbitals. Adapted from [22].

This aspect has significant implications for the electrical behavior of organic molecules. The σ -electrons, involved in the σ -bond, are too localized to be free to move, while the π -electrons, involved in the π -bond, are much more delocalized. As a result, the σ -electrons form the skeleton of the molecules, while the π -electrons are free to move across the molecule and contribute to the electrical properties of the material. OSCs consist of a repetition of conjugated units where single and double π -bonds alternate. The length of the π -conjugated systems determines whether the organic semiconductor is a small molecule or a polymer. Small molecules have a well-defined molecular weight, while polymers are long-chain molecules consisting of an indeterminate number of molecular repeating units. Despite this

difference, these compounds share more similarities than differences, especially in terms of optical and electrical properties.

1.2.3 Electronic Structure of Conjugated Units

A conjugated molecule is characterized by a chain alternating single and double bonds between carbon atoms. Take polyacetylene ($[\text{C}_2\text{H}_2]_n$), as a straightforward example of a conjugated polymer. In this structure, every carbon atom undergoes sp^2 hybridization, bonding with three other atoms as depicted in **Fig. 1.5**. The carbon atoms' non-hybridized p-orbitals are oriented perpendicular to the carbon chain plane, interacting to establish π -bonds. Not confined to a specific bond, electrons within these π -bonds are free to go along the carbon chain.

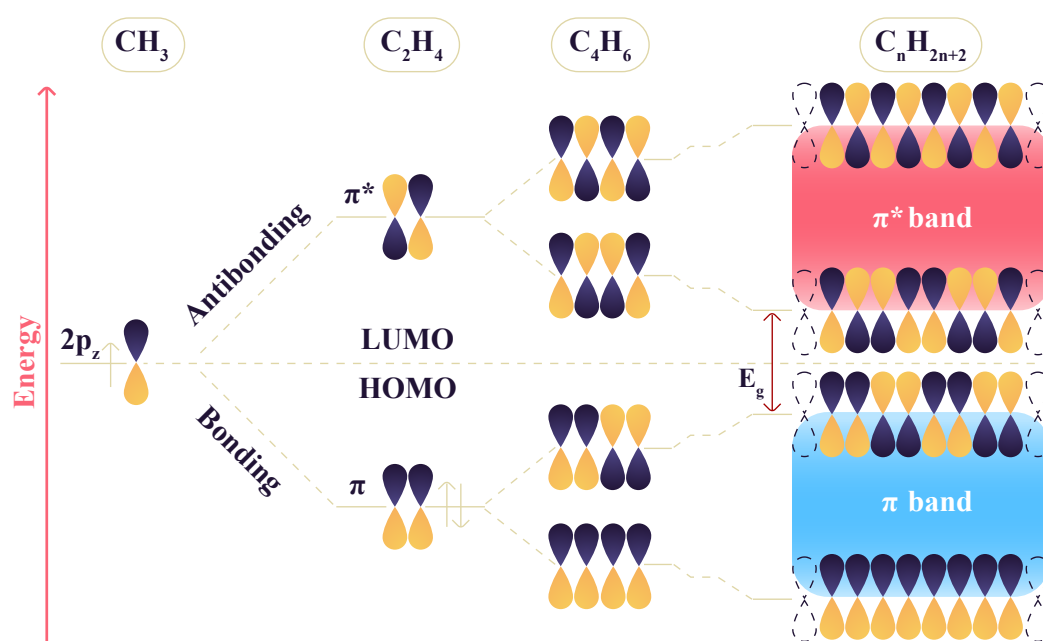


Figure 1.5 Energy diagram of the formation of π orbitals of polyacetylene of different length. Adapted from [23].

When you double the count of carbon atoms in a polyacetylene molecule, there's a splitting of energy levels between the π and π^* orbitals. For C_2H_4 , this results in a single π and one π^* level; C_4H_6 has two π and two π^* levels, while a polyacetylene chain consisting of n carbon atoms will have $\frac{n}{2}\pi$ and $\frac{n}{2}\pi^*$ levels. In polyacetylene structures, all bonding π -orbitals are electron-filled, leaving the antibonding π^* orbitals vacant. Consequently, the

highest energy level of the π levels aligns with the HOMO, and the LUMO corresponds with the lowest energy level of the π^* levels [24].

As the carbon chain lengthens, the distance between the HOMO and LUMO is reduced, leading to a reduction in the band gap. With each carbon atom in the chain contributing to one π electron, a homogeneous distribution of these electrons along the chain would result in uniform distances between the carbon atoms. In the case of infinitely extended chains, this would theoretically eliminate the band gap, yielding a metallic conductivity type. However, Peierls' theorem asserts that a chain with an alternating pattern of single and double bonds maintains greater stability compared to a chain where atoms are equally spaced. This enduring band gap ensures that polyacetylene retains its semiconductor properties. Typically, conducting polymers exhibit band gaps ranging from 1 to 4 eV [25]. For exceptionally long chains, the differences within the π levels, and between the π^* levels, become negligible. This minimal difference allows these levels to be perceived as continuous π and π^* bands. The electron-filled π band and the vacant π^* band are identified as the Valence Band (VB) and Conduction Band (CB), respectively.

1.2.4 Charge Transport

Charge transport mechanisms in OSCs contrast significantly with those in inorganic semiconductors. While inorganic semiconductors facilitate charge transport through delocalized states according to band transport theory, OSCs operate differently. In these materials, molecular units are interconnected via weak Van der Waals forces, leading to transport across localized states. This localization is highly contingent on the π orbital overlap, intimately tying charge transport to the structural attributes of the organic film. Consequently, the transport model varies with the degree of molecular order: band transport theory governs transport in long-range ordered systems, such as organic single crystals, whereas the hopping model is more appropriate for amorphous or polycrystalline systems.

Despite the ongoing progress, a complete comprehension of the transport model for these materials was not yet achieved. In the last decades, several models, with the aim to elucidate charge transport in amorphous or disordered OSCs, were developed and extensively reviewed in literature [26, 27, 28].

Some of the most prevalent models will be detailed in the following sections.

Band Transport Model

In high-quality organic crystals, classical band-like transport is typically observed, attributed to the significant delocalization of charge carriers. These carriers pass through the crystal

in extended Bloch waves, moving seamlessly through the periodic lattice structure. The band transport model suggests an inverse relationship between mobility and temperature; as temperature decreases, mobility is expected to increase. This increase is primarily due to a reduction in charge scattering processes, which are commonly determined by lattice phonons.

The applicability of the band transport model is feasible if the crystal structure presents the two following conditions: a high degree of periodicity and a robust intermolecular interaction. However, these ideal conditions are not always prevalent in organic crystalline materials. Often, such materials are characterized by considerable structural and chemical defects, which coupled with pronounced lattice vibrations, determine a non-ideal scenario required for pure band-like transport.

Hopping Transport Model

Originating from the works of Mott [29] and Conwell [30], and subsequently refined by Miller and Abrahams [31], the hopping transport model provides a framework for understanding charge transport in disordered or amorphous OSCs. Different from ordered systems, where electrons freely pass through the delocalized states, in disordered systems, charges navigate by hopping between localized states. The suitability of this model can be evaluated by analyzing the temperature dependence of electrical mobility. In band-like transport, elevated temperatures increase the charge-phonon scattering, thereby reducing the mobility ($\mu \propto T^{-n}, 0 < n < 3$)

On the contrary, the hopping mechanism is thermally assisted, leading to an increase in mobility while the temperature rises. Specifically, within the hopping model framework, mobility is directly proportional to the transition rate W_{ij} between two distinct states, such as from state i to state j . This relationship is represented by the Miller-Abrahams expression:

$$W_{ij} = \nu_0 e^{-2\gamma|R_{ij}|} \begin{cases} e^{-\frac{\epsilon_j - \epsilon_i}{k_B T}}, & \forall \epsilon_j > \epsilon_i \\ 1, & \text{else} \end{cases} \quad (1.1)$$

where ν_0 represents the phonon vibration frequency, γ represents the wavefunction overlap between states, R_{ij} is the distance between the two states, and ϵ_i, ϵ_j are the energies of the initial and final states, respectively.

Small Polaron Model

Introduced by Holstein in 1959 [32], the Small Polaron theory aims to elucidate the nature of localized states in organic materials. This model suggests that when a charge passes through

the conjugated chain of an organic material, the charge's long-range interaction induces polarization and deformation of the molecular system, resulting in the polaron formation. This polaron effect leads to the self-trapping of the charge.

The Holstein model, a one-dimensional, single-electron framework, calculates the total energy of the system by summing three components. The lattice energy E_L arises from the sum of N harmonic oscillators, each vibrating at frequency ω_0 :

$$E_L = \frac{1}{2} \sum_{n=1}^N \left(M\omega_0^2 u_n^2 + \frac{p_n^2}{M} \right) \quad (1.2)$$

where u_n represents the displacement of the n^{th} molecule from the equilibrium position, and M is the reduced mass of the molecular site.

The model further incorporates the electron energy, computed under the tight-binding approximation, and the electron-lattice coupling. The significance of the polaron binding energy is highlighted, denoting the energy gain of an extremely slow-moving carrier due to lattice polarization. The mobility of the small polaron is then determined by solving the time-dependent Schrödinger equation.

Multiple Trapping and Release Model

The Multiple Trapping and Release model is suitable for describing the charge transport in polycrystalline semiconductors [33]. In such materials, crystalline domains are interspersed with amorphous grain boundaries. Within each microcrystal, charge transport adheres to the band-like model, but charges become trapped at grain boundaries, resulting in a mobility decrease.

Starting from this concept, Horowitz et al. [34] proposed to consider the polycrystalline system as a series of resistors, representing both the grains and their boundaries, connected in series. Mobility in this context is a function of both the grain and boundary mobilities (μ_G and μ_B):

$$\frac{1}{\mu} = \frac{1}{\mu_G} + \frac{1}{\mu_B} \quad (1.3)$$

The mobility varies based on the grain size relative to the Debye Length, distinguishing two distinct regimes for charge transport in polycrystalline semiconductors:

1. For $l > 2L_D$, traps are primarily located at the grain boundaries. The mobility in this scenario is governed by:

$$\mu = \frac{q\bar{v}l}{8k_B T} e^{-\frac{E_B}{k_B T}} \quad (1.4)$$

where q is the electrical charge, \bar{E} is the mean velocity of the charge, and E_B represents the height of the energy barrier at the grain boundaries. In this regime, mobility is directly proportional to the grain dimensions. Interestingly, at lower temperatures, charge transport is dominated by tunneling through energy barriers, making mobility largely temperature-independent.

2. Conversely, for $l < L_D$, the traps at grain boundaries are considered to be uniformly distributed. Mobility in this case is described by:

$$\mu \propto \mu_0 e^{-\frac{E_B}{k_B T}} \quad (1.5)$$

with μ_0 being the intrinsic mobility within the grain. This regime is characterized by thermally activated transport, where mobility increases with increasing temperature. The energy barrier E_B due to trapped charges at grain boundaries is ascertainable by analyzing the temperature dependency of mobility.

1.3 Organic Semiconductor Materials

As mentioned, Organic Semiconductors are typically electroactive, small conjugated molecules or polymers with a strongly π -conjugated system, where electrons are delocalized over the entire structure. OSCs are classified based on polarity as p-type, n-type, and ambipolar. p-type OSCs are electron donor molecules, easily oxidized with a high HOMO energy, usually around -5.0 eV [35]. Conversely, n-type OSCs, being electron acceptors, display a low LUMO energy around -4.0 eV [36]. In ambipolar OSCs, charge transport of both holes and electrons is possible, depending on the applied electric field.

The HOMO and LUMO energies determine the semiconductor's stability in ambient conditions, with n-type OSCs generally showing lower intrinsic stability due to the complexity for molecules synthesis with low LUMO energy. In contrast, p-type OSCs, which have been more extensively studied, exhibit better performances [37, 38]. This work focuses on p-type organic semiconductors.

A distinction can be made between conjugated polymers and small conjugated molecules. In both cases, conductivity is largely determined by the relative position of $\pi - \pi$ orbitals, making molecular ordering crucial for high-performance OFETs.

Polymer OSCs, shown in **Fig. 1.6**, comprising long chains of interconnected electroactive and aromatic groups, cannot be evaporated due to their high molecular weight.

However, they are compatible with solution processing techniques, often forming microcrystalline structures embedded in an amorphous polymer matrix. A notable example

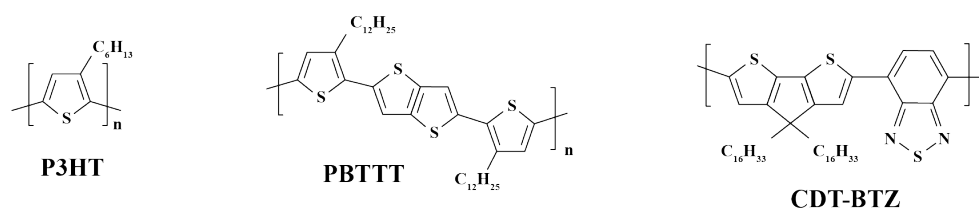


Figure 1.6 Chemical structures of conjugated polymer OSCs.

is poly(3-hexylthiophene) (P3HT), exhibiting mobility of $0.1 \text{ cm}^2/\text{V}\cdot\text{s}$ [39]. Strategies to increase structural order and thus performance include the use of liquid crystal polymers like PBTTT, achieving mobilities up to $0.72 \text{ cm}^2/\text{V}\cdot\text{s}$ [40], and donor-acceptor copolymers like cyclopentadithiophene-benzothiadiazole (CDT-BTZ), with mobilities up to $3.3 \text{ cm}^2/\text{V}\cdot\text{s}$ [41].

Small molecule OSCs, shown in **Fig. 1.7**, on the other hand, can be thermally evaporated or deposited using solution-based techniques. Their higher structural order compared to polymer OSCs results in higher field-effect mobilities, typically around $10 \text{ cm}^2/\text{V}\cdot\text{s}$ [37]. Examples include TIPS-pentacene, TMTES-pentacene, rubrene, diF-TES-ADT, C10-DNTT, DB-TTF, and C8-BTBT.

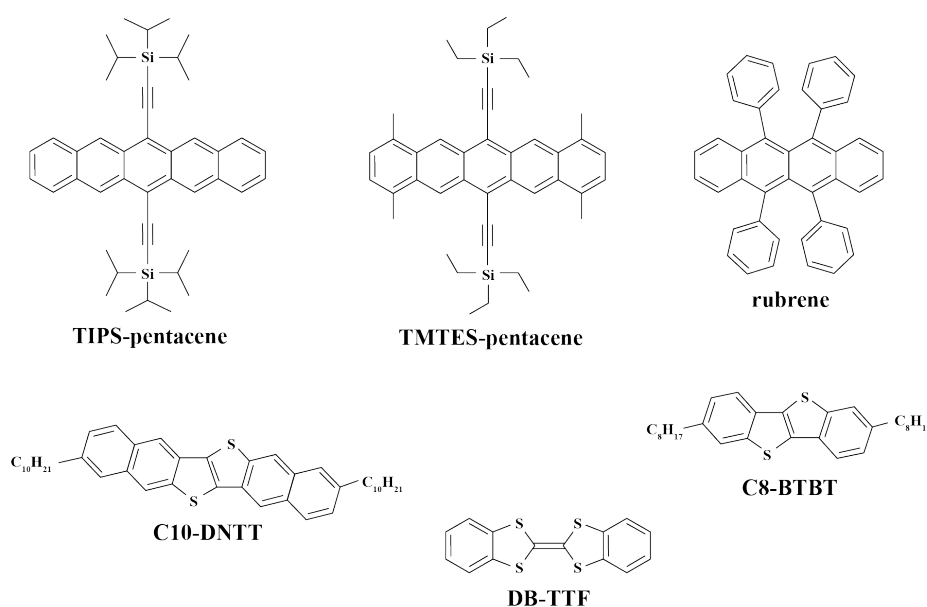


Figure 1.7 Molecular structures of small molecule p-type OSCs.

However, the manufacturing of uniform thin films using solutions is a challenging process due to the low viscosity of these solutions. A promising approach involves blending small semiconducting molecules with an insulating polymer binder to enhance the process method and film uniformity; this new approach will be one of the key aspects of this thesis.

1.3.1 Organic Semiconductor Deposition Techniques

The deposition of OSCs is a crucial step in the fabrication of organic electronic devices. These processing techniques are broadly categorized into vapor-phase deposition and solution-based deposition.

Vapor-Phase Deposition Techniques

Physical Vapor Deposition (PVD) involves the thermic evaporation of the organic material in high vacuum [42]. Typically, the material is placed in an alumina boat inside a vacuum chamber at pressures ranging from 10^{-6} to 10^{-8} mbar. A schematic representation of an evaporation chamber is illustrated in **Fig. 1.8**.

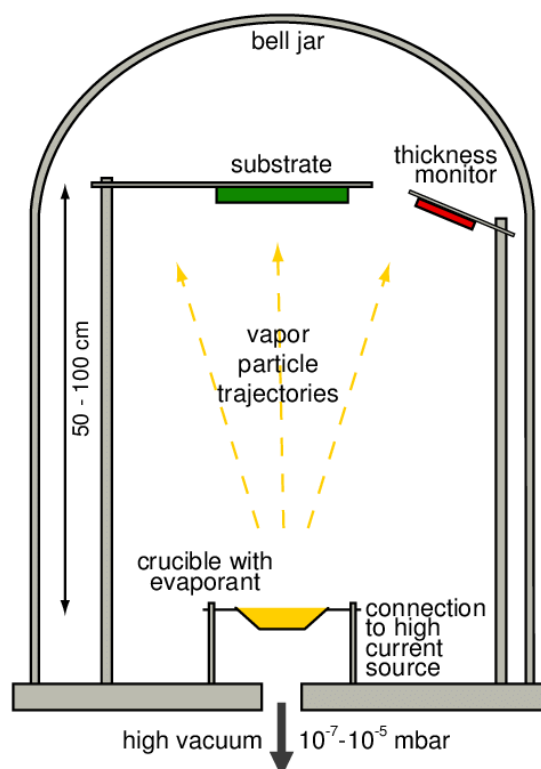


Figure 1.8 Schematic representation of a thermal evaporation system [42].

The process yields high-quality films with precise control of film thickness. Substrate temperature control can impact film morphology and crystallinity. This method also allows

for multilayer deposition and co-deposition; generally, it is not suitable for large-area and low-cost fabrication due to the cost of the equipment.

Solution-Based Deposition Techniques

These techniques are preferred for organic semiconductor thin film deposition due to low cost and suitability for large-area deposition [43]:

- **Drop Casting:** a drop of OSCs solution is put on the substrate, letting the solvent evaporate; often the evaporation is followed by thermal annealing to improve crystallinity. Drop-casting is a simple technique, but control and reproducibility are lacking, and the process is not scalable.
- **Spin Coating:** it is widely used for laboratory-scale deposition. The OSCs solution is dropped on the substrate and spun at high speed to uniformly spread and dry the film. Film thickness depends on the solution concentration, viscosity, and spinner parameters. However, this technique is not suitable for large-area applications.
- **Dip Coating:** it involves the immersion of the substrate in an OSCs solution and then the substrate is withdrawn vertically at a controlled speed. The technique is suitable for covering large areas and can be upscaled, but it requires large volumes of solution.
- **Spray Coating:** it uses high-pressure gas (usually N₂) to vaporize the OSCs solution and deposit it on the substrate. It can cover large areas and it is versatile for different substrates, but films tend to have higher roughness compared to other techniques.
- **Zone Casting:** it involves continuous deposition from a flat nozzle on a moving substrate. It's suitable for large-scale manufacturing but films result highly anisotropic and the deposition speed is slow.
- **Blade Coating:** an OSCs solution is spread on the substrate using a blade; the film thickness is dependent on the blade-substrate distance. This technique is adaptable to roll-to-roll processes and can achieve high coating speeds.
- **Bar-Assisted Meniscus Shearing (BAMS):** it is a variant of blade coating, forming a liquid meniscus between the substrate and a rounded bar. The solution is dispensed into the gap, forming a uniform film as the meniscus is dragged horizontally (**Fig. 1.9**). In BAMS, the film thickness depends on the solution viscosity, surface tension, substrate surface energy, and bar/substrate speed [44]. The substrate temperature also influences film formation, and crystallization is controlled by OSCs concentration, and solvent evaporation rate. This technique was widely employed in this work for depositing organic semiconducting thin films.

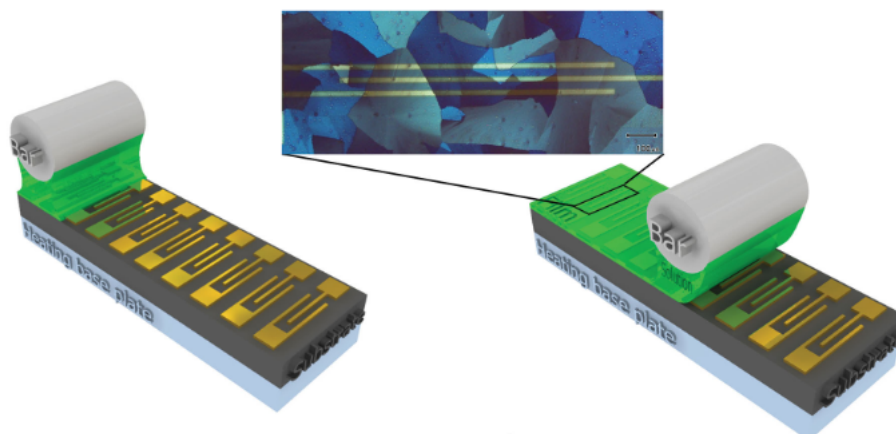


Figure 1.9 Schematic representation of the BAMS technique [44].

1.4 Doping of Organic Semiconductor

Doping techniques transformed the semiconductors, enabling precise manipulation of their transport properties and facilitating the creation of p-n junctions. This innovation not only enhanced existing semiconductor technologies but also encouraged the invention of novel devices, such as the bipolar transistor [45]. The advent of organic semiconductors saw the extension of doping techniques, originally developed for the inorganic ones. Early experiments in doping organic materials utilized highly reactive gases, and subsequently, minute atoms or molecules, to reach high levels of conductivity. However, the stability of devices was compromised due to the propensity of these diminutive dopants to migrate within the organic layers [46]. Nowadays, a pivotal advancement was observed with the introduction of molecular dopants: these larger dopants provided a similar function without the significant risk of diffusion associated with atomic-sized dopants [47, 48].

1.4.1 Mechanisms of Doping

The doping of inorganic semiconductors, like silicon, is achieved by incorporating impurity atoms into the crystalline structure of the semiconductor host material. In silicon, which has four valence electrons, the incorporation of pentavalent impurities (e.g., phosphorous) introduces one extra electron per each impurity atom added, increasing the density of mobile negative charge carriers and rendering the semiconductor n-type. Similarly, trivalent impurities (e.g., boron) introduce holes, leading to an increase in positive charge carriers, resulting in a p-type semiconductor.

According to classical semiconductor theory [49], the densities of negative (n_0) and positive charge carriers (p_0) in an intrinsic semiconductor can be calculated using Fermi-Dirac statistics, depending on the positions of the Conduction Band (CB) (E_C) and Valence Band (VB) (E_V). For intrinsic semiconductors ($n_0 \approx p_0$), the Fermi level (E_F) is located near the gap's center ($E_g = E_C - E_V$) and is given by:

$$E_F = \frac{E_g}{2} + \frac{k_B T}{2} \ln \left(\frac{N_V}{N_C} \right) \quad (1.6)$$

where N_C and N_V are the effective densities of states in the CB and VB, respectively.

In n-type semiconductors, impurity atoms create shallow donor states (E_D) below the CB edge, shifting the Fermi level towards the CB. Similarly, in p-type semiconductors, shallow acceptor states (E_A) are introduced above the VB edge, shifting the Fermi level towards the VB. These states are positioned close to the respective band edges:

$$\begin{cases} |E_C - E_D| < k_B T \ln \left(\frac{N_D}{N_C} \right) \\ |E_V - E_A| < k_B T \ln \left(\frac{N_A}{N_V} \right) \end{cases} \quad (1.7)$$

where N_D and N_A are the effective densities of states in the donor states and acceptor states, respectively. The Fermi level for n-type and p-type semiconductors (**Fig. 1.10**) is thus given by:

$$\begin{cases} E_F = E_C - k_B T \ln \left(\frac{N_C}{N_D} \right) \\ E_F = E_V + k_B T \ln \left(\frac{N_V}{N_A} \right) \end{cases} \quad (1.8)$$

respectively. This indicates that, by controlling the dopant concentrations (N_D and N_A), the number of charge carriers and hence the conductivity can be accurately controlled.

The doping of organic semiconductors follows different processes. Small atoms, like halides or alkali metals, when used as dopants in organic layers lead to device instabilities due to their diffusion tendency. This issue was resolved using small donor or acceptor molecules as molecular dopants, which, due to their size, have a smaller tendency to diffuse [46]. Utilizing small molecules as dopants, the conductivity of organic semiconductors can be increased significantly which can enable the development of high-performance devices.

Similar to inorganic semiconductors, the doping of organic semiconductors leads to a shift of the Fermi level towards the respective transport level (p-type to the HOMO, n-type to the LUMO) when increasing dopant concentration. However, differently from inorganic semiconductors, the increase in conductivity and the shift in Fermi level saturate at dopant concentrations of a few mole percent.

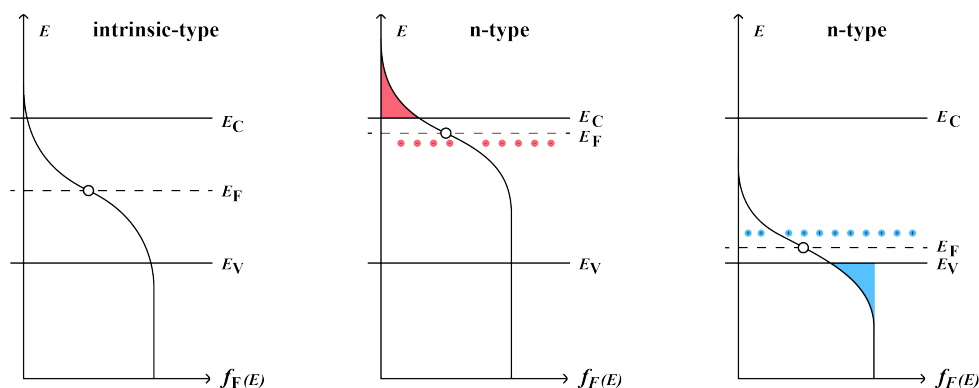


Figure 1.10 Fermi level shift: n-type doping induces an upward shift of E_F towards the CB due to shallow donor states; p-type doping leads to a downward shift of E_F towards the VB with shallow acceptor states.

For molecular doping of organic semiconductors, two distinct mechanisms are known: Ion Pair (IPA) formation and ground state Charge Transfer complex (CPX) formation (**Fig. 1.11**) [50]. Both mechanisms can be spectroscopically evidenced by observing diagnostic absorption features of the molecular ions.

In the case of IPA formation, an electron is transferred from the HOMO of the host to the LUMO of the dopant, resulting in the formation of an ion pair (host cation and dopant anion). This requires that the dopant's Electron Affinity (EA) be greater than the host's Ionization Energies (IEs) ($EA_{\text{dopant}} > IE_{\text{host}}$) for efficient charge transfer.

In the case of CPX formation, the frontier orbitals of the dopant and host hybridize in a supramolecular complex, forming new HOMO/LUMO states. The energy of the frontier levels of the formed complex ($E_{\text{CPX}}^{\text{H/L}}$) can be derived via [51]:

$$E_{\text{CPX}}^{\text{H/L}} = \frac{E_{\text{host}}^{\text{HOMO}} + E_{\text{dop}}^{\text{LUMO}}}{2} \pm \frac{1}{2} \sqrt{(E_{\text{host}}^{\text{HOMO}} - E_{\text{dop}}^{\text{LUMO}})^2 + 4\beta^2} \quad (1.9)$$

where $E_{\text{host}}^{\text{HOMO}}$ is the energy of the host's HOMO, $E_{\text{dop}}^{\text{LUMO}}$ is the energy level of the dopant's LUMO, and β is the resonance integral describing the interaction. CPX formation does not require the condition $EA_{\text{dopant}} > IE_{\text{host}}$ to be fulfilled and can occur even when IPA formation is not possible.

Recent studies have demonstrated that both IPA and CPX formation can occur within the same material pair under special processing conditions, expanding our understanding of doping mechanisms in organic semiconductors [52].

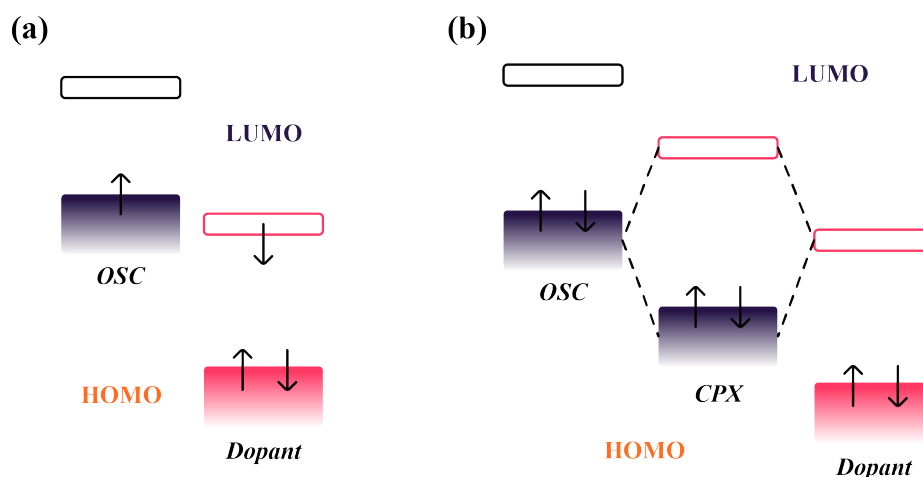


Figure 1.11 (a) Ion Pair (IPA) formation involves electron transfer from the host HOMO to the dopant LUMO, creating a mobile hole charge carrier in the host matrix. (b) Charge Transfer complex (CPX) formation results from the overlap of host and dopant frontier orbitals. Adapted from [52].

p-Type Doping

In the early stages of doping organic semiconductors, oxidizing gases such as iodine (I_2), bromine (Br_2), chlorine (Cl_2), or even oxygen were used to p-dope organic semiconductors [53]. However, these atomic dopants were prone to diffusion, leading to device instabilities. The emergence of molecular p-dopants, particularly those with quinone structures and unsaturated aromatic rings, marked a significant advancement. A prototypical example is Tetracyanoquinodimethane (TCNQ) [54], known for forming charge-transfer salts with small donor molecules. Despite the low EA of 4.2 eV, limiting the ability to dope organic semiconductors with IEs in the 5-6 eV range, it paved the way for the development of molecular dopants with higher EAs. These dopants typically have an electron-poor core and are decorated with electron-withdrawing groups to increase the EA.

2,3,5,6-tetrafluoro-7,7,8,8-tetracyanoquinodimethane (F4TCNQ) (**Fig. 1.12**), a fully fluorinated version of TCNQ with an EA of 5.2 eV [54], emerged as an effective molecular p-dopant, capable of successfully doping a wide range of organic semiconductors.

However, it sublimates around 80 °C in Ultra-High Vacuum (UHV) and could contaminate the vacuum chambers, leading to unintentional doping of other samples. To address these issues, larger molecular dopants such as quinodimethane-based TCNQ and F6TCNNQ, or

fluorinated fullerenes like C₆₀F₃₆, with EAs of 4.7 eV, 5.6 eV, and 5.4 eV respectively, have been developed. These larger molecules exhibit higher sublimation temperatures and the diffusion effect is reduced due to their larger size [51].

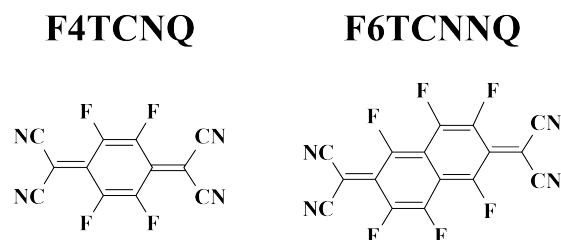


Figure 1.12 Chemical structures of typical p-type dopants.

n-Type Doping

While various stable molecular p-dopants have been developed and used in devices over the past decade, molecular n-doping poses more manufacturing challenges [52].

Historically, n-doping was dominated by alkali metals like sodium (Na), potassium (K), lithium (Li), or cesium (Cs), but these led to the device's instability [52, 51]. The first molecular n-dopant, BEDT-TTF, despite not being so efficient, lets to understand that the use of molecular dopants for n-doping is feasible. Subsequently, further developments have taken place employing one-electron reductants, like Tetrathianaphthacene (TTN), organometallic compounds, like [Ru(terpy)₂]⁰, W₂(hpp)₄, or Cr₂(hpp)₄, and organometallic sandwich compounds, like cobaltocene or decamethylcobaltocene [55]. Some of these dopants were highly efficient, but their low ionization energy made them unstable in air and complex to handle and use. Additionally, compounds like cobaltocene had high vapor pressures and could be deposited only in vacuum conditions.

A general strategy to overcome these issues is to use air-stable precursors that could be released as strong reducing agents during or after insertion into the organic host or could react through electron transfer followed by bond cleavage and/or formation. This approach has been exemplified by cationic dyes and benzoimidazole derivatives like o-MeO-DMBI-I. These compounds sublime from the precursor material when heated in UHV, and have been used to effectively dope materials with EAs ≥ 4.0 eV [56].

Another approach involves materials like hydride-reduction products of stable organic cations, tetraalkylammonium salts of inorganic ions, or dimers formed by certain 19-electron organometallic sandwich compounds. These molecules have been shown to effectively n-

dope fullerene derivatives and polymers like P(NDIOD-T2), but their efficacy can be variable depending on the host material's EA [57].

Organometallic dimers, which can dissociate into highly reducing monomers during or after deposition, have been used to dope various organic materials, including those with EAs ranging from 3.9 eV down to 2.8 eV [58]. These dimers consist of metallocene monomers with a group 9 or 8 metal sandwiched between cyclopentadiene or an arene group. The doping process of these dimers involves reversible endergonic cleavage followed by the rapid exergonic electron transfer or a reversible endergonic electron transfer followed by irreversible dissociation and a second electron-transfer reaction [59].

Recent studies have demonstrated that photo-activation of these dimers can result in efficient n-doping of low EA host semiconductors, expanding the range of materials that can be effectively doped. This approach, combining cleavable dimers with photo-activation, represents a promising opportunity for efficient n-doping of materials with very low EAs, a domain previously limited to alkali metals [59].

1.5 Organic Field-Effect Transistors (OFETs)

An Organic Field-Effect Transistors (OFETs) is a three-terminal (source, gate, and drain) device designed to modulate the density of charge carriers within the organic semiconductor layer [37]. This modulation alters the current flowing between the source and drain electrodes, controlled by the voltage applied at the gate electrode. In this structure, the gate electrode is separated from the OSCs by a dielectric layer, forming a metal/insulator/semiconductor configuration. This arrangement allows, when an electric field is generated at the gate, to induce an accumulation of charge carriers at the OSCs/dielectric interface, thereby creating a conductive channel. It's critical to note that in OFETs, conduction is primarily confined to the initial few monolayers of the organic semiconductor, which facilitates charge transport. This selective conductivity is a key feature of OFETs, influencing their operational efficiency and potential application.

OFETs are versatile in their assembly, capable of being structured into four distinct geometries, as illustrated in **Fig. 1.13** [60].

These configurations are categorized based on the placement of the source/drain contacts and the gate electrode relative to the organic semiconductor layer. They include **Fig. 1.13a** Bottom-Gate Bottom-Contact (BGBC), **Fig. 1.13b** Bottom-Gate Top-Contact (BGTC), **Fig. 1.13c** Top-Gate Bottom-Contact (TGBC), **Fig. 1.13d** Top-Gate Top-Contact (TGTC) geometries. The choice of OFETs architecture significantly influences device perfor-

mance: an understanding of the pros and cons of each architecture is critical for the choice of fabrication method.

In BGTC and TGTC designs, there's typically higher contact resistance, attributed to the reduced contact area between the organic semiconductor channel and the source electrode [61]. On the other hand, in top-contact configurations, the metal electrodes are often evaporated through a shadow mask as the final manufacturing step. This process can decrease the contact resistance due to enhanced metal/OSCs interface contact, promoting better charge injection. For example, BGTC architecture involves depositing the OSCs on the dielectric layer first, followed by the source/drain electrodes [62]. This determines a more uniform and smoother OSCs layer, useful for two-dimensional conduction at the OSCs/dielectric interface. However, this configuration could determine potential damage to the sensitive OSCs layer during top contact evaporation phase.

Furthermore, top-gate designs offer an added advantage by encapsulating the device, thereby enhancing the stability of the organic semiconductor in the presence of atmospheric agents. The specific geometry OFETs also determines the processing sequence and the deposition steps.

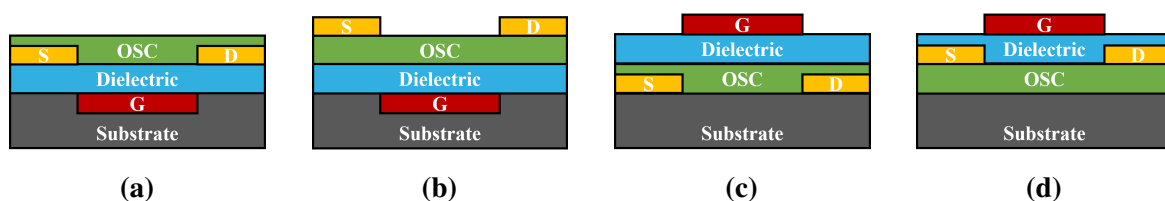


Figure 1.13 Schematic geometries for Organic Field-Effect Transistors: (a) Bottom-Gate Bottom-Contact, (b) Bottom-Gate Top-Contact, (c) Top-Gate Bottom-Contact, (d) Top-Gate Top-Contact.

For instance, the BGBC architecture is often preferred for straightforward and rapid processing, as the semiconductor thin film deposition is the final step. This approach is particularly beneficial when testing new OSCs materials or optimizing the deposition of organic layers. Additionally, the bottom electrodes, in BGBC and TGBC, can be modified using Self-Assembled Monolayers (SAMs) to face the charge injection challenges [63]. SAMs are molecular assemblies that spontaneously form on surfaces through the adsorption of an active compound from a solution or vapor phase. The quality of charge injection and transport is crucial for device performance. Charge injection, the process of introducing charge carriers (electrons or holes) into the semiconductor layer from the electrodes, can be significantly influenced by the interface properties of the electrodes. Here, SAMs play a critical role:

- **Reduction of contact resistance:** SAMs can be engineered to modify the work function of the electrode material, making it more compatible with the semiconductor's

energy levels. This alignment can reduce the energy barrier for charge carriers, leading to lower contact resistance and more efficient charge injection.

- **Improved interface quality:** SAMs can form highly ordered and stable interfaces, which can improve the consistency and reliability of the charge injection process. This improved interface quality can enhance the overall performance and stability of the device.
- **Control over interfacial chemistry:** by choosing specific molecules for the SAMs, it's possible to tailor the chemical and physical properties of the electrode surface. This customization can be used to optimize the interaction between the electrode and the semiconductor, further improving charge injection and transport.
- **Versatility and scalability:** the process of forming SAMs is relatively simple and can be integrated into existing fabrication protocols. The integration characteristics, combined with the ability to fine-tune the monolayer's properties, make SAMs a versatile tool in device engineering.

In summary, the modification of bottom electrodes using SAMs is a sophisticated strategy to enhance charge injection. Indeed, the potential impact of crystallization sensitivity of the organic material to the underlying surfaces (like electrodes or dielectrics) has to be considered, since this can lead to variable OSCs morphologies across the device [64].

1.5.1 Operation Principle

The operation principle of OFETs is based on the conductivity modulation of the organic semiconductors via gate voltage application. This concept is elucidated through a simplified electronic energy level diagram (see **Fig. 1.14a**), depicting the HOMO and LUMO of an organic semiconductor relative to the source/drain electrodes Fermi levels, which are dependent on the metals work-function [60].

In the absence of a source-gate voltage (V_{SG}), an ideal OFETs would exhibit no mobile charges and thus no charge transport when a source-drain voltage (V_{SD}) is applied. For a p-type semiconductor, applying a negative V_{SG} a hole accumulation at the OSCs/dielectric interface happens (**Fig. 1.14b**). This negative V_{SG} causes an upward shift in HOMO and LUMO energies, bringing the HOMO closer to the source electrode's Fermi Energy (E_F). With a sufficiently strong gate electric field, the HOMO aligns with the E_F , enabling hole injection and current flow (I_{SD}) from source to drain with a negative V_{SD} (**Fig. 1.14c**). Conversely, n-type semiconductors exhibit the reverse behavior, with electrons as the primary charge carriers and LUMO-related conduction. Here, positive V_{SG} and V_{SD} are required to achieve charge accumulation and current flow (**Figs. 1.14d and 1.14e**).

It's evident that the alignment between the metal electrodes' E_F with the OSCs HOMO or LUMO is crucial to obtain an efficient charge injection and a highly performing device. However, this is a simplified description of the OFETs operation and charge transport mechanisms. Factors like charge trapping, due to chemical or structural defects in the OSCs or at the OSCs/dielectric interface, significantly impact OFETs performance. Additionally, contact resistance, arising from mismatches between metal and semiconductor energy levels, can also affect device functionality.

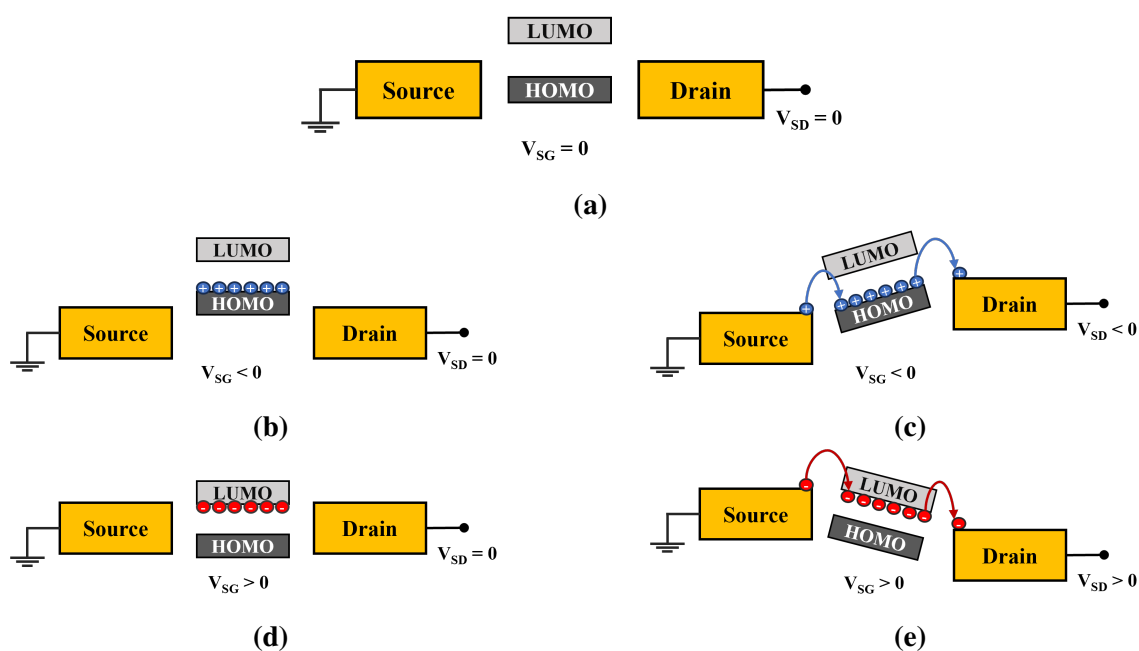


Figure 1.14 Schematic illustration of the working principle of OFETs: (a) Ideal device in the off-state with no applied V_{SD} and V_{SG} . (b) Shift of the HOMO/LUMO levels due to negative V_{SG} and the resultant hole accumulation near the OSCs/insulator interface. (c) Hole transport induced by applying a negative V_{SD} . (d) Shift in HOMO/LUMO levels caused by a positive V_{SG} , leading to electron accumulation near the OSCs/insulator interface. (e) Electron transport occurring due to a positive V_{SD} .

To provide a mathematical representation of OFETs current-voltage characteristics, Horowitz et al. proposed a model based on the traditional Metal-Oxide-Semiconductor Field-Effect Transistors (MOSFETs) theory [65]. This model assumes constant charge carrier mobility (μ) within the operational range, neglects parasitic contact resistance, and applies the gradual channel approximation, where the gate electrode's perpendicular electric field is stronger than the parallel field from the source and drain electrodes.

This model delineates two operational regimes for the OFETs. In the linear regime, where $|V_{SD}| \ll |V_{SG} - V_{th}|$, the source-drain current (I_{SD}) linearly increases with V_{SD} , described by the equation:

$$I_{SD,lin} = \mu_{lin} \cdot \frac{W}{L} \cdot C \cdot \left[(V_{SG} - V_{th}) \cdot V_{SD} - \frac{V_{SD}^2}{2} \right] \quad (1.10)$$

Conversely, in the saturation regime, where $|V_{SD}| \gg |V_{SG} - V_{th}|$, I_{SD} reaches a plateau, becoming independent of V_{SD} , as described by:

$$I_{SD,sat} = \mu_{sat} \cdot \frac{W \cdot C}{2 \cdot L} \cdot (V_{SG} - V_{th})^2 \quad (1.11)$$

OFETs are characterized through two primary measurements. Output characteristics are determined by sweeping the source-drain voltage at constant gate voltages, as shown in **Fig. 1.15b**. Transfer characteristics, on the other hand, are derived by measuring I_{SD} as a function of V_{SG} at constant V_{SD} , often plotted in a semilogarithmic scale due to the wide range of OFETs current variations (**Fig. 1.15a**).

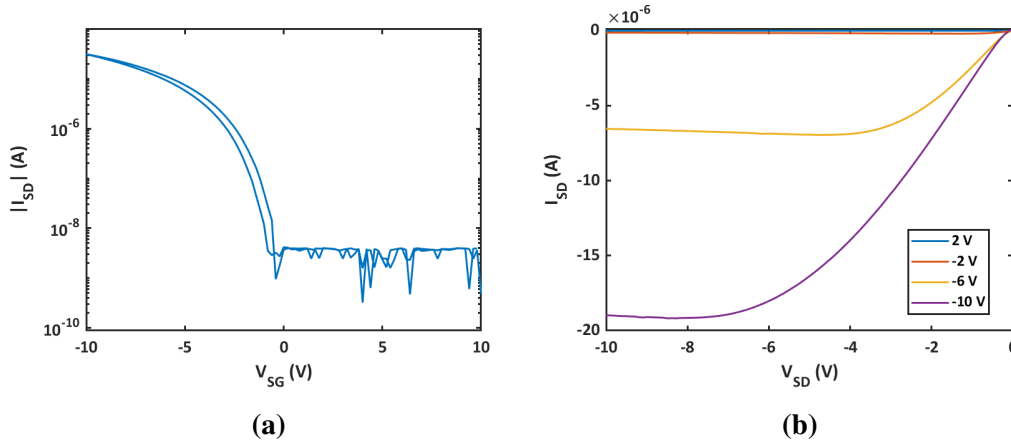


Figure 1.15 Typical current-voltage characteristics of p-type OFETs: **(a)** Transfer characteristics, **(b)** Output characteristics.

OFET Parameters

The electrical performance of Organic Field-Effect Transistors is characterized by several key parameters, essential for assessing and comparing device quality and performance [37]. The most crucial OFETs parameters and their extraction methods are outlined below.

Field-Effect Mobility

The mobility (μ) of a material quantifies how readily charge carriers move within the material under an electric field. At low electric fields E , the average drift velocity v of charge carriers is directly proportional to E , leading to the mobility equation:

$$\mu = \frac{|v|}{|E|} \quad (1.12)$$

This relation yields mobility in units of $\text{cm}^2/\text{V}\cdot\text{s}$. However, it's important to note that this linear relationship breaks down at high electric fields.

In OFETs, the critical parameter is the field-effect mobility (μ_{FE}). Ideally, μ_{FE} extracted from OFETs characteristics should align with the intrinsic material mobility. Actual devices often display lower mobility due to defects, contact resistance, and traps, making μ_{FE} more a device parameter than a material property. Different μ_{FE} values can be derived for devices based on the same OSCs but processed differently or using varied device configurations.

In the linear regime, μ_{FE} is determined using:

$$\mu_{FE,lin} = \frac{L}{W \cdot C \cdot |V_{SD}|} \cdot \left(\frac{\partial I_{SD,lin}}{\partial V_{SG}} \right)_{V_{SD}=const} \quad (1.13)$$

Plotting $I_{SD,lin}$ versus V_{SG} , the slope of the curve through a linear fit, and then inserting this slope in the equation provides a mean device mobility in the linear regime. Alternatively, calculating the derivative of $I_{SD,lin}$ versus V_{SG} gives $\mu_{FE,lin}$ versus V_{SG} , which provides some additional information of the gate voltage dependence of the mobility. In an ideal case, the mobility should be independent of the gate voltage.

In the saturation regime, μ_{FE} is extracted using:

$$\mu_{FE,sat} = \frac{2 \cdot L}{W \cdot C} \cdot \left(\frac{\partial \sqrt{|I_{SD,sat}|}}{\partial V_{SG}} \right)_{V_{SD}=const}^2 \quad (1.14)$$

The plotting $\sqrt{|I_{SD,sat}|}$ versus V_{SG} allows the calculation of the slope through a linear fit and then allows the determination of the mean device mobility in the saturation regime, as depicted in **Fig. 1.16**.

Threshold Voltage and Switch-on Voltage

For MOSFETs, the threshold voltage (V_{th}) is a key parameter, defined as the onset of strong inversion. In OFETs, operating mostly in the accumulation regime, V_{th} is interpreted as the gate voltage at which current begins to flow. Extracting V_{th} in the saturation regime involves plotting $\sqrt{|I_{SD,sat}|}$ versus V_{SG} , with the intercept on the V_{SG} axis indicating V_{th} (**Fig. 1.16**). However, real devices often deviate from this linearity, making the method empirical.

The switch-on voltage (V_{on}) indicates when the transistor activates, or when the accumulation channel is formed. It's extracted from the point in a semilogarithmic plot of $|I_{SD,sat}|$

versus V_{SG} where the current starts increasing with gate voltage. Ideally, V_{on} and V_{th} should be identical and equal to zero.

On/Off Current Ratio

The on current (I_{on}) and off current (I_{off}) are critical for assessing OFETs. I_{on} is the maximum current in the on state and should be high, while I_{off} should be minimal, reflecting the active material's quality. The on/off ratio provides insights into the switching efficiency and current amplification capability of OFETs. Comparisons should be made under the same V_{SG} and V_{SD} conditions, as illustrated in **Fig. 1.16**.

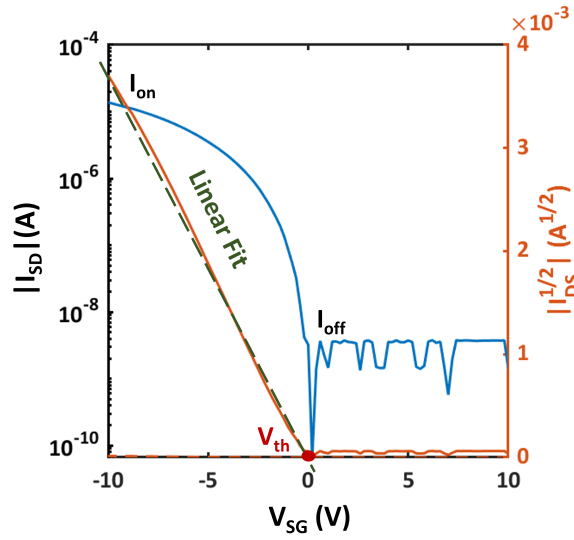


Figure 1.16 OFETs parameters extraction shown in a typical transfer characteristic.

Subthreshold Swing

In the subthreshold region of the transfer characteristics, where the gate voltage V_{SG} is below the threshold voltage V_{th} , the Subthreshold Swing (SS) becomes a significant parameter. It quantifies the sharpness of OFETs turn-on characteristic, defined as the voltage required to increase the source-drain current by an order of magnitude:

$$SS = \left(\frac{\partial \log |I_{SD}|}{\partial V_{SG}} \right)^{-1} \quad (1.15)$$

Typically, SS is expressed in V/dec. A smaller SS value indicates efficient device turn-on at a lower voltage, reducing power consumption. It also suggests a low density of charge carrier traps and high OSCs/dielectric interface quality, as indicated by:

$$N_T \approx \frac{C}{q^2} \left[\frac{q \cdot SS}{k_B \cdot T \cdot \ln(10)} - 1 \right] \quad (1.16)$$

Here, q is the electron charge, k_B is the Boltzmann constant, and T is the temperature.

Detrimental Effects on Device Performance

To optimize device performance, it has to be carefully considered the OSCs crystallization, dielectric and electrode materials, and their interfaces. However, defects in these aspects could lead to issues such as charge trapping and injection problems, negatively impacting OFETs characteristics.

Trapping of Charge Carriers and Hysteresis Effects

Hysteresis in OFETs characteristics, seen as looping in the I_{SD} during forward and reverse V_{SG} sweeps, is often caused by charge trapping. Structural defects and chemical impurities in even the purest organic single crystals, along with the instability of organic materials under ambient conditions (where moisture and oxygen act as dopants), contribute to this hysteresis effect. Consequently, parameter extraction in the presence of hysteresis phenomenon should be approached with caution.

Contact Resistance

Contact Resistance (R_C) at the electrodes/OSCs interface can significantly limit the charge injection. The width-normalized contact resistance ($R_C \cdot W$) in OFETs with solution-processed semiconductors is considerably higher than that of Si MOSFETs. Efficient charge injection requires alignment of the HOMO/LUMO energies of the semiconductor with the metal electrodes work-function. The total resistance of a transistor (R) includes both the channel resistance (R_{ch}) and the contact resistance (R_C):

$$R = R_{ch} + R_C \quad (1.17)$$

In staggered devices, the thickness of the semiconductor layer is crucial, influencing both injecting and extracting electrodes' contact resistances ($R_{C,source}$ and $R_{C,drain}$), as well as the internal resistance at the electrodes/OSCs interface (R_{int}) and the transport through an OSCs bulk region with low conductivity (R_{bulk}).

1.5.2 OFETs in Sensing Applications

As previously mentioned, the processing characteristics of organic semiconductors, including low-temperature requirements and compatibility with solution-based techniques, make them ideal for electronic applications that require low-cost, lightweight, large-area coverage, and structural flexibility. Organic Field-Effect Transistors, in particular, are being extensively researched for their potential in new chemical and physical sensing devices [66].

Chemical and Bio-chemical Sensing

OFETs ability to detect analytes at low concentrations with stability, reproducibility, and selectivity is highly valuable for applications in food processing, environmental analysis, and medical diagnostics [67, 68]. Organic semiconductors can interact with various analytes on the OSCs surface, within polycrystalline film crystallites, and at the OSCs/dielectric or OSCs/electrode interfaces. These interactions can then be transduced into measurable electronic information through the OFETs current-voltage characteristics.

Most OFETs-based chemical sensors measure device response in the presence of specific gases or chemical vapors [68]. Advances in bio-recognition capabilities are also underway, involving functionalization with DNA strands, antibodies, or enzymes. Yu et al. fabricated a DNA-based chemical sensor for detecting nitrogen dioxide (NO_2), integrated into an OFETs (Fig. 1.17) [69].

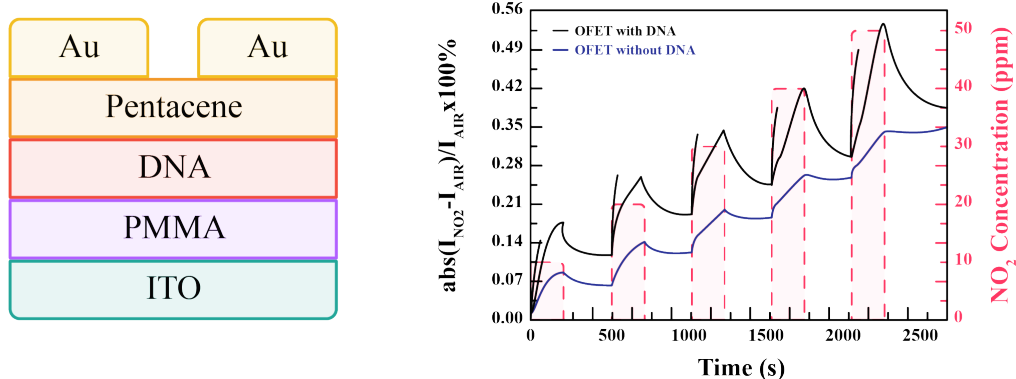


Figure 1.17 Schematic representation of DNA-based chemical sensor with sensing performance in the presence of various NO_2 concentrations. Adapted from [69].

In this sensor design, DNA is applied between the gate dielectric and the organic semiconductor layer using spray-coating, serving as the detection layer for NO_2 . Compared to

the OFETs without the DNA layer, the OFETs with the DNA interlayer demonstrated significantly improved sensing performance in the presence of various NO_2 concentrations. The sensitivity of the DNA-interlayered OFETs sensor was approximately an order of magnitude higher than that of the control device as shown in **Fig. 1.17**.

This enhanced performance is evident by observing the notable shifts in saturation current and the charge carrier mobility that occur after NO_2 exposure. This enhancement is attributed to the negatively charged phosphate groups in the DNA molecules, which interact with the NO_2 analytes, thereby improving the sensing performance of the DNA-incorporated OFETs. Moreover, OFETs-based liquid sensors have been used for the detection of various biomaterials, health-related molecules, and chiral molecules [70, 71]. To this end, different device configurations have been developed, including OFETs and Electrolyte-Gated Organic Field-Effect Transistors (EG-OFET) (**Fig. 1.18**).

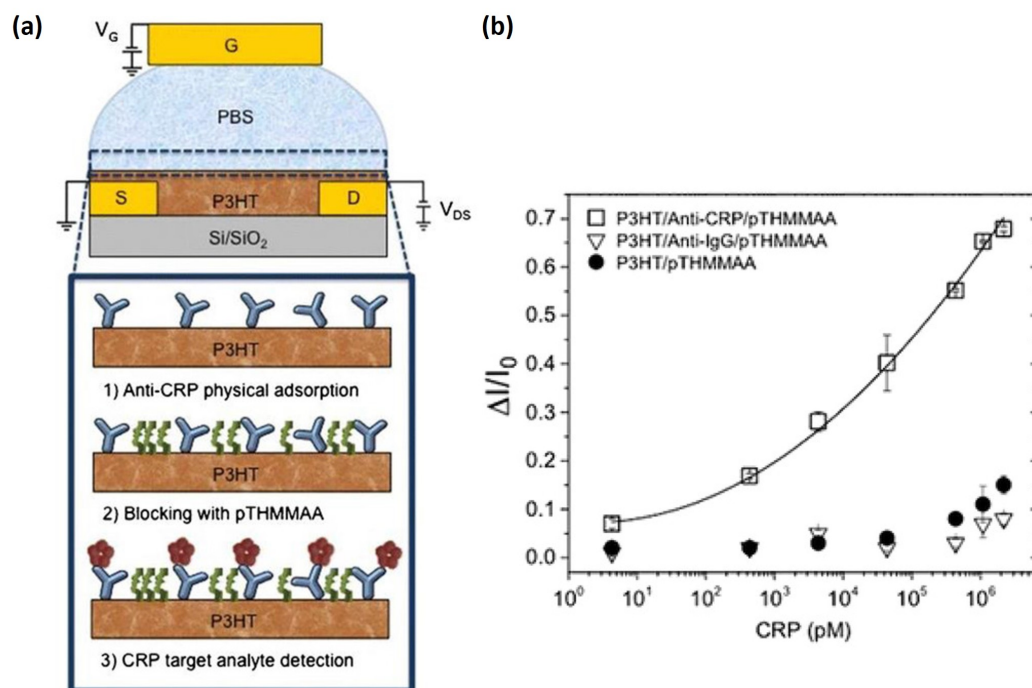


Figure 1.18 (a) Device structure of developed EG-OFET immunosensor for C-Reaction Protein detection. (b) CRP calibration curve obtained for EG-OFET immunosensor (square symbols) [72].

EG-OFET are emerging as innovative platforms for detecting high molecular weight biomolecules. This technology enables stable and reliable label-free sensing of specific analytes through the appropriate functionalization of Organic Semiconductors layers or receptor layers. Magliulo et al. successfully attached the anti-C-Reaction Protein (anti-CRP) to a poly-3-hexyl thiophene (P3HT) OSCs surface via physical adsorption, achieving ultra-sensitive label-free detection of CRP in clinically relevant serum samples [72]. Additionally,

to prevent non-specific absorption of the analyte CRP, a non-ionic hydrophilic polymer (pTHMMAA) was employed to cover the surface of P3HT not covered with the anti-CRP monoclonal antibody. They reported a detection limit as low as 2 pM, as shown in **Fig. 1.18**. Additionally, the reproducibility across devices was verified, with measurements from three different immunosensors on separate chips showing variability within the range of 1% to 14%.

Physical Sensing

OFETs are widely employed for the development of new sensors for physical phenomena, with applications in mechanical force detection and electromagnetic energy detection [73, 74].

Mechanical-sensing devices, particularly pressure sensors, are being explored for innovative applications like electronic artificial skin and wearable healthcare devices [75, 76, 77]. These sensors operate by inducing changes in the active layer structure or dielectric capacitance under applied pressure, leading to variations in current. Their sensitivity depends on factors like the semiconductor and microstructure of the layer. In 2005, Darlinski et al. explored a novel application where the OFETs itself served as the sensor element [78]. To apply mechanical force on the OFETs, they used a motor-controlled microneedle, as depicted in **Fig. 1.19**. The pressures exerted on the OFETs were quantified while the devices were positioned on a balance.

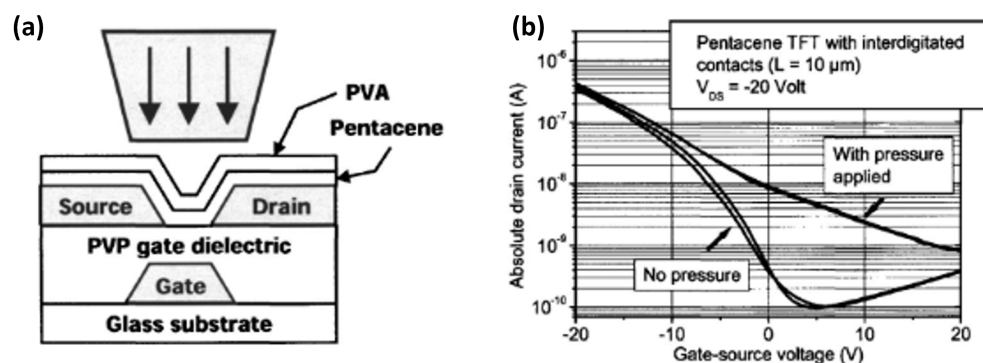


Figure 1.19 (a) Schematic cross-section of the experiment when pressure is applied to the entire device, including the pentacene channel and the source/drain contact regions; (b) Transfer characteristic showing the pressure and no-pressure states [78].

They explained that the observed changes in the drain current as a function of the applied force resulted from alterations in the distribution of trap states near the insulator/semiconductor interface. However, a significant limitation of these devices was their reliance on non-flexible (glass) substrates, which restricts their potentiality for wearable applications such as electronic skin.

In the field of electromagnetic signal detection, which spans visible light to X-rays, applications in biomedical imaging/sensing and optical communications are being pursued [79]. In 2020, Temiño et al. studied the mechanisms of X-ray photoconversion using 6,13-bis(triisopropylsilyl)ethynyl)pentacene (TIPS) as OSCs thin films (as shown in **Fig. 1.20**) [80].

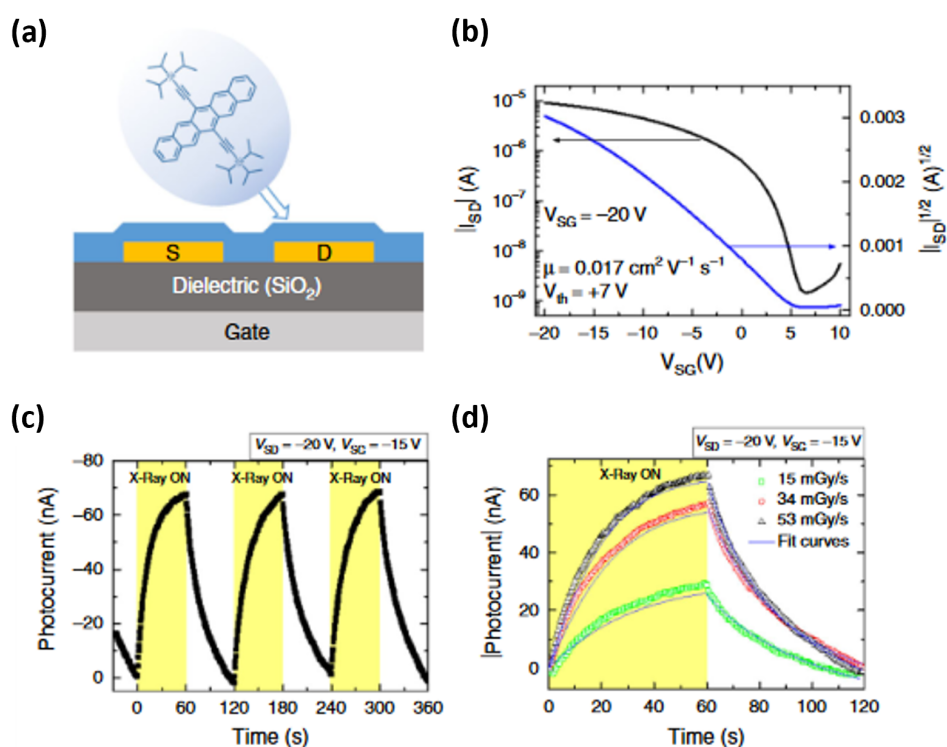


Figure 1.20 (a) Schematic representation of the OFETs. (b) Transfer characteristics in the saturation regime. (c) X-ray induced photocurrent response of a device upon three on/off switching cycles employing a dose rate of 53 mGy s^{-1} . (d) Experimental and fitted curves of the response of the same device for three different dose rates of radiation [80].

They found that decreasing the grain size and increasing the number of grain boundaries in the semiconductor material, increases the density of electron trap states. This enhancement in electron trap density significantly boosts the photoconductive gain for X-ray-induced photocurrents. Additionally, the incorporation of Polystyrene (PS) into the semiconductor solution mitigates the density of hole traps at the interface, resulting in improved charge carrier mobility and, subsequently, elevated device sensitivity. Indeed, the detectors developed through Bar-Assisted Meniscus Shearing (BAMS) technique have achieved a very high sensitivity of $1.3 \times 10^4 \mu\text{C}/\text{Gy} \cdot \text{cm}^2$ thanks to the morphology of the active layer and enhance OFETs mobility. Additionally, these detectors demonstrate an exceptionally low minimum

detectable dose rate of $35 \mu\text{Gy/s}$. The results of this work open up the possibility of employing organic large-area direct detectors for X-ray radiation in practical applications.

1.5.3 Objectives

This work was focused on the development of high-performance Organic Field-Effect Transistors (OFETs) using blends of p-type small molecule Organic Semiconductors (OSCs) and insulating polymer binders. These are processed through a solution-based deposition technique known as Bar-Assisted Meniscus Shearing (BAMS). The primary aim is to understand how various fabrication parameters impact the morphological and structural aspects of the active layer, consequently influencing the electrical performance of the OFETs.

The specific objectives are:

1. **Exploring TOF-SIMS in Thin Film Characterization:** Employ Time-of-Flight Secondary Ion Mass Spectrometry (TOF-SIMS) to analyze organic active layers comprising diverse small molecule OSCs. The focus is to assess the morphology and structure of thin films, as well as evaluate the reproducibility and performance of OFETs through this advanced analytical technique.
2. **Molecular Contact Doping:** Address OFETs with high contact resistance, exploring the molecular contact doping method to reasonably boost the electrical performance. This involves the optimization of doping and the assessment of the stability of devices with doped OSCs.
3. **Vertical Structure Investigation:** Explore the nanoscale vertical structure of OSCs-insulating polymer thin films. The goal is to understand the enhanced performance offered by such blends and the role of the binding polymer. This includes correlating different ink formulations (OSCs:polymer weight ratio) with macroscopic electrical characteristics in OFETs devices.
4. **New Application Exploration:** Identify challenging applications of low-cost solution-processed OSCs:polymer thin films, including flexible electronics and physical input sensing (like high-energy radiation). The focus is on the morphology-performance relationship to enhance device response.

2

Low Energy Ion Beam Analysis on Thin Film Devices

In this second Chapter, an overview of the Time-of-Flight Secondary Ion Mass Spectrometry (TOF-SIMS) technique, used for analyzing thin film devices, is provided. The first part is focused on the sources used for producing secondary ions, with particular attention to the sputtering process, which generates ionized particles from the thin film. Subsequently, the main mechanisms of interaction between the sputtered ions and the TOF-SIMS detector, as well as the most crucial physical quantities related to these interactions, are described. The chapter concludes by highlighting the practical applications of TOF-SIMS on thin-film devices, illustrating the benefits and advantages of TOF-SIMS for studies similar to the ones of this work.

2.1 General Principles

Secondary Ion Mass Spectrometry (SIMS) is a powerful technique capable of characterizing the molecular composition of hybrid stacked materials with extreme surface sensitivity (1 nm sampling depth) and achieving a lateral resolution down to a few hundred nanometers. In the last decade, SIMS, due to the ability to reveal contaminations and diffusion phenomena [81, 82], has been widely used to characterize organic devices. This technique primarily involves the detection of charged atoms and molecular fragments ejected from a solid-phase sample's surface when bombarded with heavy particles. Typically, the energy range of these projectile particles is in the order of a few keV [83].

During heavy particle bombardment, various phenomena occur. Particles from the surface are sputtered while the bombarding entities, referred to as the primary species, are either back-scattered or implanted into the target's condensed phase (**Fig. 2.1**). This process of

surface particle sputtering is one of the multiple events taking place during the surface bombardment; other events include the emission of photons and electrons [83].

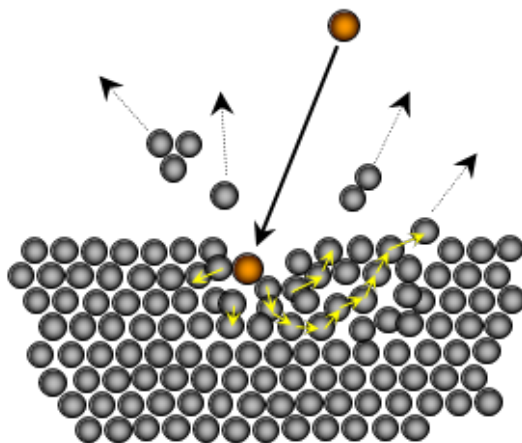


Figure 2.1 Schematic representation of the bombardment process. This illustration depicts the process initiated by the bombardment of 'primary' ions, leading to the desorption of atoms and molecules from the target surface.

The principal aim of SIMS, like any surface analytical technique, is to gather valuable information regarding the structural and compositional state of the sample surface. In the case of SIMS, this information is derived from the emission of secondary ions, which are mass (energy) separated through different combinations of instrumental setups and analyzers.

For accurate interpretation of secondary ion mass spectra, it is fundamental to understand the processes that lead to the emission of charged particles from an ion-bombarded solid. Primary particles impacting on a target, not only transfer energy and momentum at the impact point but also induce changes in the lattice structure of the sample resulting in surface material loss.

The fundamental equation for the secondary ion current of a chemical species m in SIMS is given by [84]:

$$I_m = I_p y_m \alpha q_m \mu \quad (2.1)$$

where:

- I_m represents the secondary ion current of a specific chemical species m . In the context of SIMS, this is the measured current due to ions of a particular element or molecule sputtered from the surface of the sample being analyzed.

- I_p denotes the primary particle flux. In SIMS, a focused beam of primary ions is directed at the sample surface. I_p quantifies the number of these primary ions impacting the surface per unit time.
- y_m represents the sputter yield for species m . This is a measure of the efficiency with which the primary ion beam can eject atoms or molecules of species m from the sample surface. It indicates the average number of atoms or molecules of m sputtered per incident primary ion. This yield is influenced by several factors, including the flux of primary ions, which affects the yield linearly, and the mass, charge, and energy of the primary particles, which affect it nonlinearly. Additionally, the crystallinity and topography of the sample, as well as the angle of incidence of the ion beam relative to the surface normal, are crucial in determining the sputter yield.
- α is the ionization probability. When atoms or molecules are sputtered from the sample surface, they may or may not be ionized. This probability reflects how likely it is that a sputtered atom or molecule of species m becomes ionized, and hence detectable in SIMS.
- q_m is the fractional concentration of species m in the target surface region. It represents the abundance or concentration of the species m in the area of the sample being bombarded by the primary ion beam.
- μ accounts for the transmission yield of the analysis system. It encompasses the efficiency with which the mass spectrometer system used in SIMS detects and transmits the ionized species m to the detector. This factor includes the efficiencies of ion extraction, focusing, and detection in the SIMS instrument.

This relationship is essential for quantitative analysis in SIMS, allowing researchers to infer the concentration of various elements or compounds on the surface or within thin layers of the sample based on the detected secondary ion currents.

2.2 Ion-Solid Interaction

Ion-solid interactions involve a series of complex processes triggered when ions collide upon a surface. These interactions initiate a dynamic energy transfer to the target atoms, characterized by a multifaceted set of phenomena [85, 86].

One of the primary phenomena in this interaction is the collision cascade. This occurs when incoming ions engage multiple collisions upon striking the target surface. Each collision has the potential to generate further collisions, creating a cascade effect. This cascade is a

pivotal factor in determining the number of recoils initiated in the target by the ion probe, thereby influencing key aspects such as the distribution of damage within the target, atomic transfer processes, and mixing in compound targets. The collision cascade is a critical mechanism, as it shapes the outcome of the ion bombardment, affecting the physical and chemical properties of the surface.

Another significant phenomenon is the scattering of ions [84]. As ions interact with the target, a portion of them may be scattered back from the surface (back-scattering) or pushed forward deeper into the material (forward-scattering). While some ions scatter, the majority of the ions lose their energy gradually and come to rest within the bombarded sample. This process of ion implantation can alter the material's properties and this effect has to be carefully considered in applications such as doping in semiconductor manufacturing.

The interaction of ions with the solid surface also leads to topographical changes [87]. The energy imparted by the ions can modify the surface at various scales, ranging from the creation of atomic-scale vacancies to the formation of large-scale structures like craters. These topographical changes are not only indicative of the energy and nature of the ion bombardment but also have significant implications in applications like microfabrication and surface texturing.

Sputtering is another fundamental aspect of these interactions [88]. Energetic recoils, generated near the surface, play a significant role in the sputtering process of the target material. This process involves the ejection of atoms or molecules from the surface, a phenomenon that is central for the operation of techniques like SIMS. Sputtering can provide valuable information about the composition and structure of the target material.

In addition to these primary processes, ion-solid interactions involve numerous other subsidiary interactions that modify the target during irradiation. These include the generation of secondary electrons, photon emission, and radiation-induced chemical changes. The understanding of all these process aspects is crucial for the proper interpretation of the effects and outcomes of ion-solid interactions. This is particularly important in applications such as SIMS, where the nature of ion-solid interactions directly influences the analytical results.

Overall, the study of ion-solid interactions encompasses a wide range of physical and chemical phenomena. Each of these plays a crucial role in determining the outcome of the interaction and has specific implications in various scientific and industrial applications. The ability to control these interactions is a key factor for further potential development in areas ranging from material analysis to surface engineering.

2.2.1 Scattering Cross Section

In TOF-SIMS analysis, a comprehensive understanding of the scattering cross-section is essential [85]. In such analysis, by approximation, the target is considered as consisting of free atoms at rest, particularly when the energy of primary particles far exceeds the binding and kinetic energies of the target atoms. This approximation allows the simplification of target-probe collisions to binary interactions between two particles, which can be adequately described by classical mechanics.

Usually, in collisions, especially those involving heavy particles, a significant transfer between translational and electronic energy occurs. Such interactions are not entirely elastic as the energy transferred to electronic states must be considered. However, in a first approximation, electronic and nuclear interactions are often treated as independent due to their different energy scales.

The collision cascade model is fundamental in understanding SIMS analysis [86]. It posits that a target atom, when hit by an incoming particle such as an ion, is propelled with a certain velocity, initiating a series of collisions - a cascade. A critical aspect of these interactions is the deflection angles and impact parameters. The deflection angle θ of a particle, which arrives with an impact parameter p , can be calculated based on the repelling potential between the two interacting particles. The scattering cross section is defined as $d\sigma = 2\pi p dp$.

Beyond the specific trajectories, the statistics of energy transfer during these collisions are considerably interesting. The cross-section $\sigma(E, T)$ for energy transfer between T and $T + dT$ can be deduced from the interaction potential of the colliding particles.

From the power-law potential approximation, the scattering cross-section can be estimated. This approximation assumes that the interaction potential between the particles follows a simple power law with respect to their separation distance. It simplifies the complex interatomic forces into a more manageable form, making it possible to derive useful expressions that describe the behavior of colliding particles. This estimation leads to expressions involving constants that are related to the mass and atomic charge of the colliding atoms. The collision probability dP and the cross section $\sigma(E, T)$ can be estimated from these considerations, enabling a quantitative understanding of collision processes in SIMS.

In addition to elastic and inelastic collisions, secondary ion mass spectrometry also involves considerations of ionization probability and sputtering yields [88]. The ionization probability, which determines the likelihood of a sputtered atom becoming ionized, is influenced by several factors, including the atom's ionization energy and the energy imparted by the collision. The sputtering yield, which indicates the number of atoms or molecules

ejected from the surface per incident ion, depends on the incident ion's energy and the material properties of the target.

The interaction of primary ions with the target surface in SIMS leads to the emission of secondary ions, which carry valuable information about the surface's composition. The process of ion emission and the subsequent mass spectrometric analysis are influenced by the scattering cross-section, as it determines the energy distribution and trajectories of ejected particles. This understanding is crucial for optimizing SIMS conditions and interpreting accurately the spectra, particularly in applications involving delicate surface structures or thin films where precise depth profiling is required [84].

Scattering cross section in TOF-SIMS is a fundamental aspect that underpins the accuracy and reliability of the analysis. A thorough understanding of the collision mechanics, energy transfer, and subsequent ionization and sputtering processes is decisive for the effective application of SIMS in material analysis.

2.2.2 Emission Phenomena

Ion-solid interactions, such as those in SIMS, involve a range of emission phenomena when a target sample is bombarded with particle or ion beams [84]. One of the primary observations is the scattering phenomenon, where ions either scatter directly from the surface or after partially penetrating the target. In the case of thin film targets, a fraction of these ions may also transmit through the material.

Electron emission is another key phenomenon, especially prevalent at low ion energies. This process occurs through Auger processes, leading to potential emission at the surface, or by kinetic emission, which happens if the ion's kinetic energy is sufficient for inner-shell ionization of atoms in the solid.

Furthermore, the target or exiting particles in excited states can emit electromagnetic radiation, which spans a broad range from infrared to X-ray regions. This radiation emission is a critical aspect of the interaction, providing valuable insights into the energy states of the particles involved [89].

A particularly significant phenomenon observed in SIMS is the ejection of atoms, known as sputtering, which results from collisions that impart sufficient energy to atoms. The sputtered particles can be elemental atoms, molecules, clusters, or charged ions, and they may exist in either ground or excited states.

Sputtering, especially if involving the emission of secondary ions, is a fundamental process in SIMS analysis [88, 89]. The mechanisms of sputtering, triggered by particles with energies ranging from a few electron volts (eV) to several mega-electron volts (MeV), are predominantly understood. In the energy range of 100 eV to keV, sputtering is typically the

result of atomic collisions initiating a collision cascade. When dealing with ion beams of MeV energies, the exchange of energy with electrons plays a significant role.

In crystalline targets, sputtering is highly influenced by the lattice structure. The generation of charged species, or secondary ions, is central to the operation of SIMS. The yield of these secondary ions from a sputtered surface species is determined by both the sputter yield and the probability of ionization. Although these processes occur almost simultaneously, they are often considered separately for empirical modeling purposes.

The sputter yield is a critical parameter in SIMS, indicative of the amount of sample erosion. It is influenced by a variety of factors, including the atomic mass of the projectiles, the chemistry of the target, and the energy of the bombardment. The yield can vary significantly based on the collision regime, which might be a single knock-on, linear cascade, or spike regime. In crystalline materials, factors like surface roughness and the crystallinity of the target affect the angular distribution of the sputter yield.

A deep understanding of these emission phenomena is essential to interpret accurately TOF-SIMS analysis results. The interplay between sputtering and ionization processes, along with the effects of various collision regimes and the properties of the target materials, provides a comprehensive understanding of the characteristics of material surfaces under ion bombardment.

2.2.3 Secondary Ion Formation

Secondary ion formation in SIMS is a complex process significantly influenced by electron (or cation) exchange between emitted species and the bombarded target surface. Ion formation, fundamental for SIMS working principle, is a complex phenomenon. The ionization process, less tractable from a theoretical perspective than sputtering, involves the dynamic emission of atoms and multi-atomic clusters from the bombarded surface, and their subsequent ionization mechanisms. This section briefly outlines the main theoretical approaches to secondary ion formation.

In most cases, over 99% of the sputtered species are neutral [84]. The probability of a sputtered particle escaping the surface as an ion is determined by the relative probabilities of ionization and de-excitation crossing the near-surface region. This ion yield is dependent on the electronic properties of the matrix, the so-called matrix effect. In metals, for instance, electronic transitions are rapid, with de-excitation being a high-probability event during the brief time it takes for a sputtered particle to travel through the near-surface region.

The ionization probability, approximated by the equation:

$$P \approx \frac{2e^{-\pi(\epsilon_a - \epsilon_F)}}{\pi \hbar \gamma_N v} \quad (2.2)$$

where ϵ_a and ϵ_F are the energies of the ionized state and the Fermi level respectively, v is the velocity of the emerging atom, and $1/\gamma_N$ is the distance over which the level width decreases to a fraction of its bulk value, is also influenced by molecular covalent bonding in more complex samples.

Singly charged atomic ions, small cluster ions, and various structural ions are generated by the bombardment of an inorganic solid with low doses of keV primary ions. These structural ions, of particular interest for molecular speciation in mass spectra, include atomic ions (ionized elements), cluster ions (small polyatomic secondary ions), and molecular ions (corresponding to intact molecules after the removal of one electron). Adduct ions involve the attachment of atomic or stable cluster ions to one or several neutral molecules, forming monomeric or polymeric adducts. Fragment ions are generated from molecular or adduct ions through structure-specific fragmentation mechanisms, providing supportive information for direct speciation.

Despite numerous studies, the exact mechanism leading to the detection of ions from the impact of a keV projectile remains not entirely clear. The interaction of a primary ion with the solid introduces complex processes involving energy deposition, dissipation, recoil, sputtering, and ion formation. From an experimental point of view, the separation of a single step in this sequence is challenging, as altering one parameter tends to affect all the others.

Two qualitative models provide frameworks for understanding secondary ion generation from molecular species. The Nascent Ion-Molecule Model, developed by Gerhard and Plog [90], focuses on cluster ion formation, primarily from oxide surfaces, and suggests that rapid electronic transitions in the surface region neutralize all the ions before they can escape. This model has evolved into the Valence Model, which acknowledges partial charges on cations and anions that deviate from pure ionic values.

The Desorption Ionization Model, introduced by Cooks and Busch [91], emphasizes the importance of vibrational excitation in emitting clusters or molecular ions from organic materials. It theorizes that a variety of ion emission processes are plausible in complex, non-elemental targets.

In summary, secondary ion formation in SIMS is a multi-faceted and complex process, influenced by the electronic state of the surface, the chemical state of the sample, and complex theoretical models. Understanding these processes is crucial for interpreting the large amount of detailed data obtained from SIMS analysis.

2.3 Secondary Ions Detection and Analysis

SIMS, as extensively discussed, relies on the analysis of atomic and molecular secondary ions emitted from a surface under primary bombardment. The analysis of charge-to-mass ratios of these secondary ions provides direct insights into the chemical composition of the uppermost monolayer of the bombarded surface [84].

The efficacy of SIMS analysis is conditioned not only by the total amount of material available and the efficiency of the ionization process during sputtering but also by the mass spectrometer employed. The performance of the mass analyzer is a function of several key parameters: transmission capability, mass resolution, and accessible mass range. Continuous instrument improvement has been really important for advancements in SIMS analytical applications and fundamental research. Presently, SIMS is regarded as one of the most potent techniques for surface and low-dimensional system analysis. It offers features like the detection of all elements (including hydrogen), isotope sensitivity, molecular information, and a low detection limit.

Initially, SIMS faced limitations due to the performance of available instrumentation. The fact that low-dose SIMS could serve as a surface-sensitive technique was first noted by Benninghoven [92, 93]. His results demonstrated that many components in the uppermost monolayer of samples could be sputtered with high enough yields to generate useful spectra. This low-current density analysis mode, known as static SIMS, is considered non-destructive as long as the primary ion fluence remains below the static limit of 10^{12} ions/cm². At this limit, the probability of a target atom being bombarded twice is extremely low, ensuring that the surface remains undamaged and the SIMS characterization reflects the pristine surface.

2.4 Instrumental Setup

The TOF.SIMS⁵ instrument, commercialized by IONTOF GmbH (Muenster, Germany), is a leading product in the SIMS line and is currently operational at Roma Tre University (Fig. 2.2). In Fig. 2.3, a schematic representation of the principal components of TOF-SIMS is reported.

The TOF.SIMS⁵ instrument at Roma Tre University stands out for sophisticated ion generation and analysis capabilities. Central for the functionality are two versatile ion sources:

- Liquid Metal Ion Gun (LMIG): exclusively used for surface analysis, the LMIG is adept to generate precise monoatomic Bi⁺ⁿ ion beams. This feature allows for detailed

surface characterization, providing critical insights into the topmost layers of the sample with high spatial resolution.

- Cesium ion source: complementing the LMIG, the cesium ion source, Cs^+ , is particularly effective for depth profiling. Its etching capability is crucial for uncovering subsurface layers and analyzing material composition at varying depths.



Figure 2.2 Photograph of TOF.SIMS⁵ equipment installed at Roma Tre University

Additionally, the TOF.SIMS⁵ is equipped with an electron gun, commonly referred to as a flood gun, which plays a pivotal role in charge compensation during analysis. This feature is essential for maintaining sample integrity, especially when examining insulating materials.

The instrument's design is also noteworthy. The ion sources are strategically positioned at a 45° angle relative to the sample surface, optimizing ion interaction and sputtering efficiency. The heart of the system is the Time-of-Flight (TOF) analyzer, an advanced component responsible for the precise separation and detection of ions based on their mass-to-charge ratio.

Further enhancing its performance, the TOF.SIMS⁵ operates within an ultra-high vacuum environment. This is achieved and maintained at a pressure level of approximately 10^{-9} mbar, thanks to a turbo-molecular pump coupled with a titanium sublimation cryogenic

pump. Such a vacuum condition is essential for minimizing contamination and ensuring the accuracy of SIMS analysis.

The following sections of this chapter will provide a more comprehensive examination of these sophisticated components, elucidating their contributions to the TOF.SIMS⁵ overall functionality and performance.

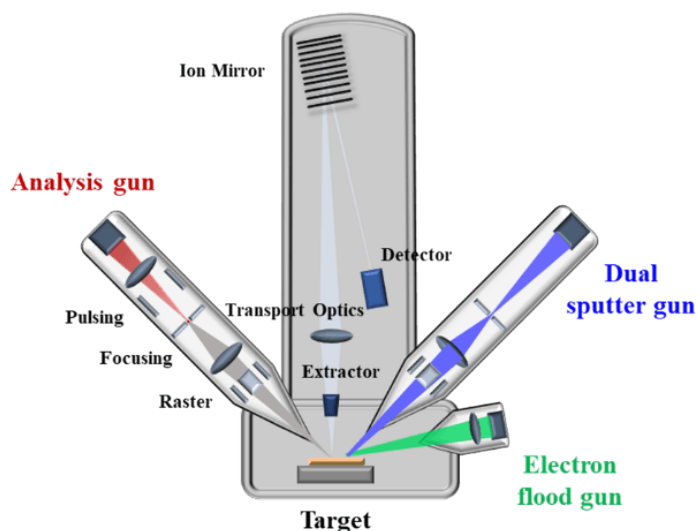


Figure 2.3 Schematic representation of the TOF.SIMS⁵ equipment configuration.

2.4.1 Primary Ion Beam Column

The comprehensive assembly of components within the primary ion beam column is illustrated in **Fig. 2.4**. The ion beam's energy is primarily determined by the emitter's potential. Ion emission begins once the field strength at the needle tip exceeds the critical threshold. This field strength is regulated by the extractor voltage, which, along with the suppressor voltage, can be finely adjusted either manually by the user or automatically to sustain a consistent emission current. Beam alignment is achieved using three X/Y deflection systems. These systems guide the ions through three apertures in series. Current measurements through apertures 1 and 2 assist in identifying optimal focusing parameters. Further fine-tuning of the focusing, particularly through the blanking aperture, is accomplished by monitoring the current impacting the target, which can be done using a Faraday cup or a conducting sample. For all types of analysis, the beam must be pulsed. This pulsing occurs at the pre-chopper and chopper stages. Here, the beam mass filtering also takes place, effectively blocking ions of differing masses. These ions exhibit varied velocities at the same beam energy, with the

predominant beam species being Bi^+ and Bi_3^+ . The maximum energy achievable by the beam for single-charged species is 30 keV.

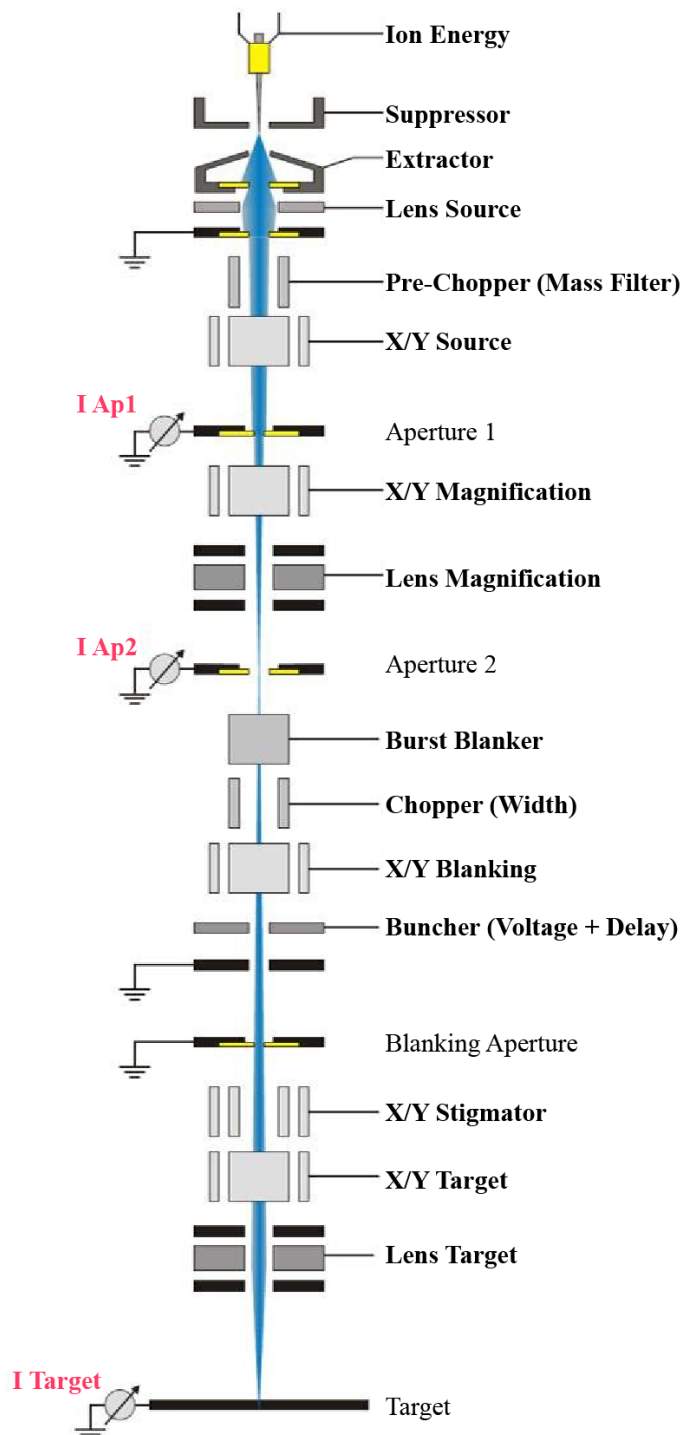


Figure 2.4 Schematic illustration of the components present in the primary ion beam column of the TOF.SIMS⁵. Adapted from the IONTOF help manual.

2.4.2 Dual-Source Ion Column

The dual-source ion column is equipped with two distinct ion sources: an electron impact source for generating C_{60}^+ ions, and a thermal sputtering ion source for producing Cs^+ ions. A schematic of the dual-source column, highlighting these main components, is presented in Fig. 2.5.

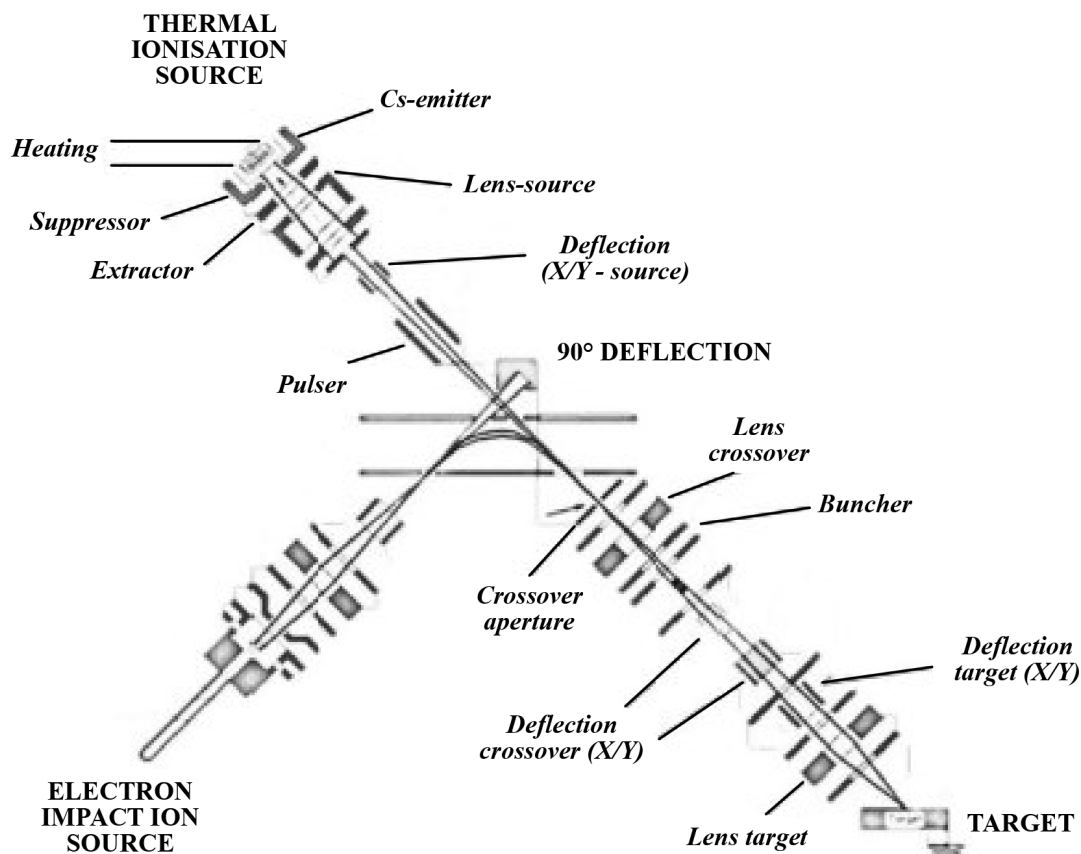


Figure 2.5 Schematic illustration of the components present in the dual-source ion column of the TOF.SIMS⁵. Adapted from the IONTOF help manual.

Beam selection within this column is facilitated by a 90-degree deflection magnet. The operations of focusing, bunching, and pulsing in this column are similar to those in the primary ion beam column. The design and functionality of these components allow for precise control and manipulation of the ion beams. Typically, these ion sources are predominantly utilized as etching guns in in-depth profiling modes, as will be discussed in subsequent sections. However, they also have the flexibility to be employed as primary ion guns for specific applications. This versatility is essential for the varied analytical requirements encountered in SIMS.

The typical energy settings for the C_{60}^+ and Cs^+ beams are 1 keV and 3 keV, respectively. These energy levels are precisely calibrated to suit the specific requirements of the analysis being conducted, ensuring optimal performance and results accuracy.

2.4.3 Electron Flood Gun

Insulating samples are prone to electrostatic charging during SIMS analysis, mainly due to primary ion bombardment and subsequent electron emission. This charging effect can significantly reduce or even eliminate the detection of secondary ions, thereby adversely affecting the signal quality. Localized positive charging on the sample surface can alter the energy of the secondary ions and distort their trajectories. This issue arises because insulators lack sufficient electrical conductivity to redistribute the accumulated charge.

To face this charging effect, samples can be irradiated with low-energy electrons, which are carefully calibrated to avoid any sample damage. Typically, this irradiation occurs between the pulses of primary ions. In this regard, our TOF-SIMS instrumentation includes a low-energy electron gun, adjustable from 0 to 21 eV. The electron energy is controlled by modulating the potential of a filament, which is encapsulated within a shielded electrode.

When the electron flood gun is activated for charge compensation on an insulating sample, adjustments to the analyzer settings are necessary. Specifically, the reflectron voltage must be adjusted to take in account the shift in the sample surface potential from the ground. The modification in the surface voltage V_S is compensated by changing the reflectron voltage V_R by a value $\Delta U_{\text{surface}}$, which is non-zero for insulating targets under ion bombardment. This adjustment ensures accurate analysis correcting the potential shifts induced by surface charging.

2.4.4 Analyzer

The Time-of-Flight (TOF) analyzer offers unique characteristics, making it an ideal detection system for SIMS. Its principle lies in separating secondary ions based on their mass-to-charge ratio (m/z) and determining their masses by the time taken to travel a known distance L in a field-free flight tube. This time is measured after acceleration by an extractor to a common energy E (**Fig. 2.6**).

The relationship between energy E , flight time t , and other parameters is described by the equation:

$$E = zU = \frac{mv^2}{2} = \frac{mL^2}{2t^2} \quad (2.3)$$

where z is the ion charge state, U the extractor potential, and v the velocity of the secondary ion. Consequently, lighter ions, with higher speeds, reach the detector faster than heavier ions:

$$t = L\sqrt{\frac{m}{2E}} = L\sqrt{\frac{m}{z \cdot 2U}} \quad (2.4)$$

The TOF resolution, or the width of a secondary ion packet, is influenced by several factors, such as the angular spread of ion trajectories and the detector's effective depth. The primary source of resolution degradation, however, is the energy spread (ΔE) of ions with the same mass.

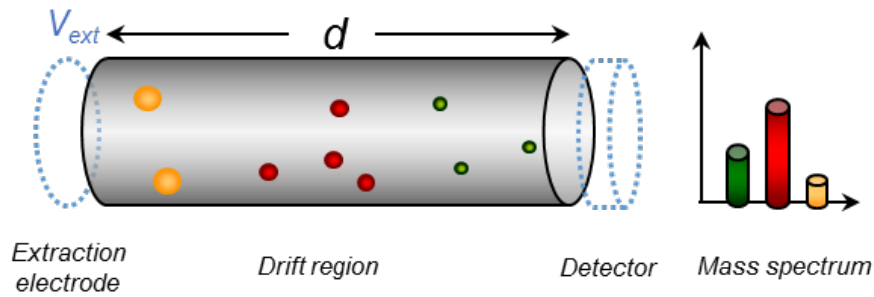


Figure 2.6 Schematic representation of TOF analyzer.

The resolution R is determined first-order by the energy spread:

$$R \equiv \frac{t}{2\Delta t} = \frac{m}{\Delta m} = \frac{E}{\Delta E} \quad (2.5)$$

To address resolution issues, the concept of an ion mirror was introduced. Under an appropriately designed quadratic field, the detection time becomes independent of the initial kinetic energy, minimizing mass resolution degradation. However, the practical realization of such ion mirrors faces challenges like reduced ion transmission, leading to the adoption of single and double-stage reflectrons. These designs involve two field-free regions and a reflectron where ions experience at least one linearly increasing potential $U = ax$ step. This setup guarantees first-order focusing of the initial energy spread of secondary ions of the same mass, contributing to improved resolution.

Delayed extraction and post-acceleration voltages are other design strategies implemented to enhance resolution in TOF-SIMS.

2.5 ToF-SIMS Analysis Mode

The TOF-SIMS instrumentation at our laboratory boasts advanced raster scanning capabilities. It can precisely adjust the primary ion beam over a maximum area of $500 \times 500 \mu\text{m}^2$. During the scanning process, the sample surface is effectively divided into numerous pixels.

In all analysis modes (**Fig. 2.7**), a comprehensive mass spectrum is collected and recorded for each pixel. This detailed data acquisition forms a raster pattern across the scanned area. Additionally, the instrumentation allows for the post-reconstruction of the collected data sets. This feature is particularly useful for generating detailed spatial distributions and for in-depth analysis of the sample surface.

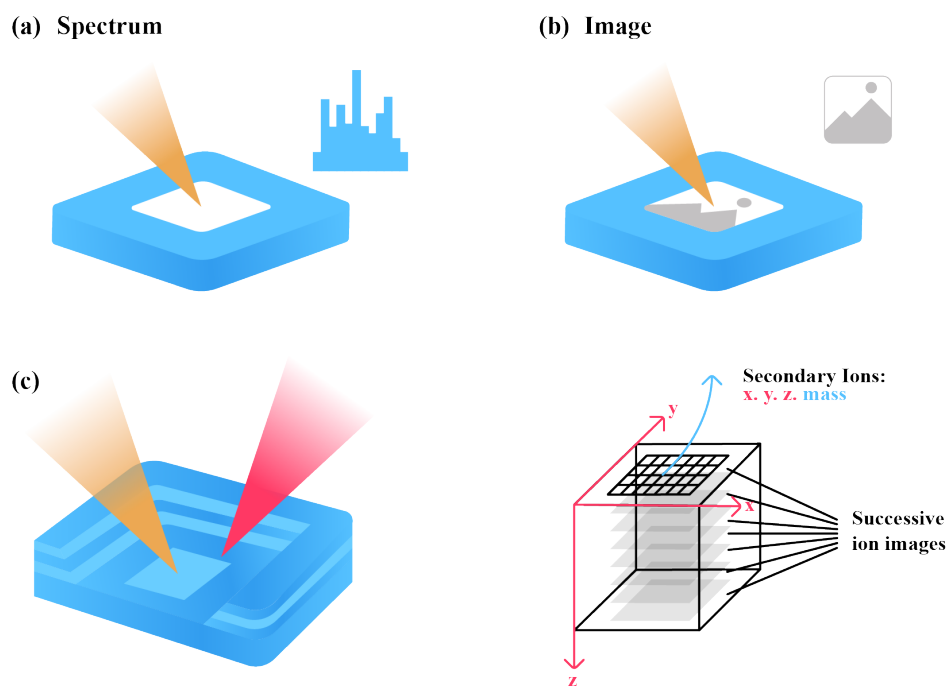


Figure 2.7 Analysis modes with TOF-SIMS. **(a)** Surface Spectrometry (static SIMS), **(b)** Surface Imaging (static SIMS), **(c)** Depth profiling in-plane (2D), **(d)** Depth-profiling in-depth (3D) TOF-SIMS data set reconstruction.

2.5.1 Static SIMS

In surface spectrometry experiments using TOF-SIMS the primary interest often lies in obtaining a representative mass spectrum of the surface under analysis, rather than in detailed

spatial distribution mapping of secondary ions. To minimize sample damage, the primary ion beam is raster scanned over small areas, with the spectra from all pixels combined into one aggregate mass spectrum.

An important consideration in these experiments is the ion dose limit, which must be carefully managed to avoid significant alteration of the sample's structure or chemistry. In Static SIMS mode, considered quasi-non-destructive, the primary ion dose is kept below a threshold of 10^{12} ions/cm². This limit dictates the endpoint for analysis using metal cluster beams.

The duty cycle, defined as the ratio of beam-on time to real-time in a pulsed ion beam, is a critical factor in these experiments. It is determined by the duration of the ion beam pulses and the repetition rate of pulsing. For example, a continuous 1 nA beam scanning an area of $100 \times 100 \mu\text{m}^2$ would reach the static limit in just over 0.001 seconds. However, if the same beam is pulsed at 10 kHz with 10 ns pulses, the beam is on for only 10^{-4} seconds of each second of real-time, extending the time to reach the static limit to over 100 seconds.

The time T to reach the static limit can be calculated using the formula:

$$T = \frac{A \times q \times 10^{30}}{I \times f \times t} \quad (2.6)$$

where q is the electronic charge (1.602×10^{-19} C), A the analysis area in cm², I the current of singly charged ions in nA, t the pulse length in ns, and f the repetition rate in Hz.

Short primary ion pulses (less than 1 ns) are essential for achieving high mass resolution. In the LMIG operational modes, the high current (Bunched) mode is ideal for this purpose. The buncher unit in the LMIG column consists of two plates, which are grounded when the pulse enters between them. As the pulsed beam passes between the buncher plates, the rear plate is set to a positive voltage, accelerating the ions.

Each pixel of the scanned sample area contains a spectrum, allowing for lateral chemical mapping. In TOF instruments, spatial resolution as low as $0.1 \mu\text{m}$ is routinely achievable. The spatial resolution is determined by the ion-optical column's lenses, apertures, pulsing unit, and electrical supply. Surface imaging TOF-SIMS measurements provide mass-resolved secondary ion images from the topmost atomic layers under the static limit.

The best-suited imaging mode depends on specific analytical requirements, such as lateral or mass resolution, acquisition time, and the dimensional scale of the investigated system. TOF-SIMS analysis encompasses various modes, each tailored to specific analytical needs, balancing between mass resolution, lateral resolution, and acquisition time. This adaptability allows for comprehensive analysis of sample surfaces, providing valuable insights into their chemical composition and structure.

2.5.2 Dynamic SIMS: Depth-Profiling

In-depth analysis using TOF-SIMS techniques is crucial for investigating sub-surface sample regions and characterizing the chemical composition of materials at a detailed level. This method employs a focused ion beam, typically in the keV range, which is rastered over an area larger than the beam size [84]. This rastering technique is essential to form a well-defined sputter crater for analysis. Unlike electron spectroscopy methods, where an independent probe analyzes the crater bottom, TOF-SIMS utilizes the sputtered particles themselves for analysis. This approach, known as dynamic SIMS, is different from static SIMS, which primarily focuses on the analysis of the outermost layer of a solid.

One of the key features of TOF-SIMS sputter depth profiling is the incredibly low detection limit, often in the sub-parts per million (ppm) range. This sensitivity allows for the detection of trace elements and really small variations in the composition. The information depth achievable with TOF-SIMS is typically in the range of 1-2 monolayers, providing an exceptional level of surface detail. Furthermore, the high speed of analysis inherent to TOF-SIMS technology facilitates rapid data acquisition, making it an efficient tool for detailed surface analysis.

The erosion gun and the analysis gun in TOF-SIMS operate in an alternating fashion. The sputtering phase is designed to remove the previously rastered surface, thereby exposing a fresh layer for successive analysis in the next cycle. This regular removal and analysis allow for a systematic examination of the sample's sub-surface layers.

TOF-SIMS's dual-beam mode offers several distinct advantages. The ability to perform parallel detection of all fragments by the pulsed beam is particularly beneficial for Time-of-Flight Secondary Ion Mass Spectrometry detection. Despite the relatively low currents used in the pulsed analysis beam, high sputter yields are achieved, enhancing the efficiency of material removal and analysis. The dual-beam setup allows for the independent adjustment of analysis and sputter parameters, providing greater control over the analysis process. Additionally, the capacity to raster different analysis areas with each beam affords a high degree of flexibility in sample examination.

In the dual-beam setup of TOF-SIMS, two operational modes are commonly employed. The Interlaced Mode involves the near-simultaneous use of both beams, which is particularly employed for conducting samples since TOF-SIMS facilitates data acquisition at high rates. In contrast, the Non-Interlaced Mode separates the operations of the primary ion beam and analyzer from the sputter gun, making it more suitable for insulating samples. This mode allows for a longer interval for charge compensation, crucial for samples that are prone to charging under ion bombardment.

Depth profiling with TOF-SIMS is an indispensable tool for the three-dimensional characterization of multilayer systems, interface analysis, and the investigation of atomic and molecular species migration within the sample. The depth resolution, defined as the interval between 16% and 84% of the maximum intensity of the signal when crossing a planar interface, is a critical parameter in these analyses. It's essential to consider factors like depth resolution and material-dependent sputtering yields for accurate interpretation of the data.

Depth profiling in TOF-SIMS is a sophisticated process requiring careful selection of parameters and conditions. The aim is to minimize the side effects of the profiling process while preserving the integrity of the sample. The technique has become an essential tool in materials science for its ability to provide detailed insights into the composition and structure of materials at the nanoscale. With advancements in TOF-SIMS technology, applications in surface analysis continue to expand, offering unparalleled depth and clarity in understanding material properties.

2.5.3 ToF-SIMS Analysis of Thin Film Devices

The Time-of-Flight Secondary Ion Mass Spectrometry technique offers advantages in the analysis of thin film devices, particularly Organic Field-Effect Transistors [94, 95]. This analysis method stands out due to the ability to combine high lateral resolution surface analysis with nanometer-scale sensitivity in-depth profiling [96].

One of the critical aspects of TOF-SIMS in thin-film device analysis is the high lateral resolution. This feature allows for detailed surface characterization of OFETs, revealing fine structural details and compositional variations at the microscopic level. Such high-resolution imaging is essential in identifying surface heterogeneities, which can significantly impact the performance and reliability of OFETs [97, 98]. Moreover, TOF-SIMS excels in providing depth profiles with nanometer sensitivity, a crucial factor in analyzing multi-layered thin-film structures like OFETs. This capability enables the precise determination of layer thicknesses, interfaces, and compositional gradients within the device [99]. The technique's sensitivity allows for the detection of even negligible changes in material composition, which can be pivotal in understanding charge transport and trapping mechanisms in OFETs.

The combination of surface and depth analysis offered by TOF-SIMS is particularly beneficial in the study of OFETs. The technique can be employed to investigate the distribution and concentration of dopants, the integrity of organic semiconductor layers, and the presence of potential contaminants that could affect device performance. Furthermore, TOF-SIMS can provide insights into the effects of fabrication processes on the molecular structure of the organic layers, crucial to optimize device design and to improve the performance [99].

TOF-SIMS is an indispensable tool in the analysis of thin-film devices, especially OFETs. Its ability to deliver high-resolution surface imaging alongside detailed depth profiling at the nanometer scale makes it precious in advancing our understanding and development of these complex devices.

Data-Set Analysis

The complexity of the TOF-SIMS dataset, due to ionization yields, matrix effects, and mass overlaps, can generate ambiguities in identifying the characteristic molecular fragments from each layer [100, 101]. Therefore, even when the nominal composition and thickness of each organic device layer are known, an unequivocal identification of characteristic layer fragments among hundreds of peaks is challenging. This is the reason why it is advantageous to develop statistical methods capable of processing data and able to reduce data complexity. Multivariate Analysis (MVA) has shown the ability to overcome the complexity presented by TOF-SIMS data-set.

Among the various techniques under the MVA, Principal Component Analysis (PCA) stands out as particularly effective. PCA is a statistical procedure that transforms a set of observations of possibly correlated variables into a set of values of linearly uncorrelated variables called principal components. This transformation is defined in such a way that the first principal component has the largest possible variance, and each succeeding component, in turn, has the highest variance possible under the constraint that it is orthogonal to the preceding components. The resulting orthogonal components represent the directions of maximum variance in the data, allowing for a dimensionality reduction, while retaining most of the variability in the dataset.

By applying PCA to TOF-SIMS data, we can efficiently reduce the complexity of the data by focusing on the most significant variance-contributing factors. This method facilitates the identification of characteristic molecular fragments and aids in the interpretation of the layered structure of organic devices.

In 2018, Tortora et al., tested PCA as an innovative method for the identification of molecular fragments useful for the OFETs multi-layer structure characterization (**Fig. 2.8**) [95].

PCA in this context is used to analyze the relationship between variables over sputter time, which represents the sample depth. Each principal component has a characteristic profile showing all detected ion signals. Score plots (**Fig. 2.8a**) illustrate depth profiles while loading plots (**Fig. 2.8b,c**) represent related mass spectra. The first three components, covering about 95% of the total variance, distinguish different layers of the OFETs studied. Negative and positive PC1 scores indicate layer composition, with PC2 and PC3 providing

further layer differentiation, including the OFETs surface treatment. These results are in agreement with the depth profile achieved in Tortora et al. work.

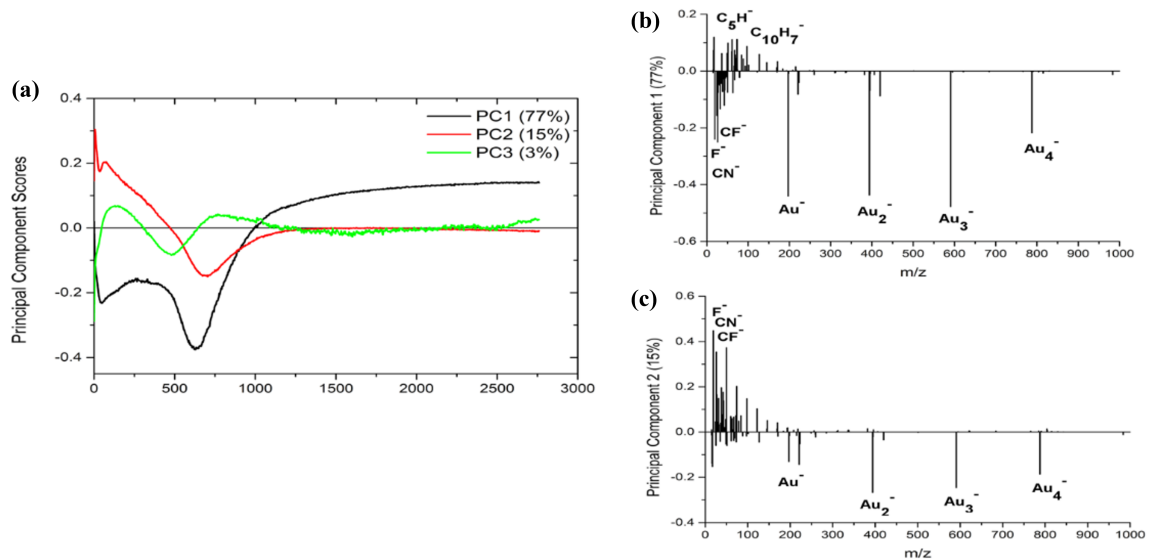


Figure 2.8 PCA model from ToF-SIMS depth profiling data: (a) Overlay of PC1, PC2, and PC3 scores plot; (b) PC1 loading plot; (c) PC2 loading plot [95].

Inspired by this work's use of PCA for depth profiling in TOF-SIMS data analysis, all the data collected during this thesis work were analyzed using firstly PCA. This approach ensures the most comprehensive extraction of information from the TOF-SIMS datasets, enhancing the accuracy of our understanding in each study presented in the thesis.

3

Molecular Contact Doping Effects in OSCs

Molecular contact doping is a highly efficient strategy for reducing Contact Resistance (R_C) in OFETs. This technique is based on the insertion of a dopant layer between the OSCs and the top gold contacts. The main objective of this layer is to decrease the energy barrier necessary for the injection and release of charges, thereby enhancing the device's overall performance.

Despite its efficacy, a significant challenge in the implementation of molecular contact doping is the tendency of the dopant to diffuse towards the OFETs channel over time. This diffusion, resulting in an unintentional doping of the OSCs, adversely affects the on/off switching capability of the device.

To overcome this issue, we applied an innovative approach for the fabrication of OFETs using 2,7-dioctyl[1]benzothieno[3,2-b][1]benzothiophene (C_8 -BTBT- C_8) OSCs. Our method involves the utilization of a solution shearing technique, which has shown encouraging results to control the dopant unintended diffusion and to promote the integration of Polystyrene (PS) into the blend as a dopant diffusion inhibitor, thereby improving device stability and performance.

3.1 Introduction and Objectives

In the last two decades, small molecule Organic Semiconductors have garnered significant interest in organic electronics [36]. Their applications span a range of cutting-edge technologies, including organic photovoltaics, Organic Light-Emitted Diodes, and Organic Field-Effect Transistors. These materials have played a central role in the development of flexible, lightweight, and cost-effective electronic devices.

Among the OSCs, derivatives of benzothieno[3,2-b][1]benzothiophene (BTBT) have been identified as benchmark materials, particularly in OFETs applications [102, 103]. These derivatives are recognized for their excellent electrical performance and high stability under ambient conditions. A standout compound in this family is 2,7-dioctyl[1]benzothieno[3,2-b][1]benzothiophene (C_8 -BTBT- C_8), which is highly required due to its combination of printability with low-cost techniques and high field-effect mobility [104].

Despite the fabrication of high-performance OFETs based on the BTBT derivatives presents many advantages, also several challenges have to be faced, mainly due to the high Contact Resistance (R_C) of devices. This resistance results from the energy mismatch between the gold source/drain contacts and the OSCs highest occupied molecular orbital, typically around -5.4 eV [105]. This mismatch creates energetic barriers for charge carrier injection and release, leading to a significant reduction of the device mobility. Consequently, the identification of effective methods to reduce contact resistance has become a critical research aspect to optimize the device performance, especially for high-frequency OFETs applications [106].

Several approaches have been adopted. One methodology foresees the modification of the metal contacts in bottom-contact devices with molecular self-assembled monolayers to tune their work function. Chemical doping of the OSCs has also been explored as a promising opportunity for improving OFETs Contact Resistance [47, 48]. However, it could be complex to achieve full control over the doping level, and the excess of doping could lead to over-doped devices with high off-currents, affecting the OSCs crystallinity and transport properties.

An alternative and widely employed strategy is molecular contact doping, with the insertion of a dopant layer between the OSCs and the top gold contacts [107]. This method has been extensively and successfully employed with BTBT derivatives in p-type OFETs. A common electron acceptor molecule used for this purpose is 2,3,5,6-tetrafluoro-7,7,8,8-tetracyanoquinodimethane (F4TCNQ). However, the limited life stability of contact-doped devices due to dopant diffusion into the OFETs channel remains a significant concern. This diffusion hampers the on/off switching capability of the device.

A recent approach, reported in the literature to address this issue, involves the evaporation of a layer of a “dopant-blockade” molecule on the OFETs channel region to create barriers against dopant movement [108].

The observed decrease in the R_C in organic semiconductor devices, particularly in those employing small molecule organic semiconductors such as C_8 -BTBT- C_8 , can be attributed to two main mechanisms. The first mechanism involves doping at the contacts, which effectively increases the charge density within the depletion region, consequently thinning it,

as illustrated in **Fig. 3.1**. This increase in charge density at the contacts facilitates charge tunneling, thereby reducing the interface R_C (R_{int}) [109].

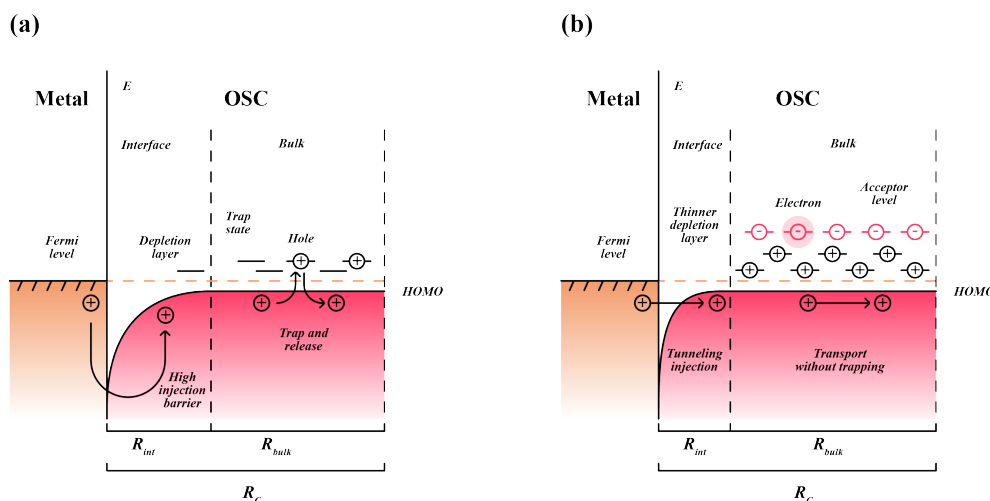


Figure 3.1 Schematic energy diagrams of the organic semiconductor/metal contact: **(a)** without doping, the depletion layer is very thick and hole injection is by thermal activation through a high-energy barrier, **(b)** with acceptor doping, so that the depletion thickness decreases, the tunneling injection becomes predominant, and trap states are occupied. Adapted from [109].

The second mechanism involves the reduction in the density of traps at the organic semiconductor/metal interface. This reduction in trap density effectively decreases the bulk R_C (R_{bulk}). As indicated in **Fig. 3.2**, considering the Lowest Unoccupied Molecular Orbital and the Highest Occupied Molecular Orbital levels of F4TCNQ and C_8 -BTBT- C_8 respectively, it is plausible that most in-gap trap levels of the organic semiconductor are filled through a charge transfer process [105]. This charge transfer facilitates significantly the charge transport through the bulk region. Moreover, the low energy of the C_8 -BTBT- C_8 HOMO prevents the generation of additional mobile charges in the semiconductor; in other words, the semiconductor does not undergo significant oxidation. This aspect is particularly noteworthy as it enables the enhancement of injection efficiency without increasing the off-current which is a challenge often encountered with other OSCs with higher HOMO energies, such as pentacene (~ -4.8 eV) [105].

A critical aspect of the doping of Organic Semiconductors is the distinction between selective and bulk doping. Selective doping refers to the scenario where the semiconductor film is doped only at specific areas, such as the OSCs/electrode interface, while bulk doping

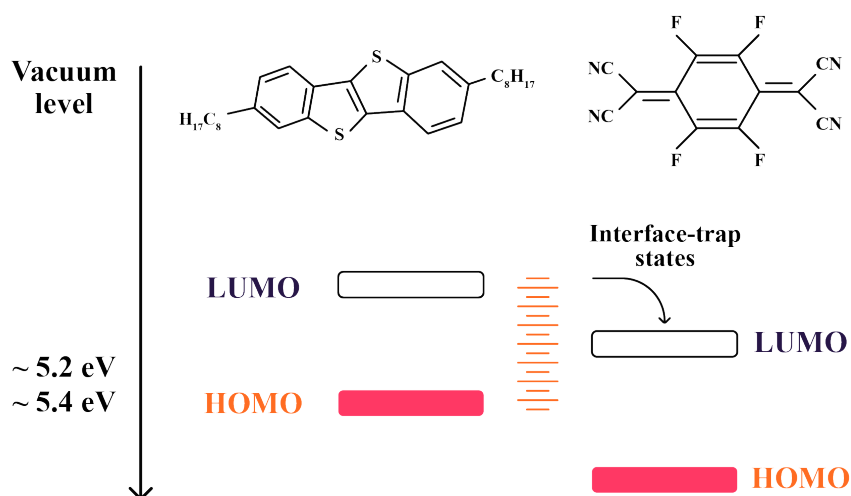


Figure 3.2 Energy diagram showing the charge-transfer between C₈-BTBT-C₈ and F₄TCNQ, thus filling the in-gap traps levels at the interface of the OSCs. Adapted from [105].

implies homogeneous doping throughout the semiconductor film. The choice between these two types of doping largely depends on the doping methodology employed [110].

The methodologies for doping Organic Semiconductors can be broadly categorized into three types: thermal evaporation, solution-based, and physisorption processes. Each of these methods presents advantages as well as limitations, impacting the doping uniformity and effectiveness. Understanding the mechanisms behind the decrease in R_C in OSCs devices is a crucial aspect of optimizing their performance. The ability to control the doping process, whether selective or bulk, plays a significant role in the overall efficiency and stability of these devices. These insights are fundamental for the advancing of Organic Electronics, particularly for the development of high-performance Organic Field-Effect Transistors and other Organic Semiconductors-based devices [111].

In our research, we aim to develop an innovative and straightforward method to significantly inhibit dopant diffusion towards the OSCs channel in OFETs that are based on C₈-BTBT-C₈ and contact doped with F₄TCNQ. Our approach involves blending the OSCs with PS of various molecular weights (M_w). This strategy was deemed able to allow precise control of the dopant distribution on the surface as well as in-depth.

Through our planned investigations using TOF-SIMS, we expected to discover that in thin films of OSCs blends with High-Molecular-Weight Polystyrene, the dopant remained significantly confined to the contact areas. In such case, an enhanced long-term stability of the devices was hypothesized. This could represent a breakthrough in OFETs technology,

offering an efficient solution to one of the key challenges in OEs: the diffusion of dopants and the dopant impact on device performance and lifetime.

3.2 Device Fabrication

C_8 -BTBT- C_8 and Polystyrene polymer with different molecular weights, specifically PS_{10K} ($M_w = 10,000$ g/mol), PS_{100K} ($M_w = 100,000$ g/mol), and PS_{280K} ($M_w = 280,000$ g/mol), were procured from Sigma-Aldrich. Furthermore, F4TCNQ was sourced from TCI Chemistry. All materials were utilized as received, without any additional purification.

The molecular structures of C_8 -BTBT- C_8 , the dopant F4TCNQ, and the binder polymer PS are shown in **Fig. 3.3a** together with the device structure. OFETs with a bottom-gate top-contact architecture with constant channel width ($W = 4000$ μm) and different channel lengths ($L = 35, 80, \text{ and } 175$ μm) were fabricated.

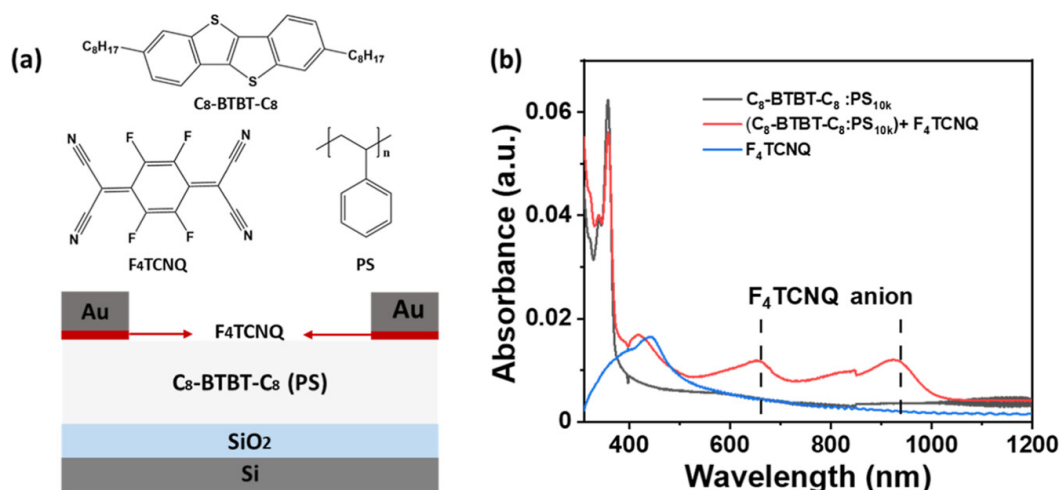


Figure 3.3 (a) Chemical structures of C_8 -BTBT- C_8 , F4TCNQ, and PS and scheme of the OFETs layout. (b) UV-vis of a C_8 -BTBT- C_8 :PS_{10K} film, a F4TCNQ film, and a C_8 -BTBT- C_8 :PS_{10K} after the evaporation on top of 10 nm of F4TCNQ [82].

Solutions were prepared with either pristine C_8 -BTBT- C_8 or a blend of C_8 -BTBT- C_8 and PS in varying molecular weights. The weight ratio of C_8 -BTBT- C_8 to PS was maintained at 4:1 in a 2 wt% chlorobenzene solution. Before the deposition of the OSCs solution, substrates underwent a cleaning process with acetone and isopropanol, three times each, followed by drying under a nitrogen flow.

The fabrication of the OSCs thin films was carried out using the Bar-Assisted Meniscus Shearing technique [80]. This was executed using a home-designed setup under ambient conditions on Si/ SiO_2 substrates (provided by Si-Mat, with SiO_2 thickness of 200 nm and capacitance $C = 17.26 \times 10^{-9}$ F \cdot cm⁻²). As reported in previous studies, 35 μL of the heated

OSCs solution (at 105 °C) was placed between a hot substrate (also at 105 °C) and a steel bar positioned 500 μm above the stage to form a meniscus [112]. Subsequently, the substrate was moved parallel to the bar at a constant speed of 10 mm/s, leading to the formation of a dry film behind the moving meniscus.

For the deposition of F4TCNQ (10 nm) and gold contacts (25 nm), thermal evaporation was employed. The evaporation rates were set at 0.02 nm/s for F4TCNQ and 0.05 nm/s for Au, using a shadow mask to define channel widths ($W = 4$ mm) and lengths ($L = 50, 100,$ and 200 μm). Post contact evaporation, samples devoid of F4TCNQ were stored in dark conditions in air for 7 days. In contrast, samples containing F4TCNQ were subjected to immediate measurements. It was previously reported that F4TCNQ can effectively dope $\text{C}_8\text{-BTBT-C}_8$ films [113]. This was confirmed by recording the UV–vis absorption spectra (measured with a UV-visible spectrometer V-780) of a F4TCNQ film, a $\text{C}_8\text{-BTBT-C}_8\text{:PS}$ blend film, and the same blend film with a 10 nm layer of F4TCNQ evaporated on top (**Fig. 3.3b**). The presence in the latter film of the absorption bands corresponding to the radical F4TCNQ (centered at around 650 and 930 nm) confirmed that the charge transfer between F4TCNQ and $\text{C}_8\text{-BTBT-C}_8$ occurred and, hence, the $\text{C}_8\text{-BTBT-C}_8$ doping was successful [113].

3.3 Thin Films Characterization

The morphological characteristics of the pristine $\text{C}_8\text{-BTBT-C}_8$, **(b)** $\text{C}_8\text{-BTBT-C}_8\text{:PS}_{10\text{K}}$, **(c)** $\text{C}_8\text{-BTBT-C}_8\text{:PS}_{100\text{K}}$, and **(d)** $\text{C}_8\text{-BTBT-C}_8\text{:PS}_{280\text{K}}$ thin films were investigated using various imaging techniques. These thin films polarized optical microscope images are depicted in **Fig. 3.4**.

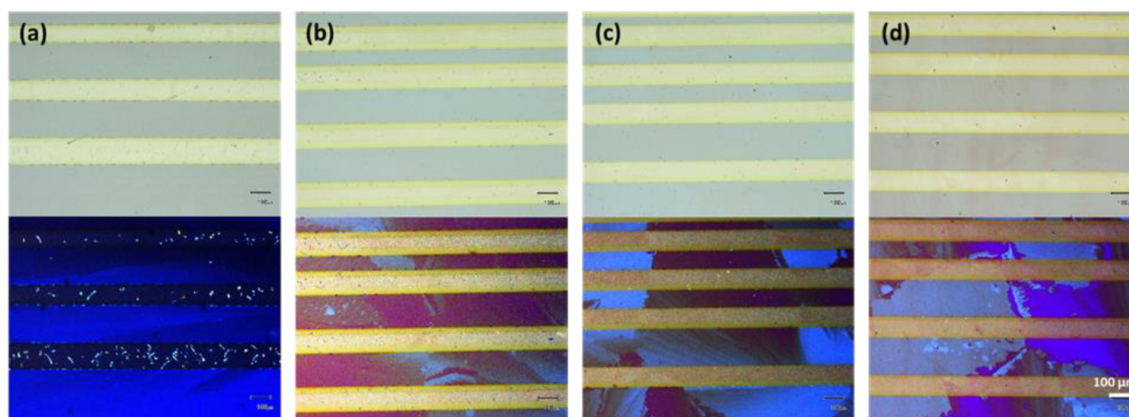


Figure 3.4 Optical microscopy (top) and polarized optical microscopy (bottom) images: **(a)** pristine $\text{C}_8\text{-BTBT-C}_8$, **(b)** $\text{C}_8\text{-BTBT-C}_8\text{:PS}_{10\text{K}}$, **(c)** $\text{C}_8\text{-BTBT-C}_8\text{:PS}_{100\text{K}}$, and **(d)** $\text{C}_8\text{-BTBT-C}_8\text{:PS}_{280\text{K}}$ [82].

The images reveal that all blended formulations have a similar morphology, characterized by plate-like crystal domains. These domains span several hundreds of microns, indicating a significant degree of uniformity and consistency in crystalline structure across all types of blended films.

To gain further data into the surface morphology of these thin films, Atomic Force Microscopy (AFM) was employed, with the results presented in **Fig. 3.5**. The AFM topography images reveal that C_8 -BTBT- C_8 :PS films exhibit a remarkably uniform and smooth surface. This is quantified by the Root Mean Square (RMS) roughness values, which were found to be in the range of 1–6 nm (**Table 3.1**). These RMS values are indicative of the high-quality surface achieved in these films, which is a critical factor for their potential application in electronic devices.

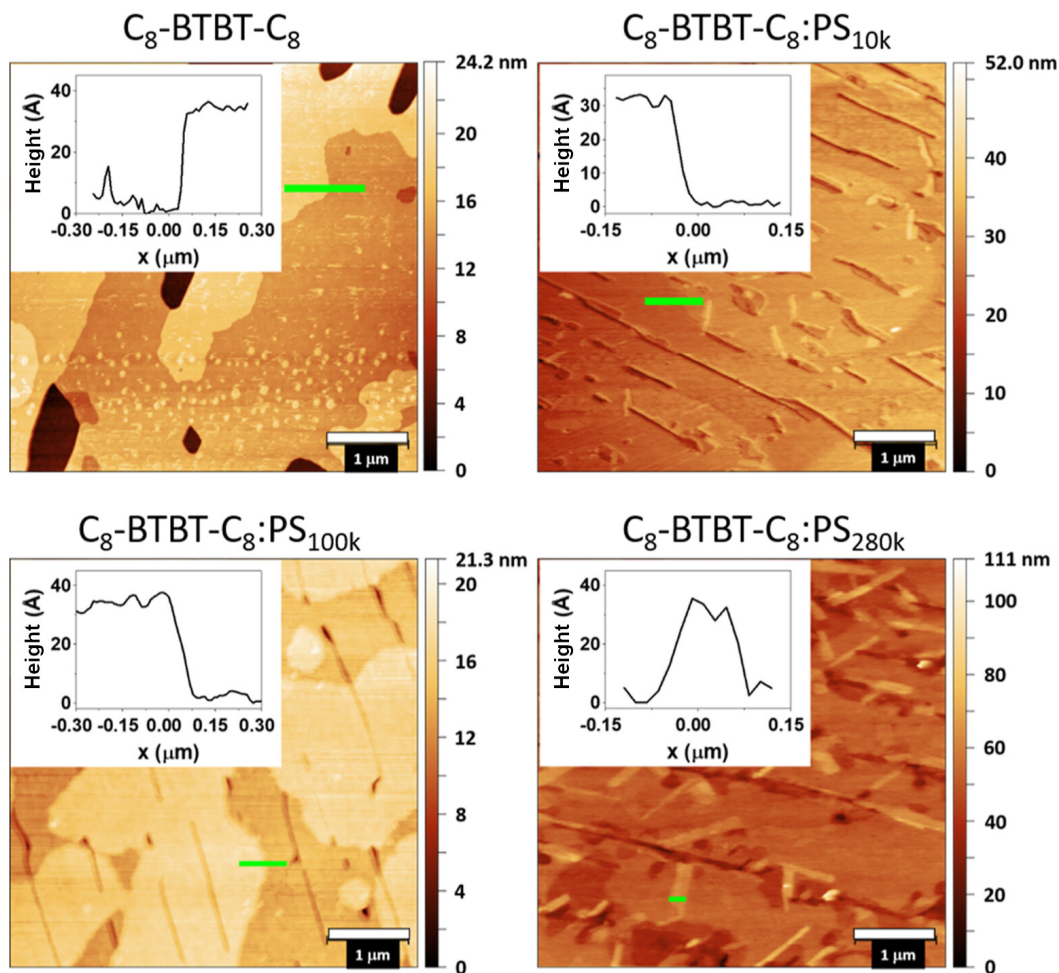


Figure 3.5 Topographic AFM images of the pristine and blended films. Inset: height profiles of the terraces performed along the green lines in the images [82].

In addition to the smoothness, terraces with step heights of approximately 3 nm were observed consistently across all films. This terrace height aligns closely with the length of the

C_8 -BTBT- C_8 molecule, implying that the OSCs crystalline layer is predominantly situated at the top part of the film. It also suggests that the molecules are oriented with their long axis perpendicular to the substrate, confirming the literature result [114].

The film thickness was another critical parameter measured during our study. The pristine films displayed an estimated thickness of around 20 nm, whereas the blended films showed a slightly increased thickness of about 30 nm (**Table 3.1**). This thickness increase of blended films can be attributed to the incorporation of additional material, altering the overall film structure.

	Step	RMS	Thickness
Pristine	3.27 ± 0.36	3.42 ± 0.89	20.3 ± 1.3
PS_{10K}	3.04 ± 0.30	2.79 ± 0.68	32.4 ± 4.3
PS_{100K}	3.22 ± 0.24	1.25 ± 0.26	29.6 ± 8.7
PS_{280K}	3.32 ± 0.46	6.37 ± 1.54	29.3 ± 2.9

Table 3.1 AFM analysis results for Pristine and PS blend films.

Despite the difference in molecular weight of the polystyrene used, the resulting films demonstrate consistent morphological characteristics. This suggests that the processing conditions and the intrinsic properties of C_8 -BTBT- C_8 :PS blends are robust and are not significantly influenced by the variations in the molecular weight of the polymer component. The uniformity and smoothness of these films are particularly advantageous for applications in organic electronics, where surface morphology can significantly influence the device's performance.

The high degree of crystallinity was confirmed by the X-Ray Diffraction (XRD) in **Fig. 3.6**. All thin films exhibited identical diffraction patterns in agreement with the monoclinic phase previously reported for this material [112], which presents a herringbone packing. In addition, only (001) type reflections were observed, indicating that crystallites are highly oriented along the ab plane and that the PS is not affecting the thin film crystal structure.

In summary, the detailed morphological analysis of C_8 -BTBT- C_8 :PS thin films, encompassing both optical microscopy and AFM studies, provides a comprehensive understanding of the structural characteristics. These results offer valuable insights into the material properties, crucial for optimizing the fabrication processes and enhancing the performance of electronic devices based on these materials.

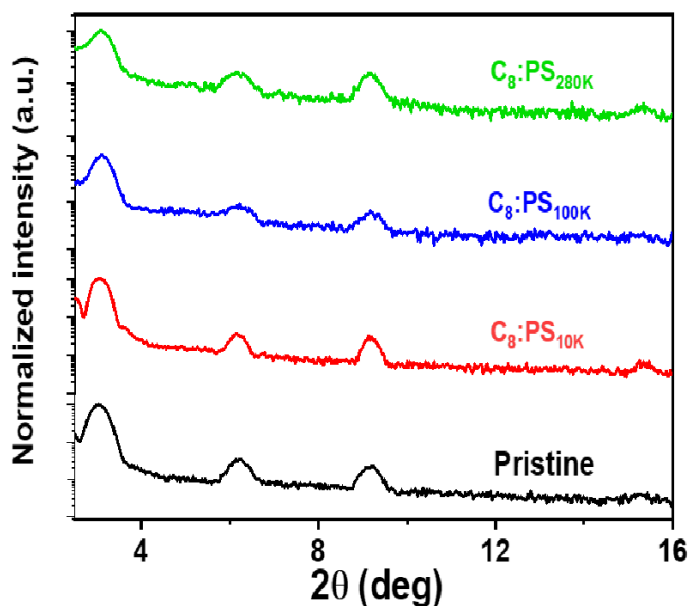


Figure 3.6 XRD of the films: pristine C₈-BTBT-C₈ (black curve), C₈-BTBT-C₈:PS_{10K} (red curve), C₈-BTBT-C₈:PS_{100K} (blue curve), and C₈-BTBT-C₈:PS_{280K} (green curve) [82].

Experimental Methods

The optical microscopy images were taken using an Olympus BX51 equipped with a polarizer and analyzer. Surface topographies of the thin films were examined by a 5500LS Scanning Probe Microscopy system from Agilent Technologies and subsequent data analysis was performed by using Gwyddion 2.56 software. X-ray characterization by X-ray specular diffractograms in the 2θ range 2.5–13° were collected on a Siemens D-5000 diffractometer.

3.4 Electrical Characterization

In our investigation into the electrical behavior of Organic Field-Effect Transistors, we explored the properties of devices with and without contact doping. **Fig. 3.7** presents the output and transfer characteristics of a representative blend film, highlighting the stark differences brought upon by the doping process.

In **Fig. 3.8**, the histogram representation summarizes the performance of four different device configurations, each of one with and without the contact doping layer of F4TCNQ. The devices under study are variations of the C₈-BTBT-C₈ organic semiconductor, with and without PS at different molecular weights. Particularly **Fig. 3.8a** focuses on the saturation mobility of these devices, while **Fig. 3.8b** focuses on the threshold voltages. Additionally, the devices with three different lengths are compared in this figure. This comparison is

particularly important because shows that the channel length can significantly affect the performance characteristics of OFETs, particularly in relation to charge carrier mobility and to the influence of contact resistance.

The output characteristics of the undoped OFETs delineate a non-ideal S-curve pattern at lower source-drain voltage (V_D), as shown in **Fig. 3.7b** and **Fig. 3.9**. This S-curve shape, often observed in devices with high Contact Resistance (R_C), indicates an inherent inefficiency in charge carrier injection at the contacts [115]. Indeed, the S-curve suggests that at lower voltages, the injection of charge carriers is not sufficient to overcome the contact resistance. Only when a certain threshold voltage is reached, does the injection become efficient enough, leading to a rapid increase in current, which contributes to the S-shaped curve in the IV plot [115].

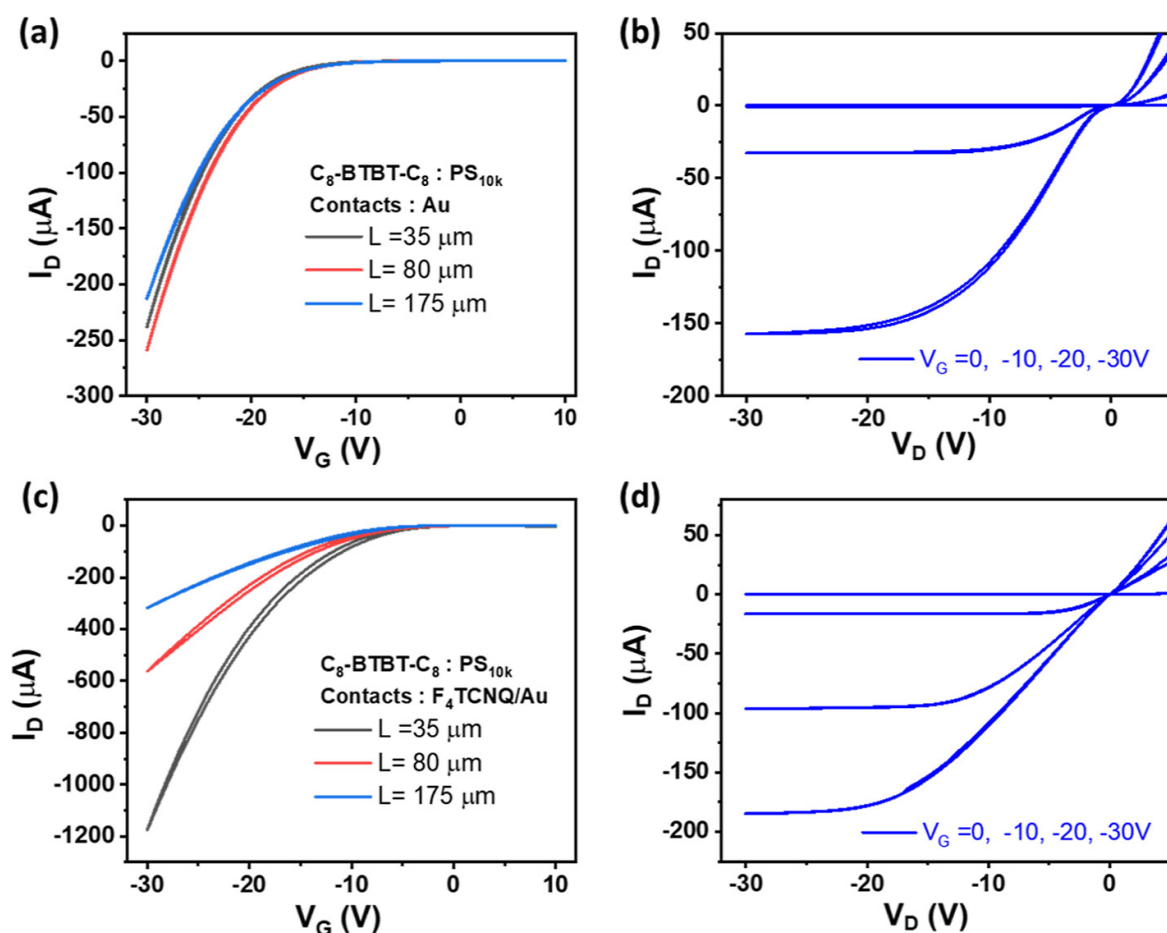


Figure 3.7 Saturation transfer curves of OFETs devices based on $\text{C}_8\text{-BTBT-C}_8\text{:PS}_{10\text{K}}$ with different channel lengths and measured at $V_D = -30\text{ V}$ (a,c) and output curves of the corresponding device with $L = 175 \mu\text{m}$ (b,d). OFETs without (a,b) and with a F_4TCNQ contact doping layer (c,d) [82].

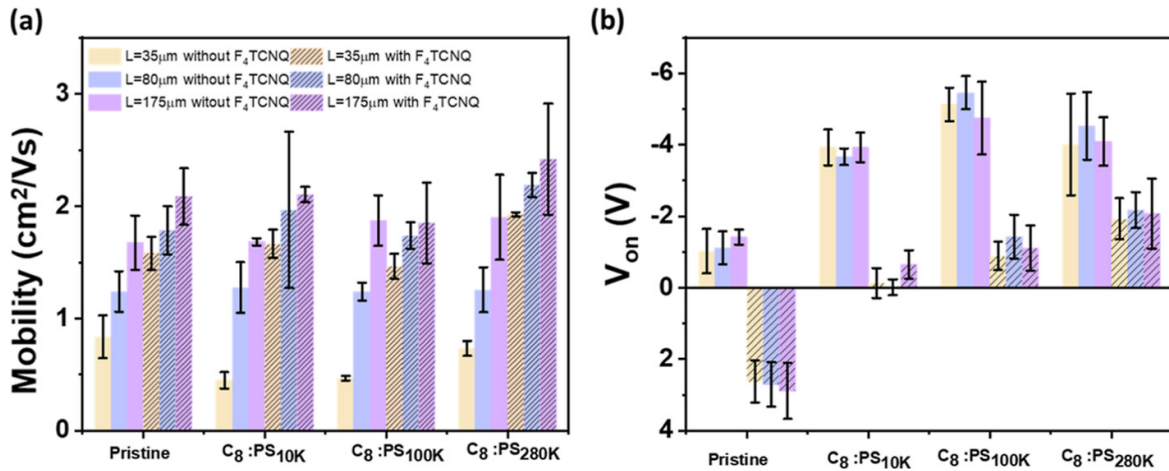


Figure 3.8 (a) Saturation mobility and (b) V_{on} histograms for the four studied devices with and without the contact doping F4TCNQ layer: pristine C_8 -BTBT- C_8 , C_8 -BTBT- C_8 :PS_{10K}, C_8 -BTBT- C_8 :PS_{100K}, and C_8 -BTBT- C_8 :PS_{280K}. Devices with three different lengths are compared. In these plots, C8 stands for C_8 -BTBT- C_8 [82].

Moreover, the transfer plots reveal a pronounced negative switch-on voltage, falling within the range of -4 to -6 V for blended films and approximately -1 to -2 V for the pristine film, as depicted in **Fig. 3.7a** and **Fig. 3.8b**. Such high switch-on voltages are symptomatic of substantial energy barriers that impede charge carrier mobility.

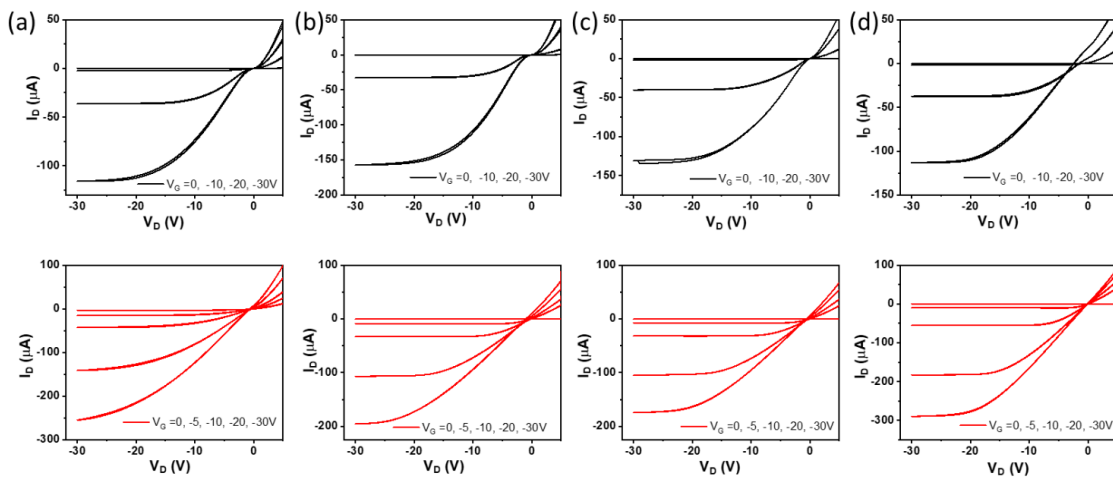


Figure 3.9 Output curves of undoped (top) and contact doped (bottom) devices: (a) pristine C_8 -BTBT- C_8 , (b) C_8 -BTBT- C_8 :PS_{10K}, (c) C_8 -BTBT- C_8 :PS_{100K}, and (d) C_8 -BTBT- C_8 :PS_{280K} [82].

In stark contrast, devices with contact doping exhibited linear I_D/V_D output curves and appreciably lower switch-on voltages. Notably, in the blended films, this voltage is shifted to fall between 0 and -2 V, while in pristine films, it becomes positive, around 3 V, as shown in

Fig. 3.7c,d and **Fig. 3.8b**. The dopant's impact is thus evident, substantially reducing the energy injection barrier and facilitating enhanced charge transport.

The impact of F4TCNQ contact doping on the electrical characteristics of OFETs was deeply examined by modifying the channel lengths (L). The observed behaviors in undoped devices exhibit transfer curves where the source-drain current intensity (I_D) is visibly not inversely scaling with L (see **Fig. 3.7a** and **Fig. 3.10**).

In accordance, the device mobility of these devices exhibits a considerably strong dependence on L , as shown in **Fig. 3.8a**. Such a trend is indicative of the overarching influence of the contact injection barriers, which become increasingly significant in devices with shorter L , where Contact Resistance values are more comparable to the channel resistance.

Conversely, upon doping with F4TCNQ, the transfer plots align more closely with the variations in L , as depicted in **Fig. 3.7c** and **Fig. 3.11**. The corresponding mobility values not only increase but also demonstrate less sensitivity to L , inferring a mitigation of contact-related limitations.

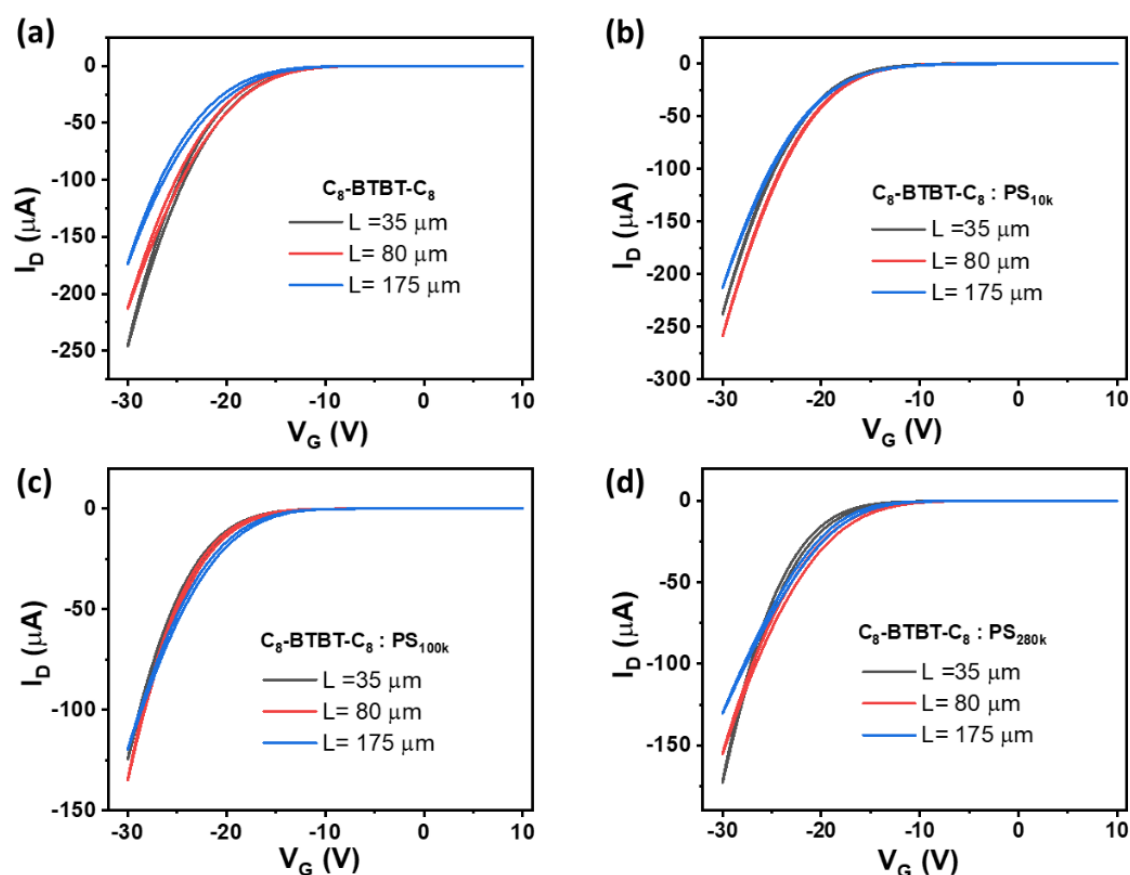


Figure 3.10 Saturation transfer curves of undoped devices with different channel lengths measured at $V_D = -30V$: (**a**) pristine C_8 -BTBT- C_8 , (**b**) C_8 -BTBT- C_8 : PS_{10k} , (**c**) C_8 -BTBT- C_8 : PS_{100k} , and (**d**) C_8 -BTBT- C_8 : PS_{280k} [82].

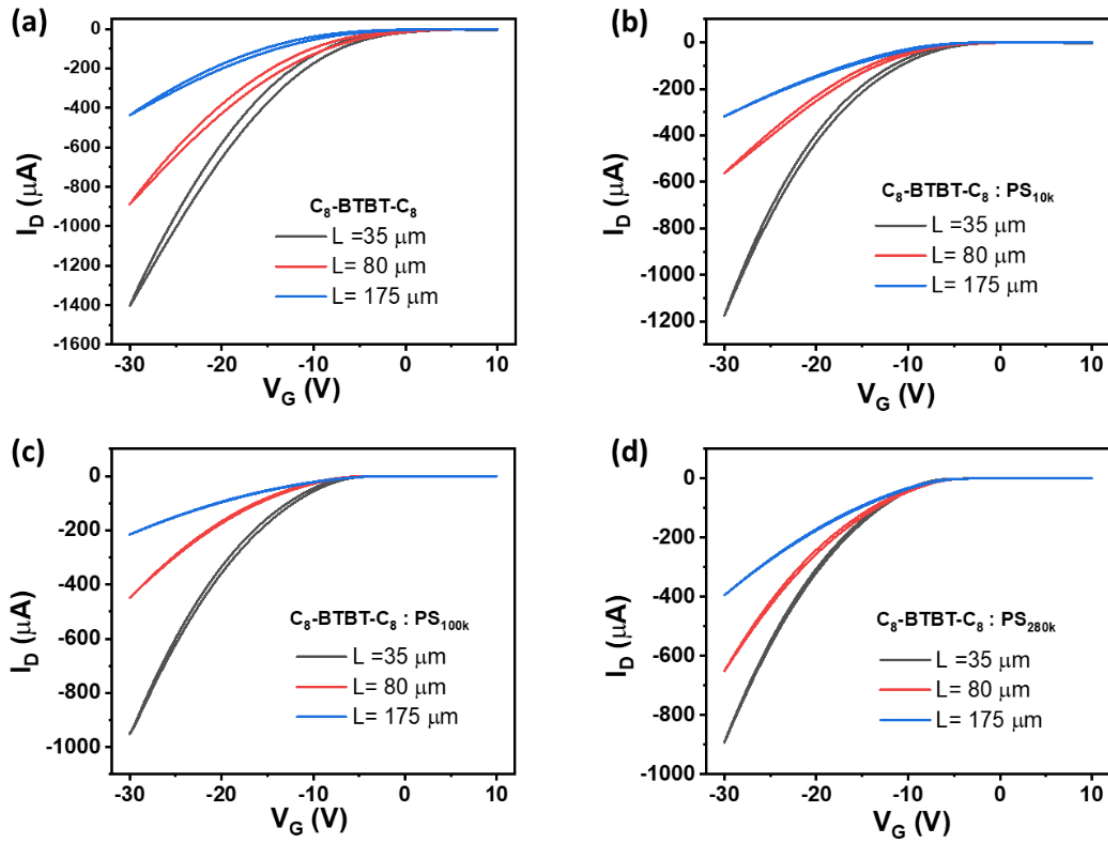


Figure 3.11 Saturation transfer curves of contact doped devices with different lengths measured at $V_D = -30\text{V}$: (a) pristine $\text{C}_8\text{-BTBT-C}_8$, (b) $\text{C}_8\text{-BTBT-C}_8\text{:PS}_{10\text{K}}$, (c) $\text{C}_8\text{-BTBT-C}_8\text{:PS}_{100\text{K}}$, and (d) $\text{C}_8\text{-BTBT-C}_8\text{:PS}_{280\text{K}}$ [82].

Remarkably, the incorporation of PS of different molecular weights into the OFETs structure does not notably impact the mobility or the doping efficiency. This observation suggests that the intrinsic properties of PS do not directly influence the operational mechanics of the device or the doping efficiency.

Time Stability

Despite the marked advancements in device performance through contact doping, the persisting challenge lies in the stability of the OFETs over time. The temporal evolution of the saturation transfer characteristics, observed over 3 weeks and plotted on a semi-logarithmic scale, clarifies this issue (refer to **Fig. 3.12**). Devices based on pristine $\text{C}_8\text{-BTBT-C}_8$ demonstrated significant shifts in both the off-current (I_{off}) and the switch-on voltage (V_{on}), indicative of dopant migration towards the channel.

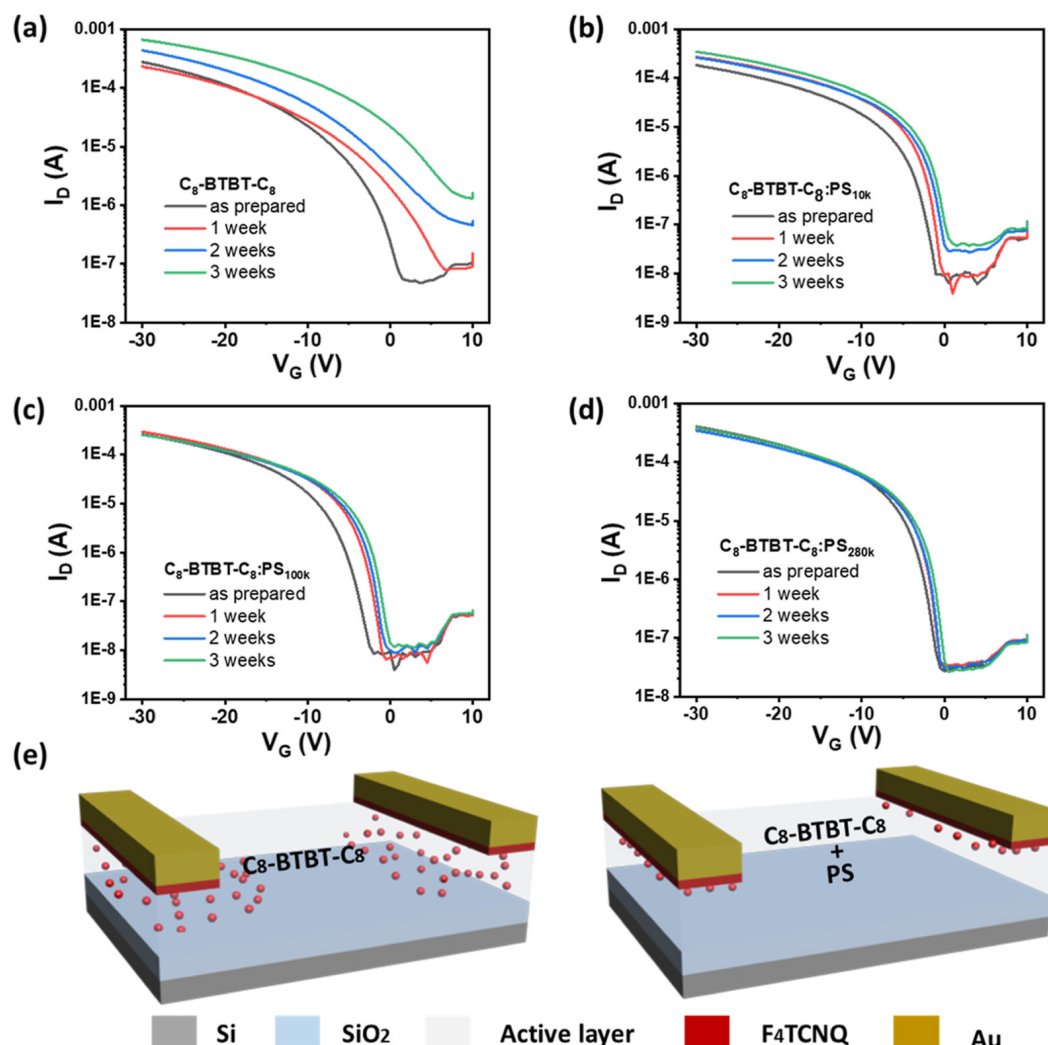


Figure 3.12 Time evolution of the saturation transfer curves of devices with different lengths measured at $V_D = -30$ V: (a) pristine C_8 -BTBT- C_8 , (b) C_8 -BTBT- C_8 :PS_{10K}, (c) C_8 -BTBT- C_8 :PS_{100K}, and (d) C_8 -BTBT- C_8 :PS_{280K}. (e) Scheme of F4TCNQ molecule diffusion toward the channel: in the pristine-based device significant dopant diffusion is taking place, while the dopant diffusion is much less pronounced in the blended films [82].

On the other hand, blended films with PS_{10K} showcased a marked improvement in stability. However, it is within High-Molecular-Weight Polystyrene blends, such as PS_{100K} and PS_{280K}, that we observed a strikingly stable performance, with negligible variations in V_{on} and I_{off} over time.

These results are confirmed by the saturation regime data obtained through standard fitting procedures, compiled in **Fig. 3.13** and **Fig. 3.14**. The data collectively suggest that the presence of PS, particularly HMWPS, serves as an effective barrier, inhibiting the migration of dopant molecules from the contact regions into the channel, as conceptually illustrated in **Fig. 3.12e**.

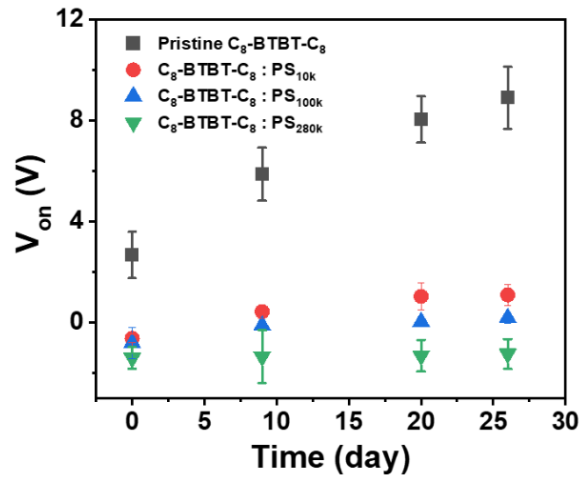


Figure 3.13 V_{on} evolution with time of F4TCNQ contact doped devices: pristine C_8 -BTBT- C_8 (black), C_8 -BTBT- C_8 : PS_{10K} (red), C_8 -BTBT- C_8 : PS_{100K} (blue) and C_8 -BTBT- C_8 : PS_{280K} (green) [82].

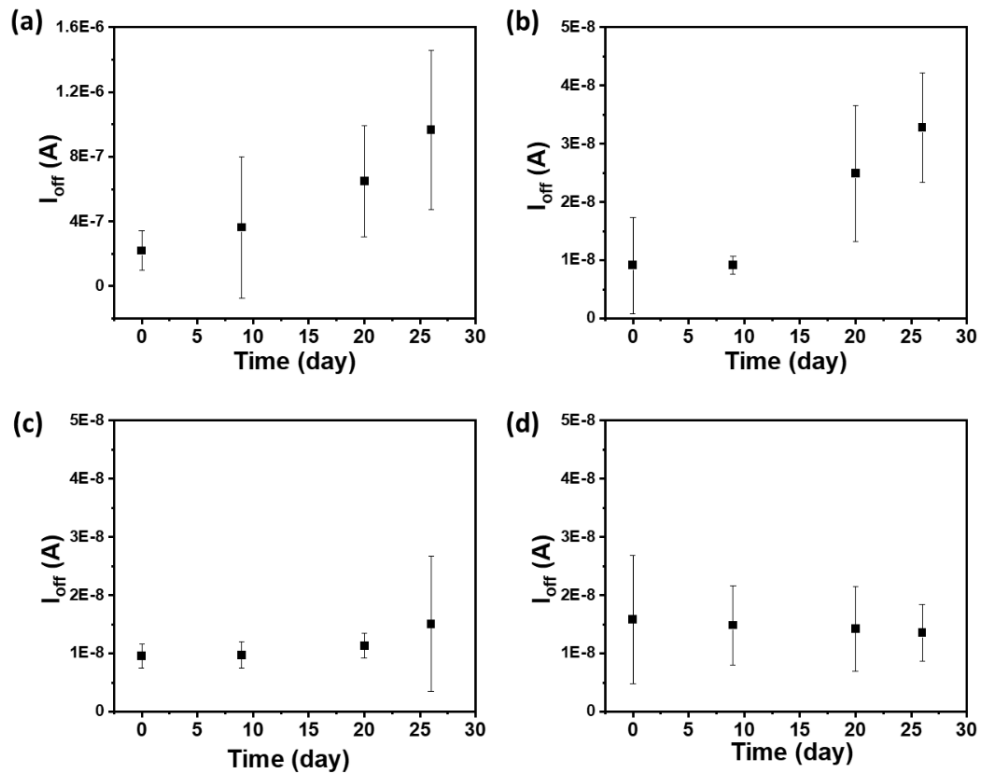


Figure 3.14 I_{off} evolution with time of F4TCNQ contact doped devices: (a) pristine C_8 -BTBT- C_8 , (b) C_8 -BTBT- C_8 : PS_{10K} , (c) C_8 -BTBT- C_8 : PS_{100K} , and (d) C_8 -BTBT- C_8 : PS_{280K} . Data was collected from different 12 devices in each case [82].

In summary, our study underlines the essential role of molecular weight of PS blends in determining the OFETs stability post-contact doping.

Experimental Methods

Electrical measurements were performed in ambient conditions employing a two-channel Keithley 2612 SourceMeter. Transfer characteristics were measured in the saturation regime, swept forward, and reverse. The mobility and V_{th} values were extracted from the saturation regime according to the mentioned equation **Eq. (1.14)**. For each ink formulation, the device parameters were measured from at least 30 devices from two substrates to ensure thin film homogeneity and reproducibility.

3.5 Chemical Characterization

TOF-SIMS experiments were conducted to elucidate the dopant, OSCs, and polymer distribution within our organic electronic structures. This spectroscopy technique has been largely employed for the aptitude to explain the complexity of diffusion and segregation in multilayered systems [95, 116]. The surface chemical maps obtained from TOF-SIMS both immediately post-fabrication and after three weeks offer visual evidence of the dopant's behavior (**Fig. 3.15**). Utilizing the molecular fragment ion of $C_{12}F_4N_4^-$ at $m/z = 276.00$ to trace the F4TCNQ dopant presence, a discernible inhomogeneity in the distribution across the channel area is evident. In freshly prepared C_8 -BTBT- C_8 samples, the dopant exhibited a pattern of linear, micrometric pathways, potentially guided by the underlying grainy, polycrystalline surface morphology of the active layer (**Fig. 3.15a**). In three weeks, a profound modification occurred, showing the channel area entirely covered by the dopant (**Fig. 3.15e**). Such a progression underscores an unrestrained diffusion, inevitably impinging upon the operational efficacy of the device.

The introduction of PS as a binding polymer to the C_8 -BTBT- C_8 semiconductor matrix determines a morphological evolution of the surface, which, in turn, influences the diffusion behavior of F4TCNQ. This effect is intensely captured in the chemical mappings illustrated in **Fig. 3.15b-d**, where the $C_{12}F_4N_4^-$ molecular fragment ion delineates the dopant distribution for freshly prepared C_8 -BTBT- C_8 PS_{10K}, C_8 -BTBT- C_8 PS_{100K}, and C_8 -BTBT- C_8 PS_{280K} samples. The dopant's localization along the gold contacts suggests a diffusion gradient that significantly reduces moving towards the central channel, an exponential attenuation reminiscent of Fick's law diffusion.

Going deeper into the influence of the polymer's molecular weight on dopant distribution, we observe that the increment from 10 kDa (LMWPS) to 100 and 280 kDa (HMWPS) induces pronounced confinement of the diffusion process in the surrounding area of the gold electrodes. The freshly cast C_8 -BTBT- C_8 PS_{10K} film showcases a vibrant dopant signal adjacent to the gold contacts, which tapers off exponentially across a span of approximately

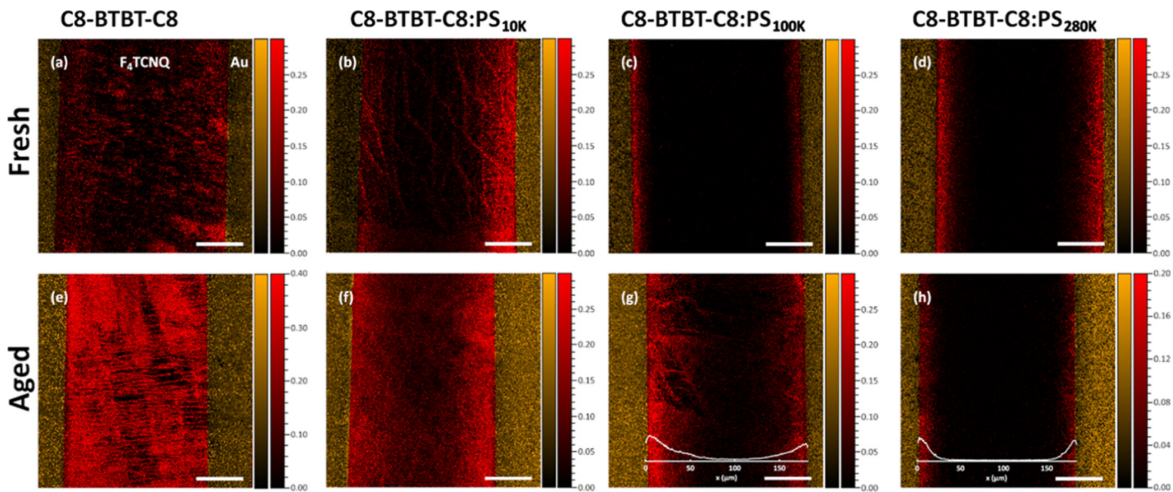


Figure 3.15 TOF-SIMS surface chemical maps of fresh and 3 weeks aged samples: (a) fresh pristine C_8 -BTBT- C_8 , (b) fresh C_8 -BTBT- C_8 : C_8 -BTBT- C_8 PS_{10K}, (c) fresh C_8 -BTBT- C_8 : C_8 -BTBT- C_8 PS_{100K}, (d) fresh C_8 -BTBT- C_8 : C_8 -BTBT- C_8 PS_{280K}, (e) aged pristine C_8 -BTBT- C_8 , (f) aged C_8 -BTBT- C_8 : C_8 -BTBT- C_8 PS_{10K}, (g) aged C_8 -BTBT- C_8 : C_8 -BTBT- C_8 PS_{100K}, and (h) aged C_8 -BTBT- C_8 : C_8 -BTBT- C_8 PS_{280K}. Scale bar: 40 μm . Color scale bars from black to red and from black to bright yellow indicate the amplitude in number of ion counts for $C_{12}F_4N_4^-$ and Au^- , respectively. Color scale bar from black to red for $C_{12}F_4N_4^-$ was normalized for total counts to account for variations in the experimental conditions. Intensity line profile along the solid line (x-axis also represents the line scan) in $C_{12}F_4N_4^-$ maps for aged C_8 -BTBT- C_8 : C_8 -BTBT- C_8 PS_{100K} (inset in figure 6g) and aged C_8 -BTBT- C_8 : C_8 -BTBT- C_8 PS_{280K} (inset in figure 6h) [82].

70 μm towards the channel's heart. In stark contrast, the C_8 -BTBT- C_8 PS_{100K} film reveals a precipitous diminution of dopant signal mere 10–20 μm from the contacts, capturing the dopant within a markedly narrow region.

The progression of time enhance this spatial distribution; after three weeks, the C_8 -BTBT- C_8 PS_{100K} (**Fig. 3.15g**) and C_8 -BTBT- C_8 PS_{280K} (**Fig. 3.15h**) samples steadfastly preserve the dopant within the initial 10–20 μm boundary, as supported by the intensity profiles embedded within **Fig. 3.15g,h**. This persistence of the polymer's impediment to dopant migration contrasts with the behavior observed in the LMWPS-blended film (**Fig. 3.15f**), where the polymer's retentive effect is clearly reduced.

Essentially, our results reveal a substantial delay of F4TCNQ diffusion in the presence of higher molecular weight PS, highlighting the polymer's role as an inhibitor of dopant diffusion and, consequently, the electrochemical stability of the OFETs.

The characterization of the surface distribution of PS was accurately conducted by mapping the signal intensity of the $C_7H_7^+$ ion ($m/z = 91.07$). Through the analytical power of TOF-SIMS, we observed in **Fig. 3.16** that the $C_{23}H_{25}S_2^+$ ($m/z = 365.21$) molecular fragment ion, indicative of the OSCs C_8 -BTBT- C_8 , is prevalent across the samples. Remarkably, total ion imaging disclosed that films incorporating HMWPS are more resilient against craze-

induced fractures. The $C_7H_7^+$ signal, very low in intensity in the channel area, primarily collocates with these fractures, corroborating literature assertions of reduced crazing stress in HMWPS films [117]. No substantial influence of the polymer on the surface distribution of the OSCs was detected, underscored by the consistent $C_{23}H_{25}S_2^+$ chemical maps. These observations provide a foundation for the subsequent in-depth profiling experiments, aimed at elucidating the vertical distribution of F4TCNQ, C_8 -BTBT- C_8 , and PS within the channel.

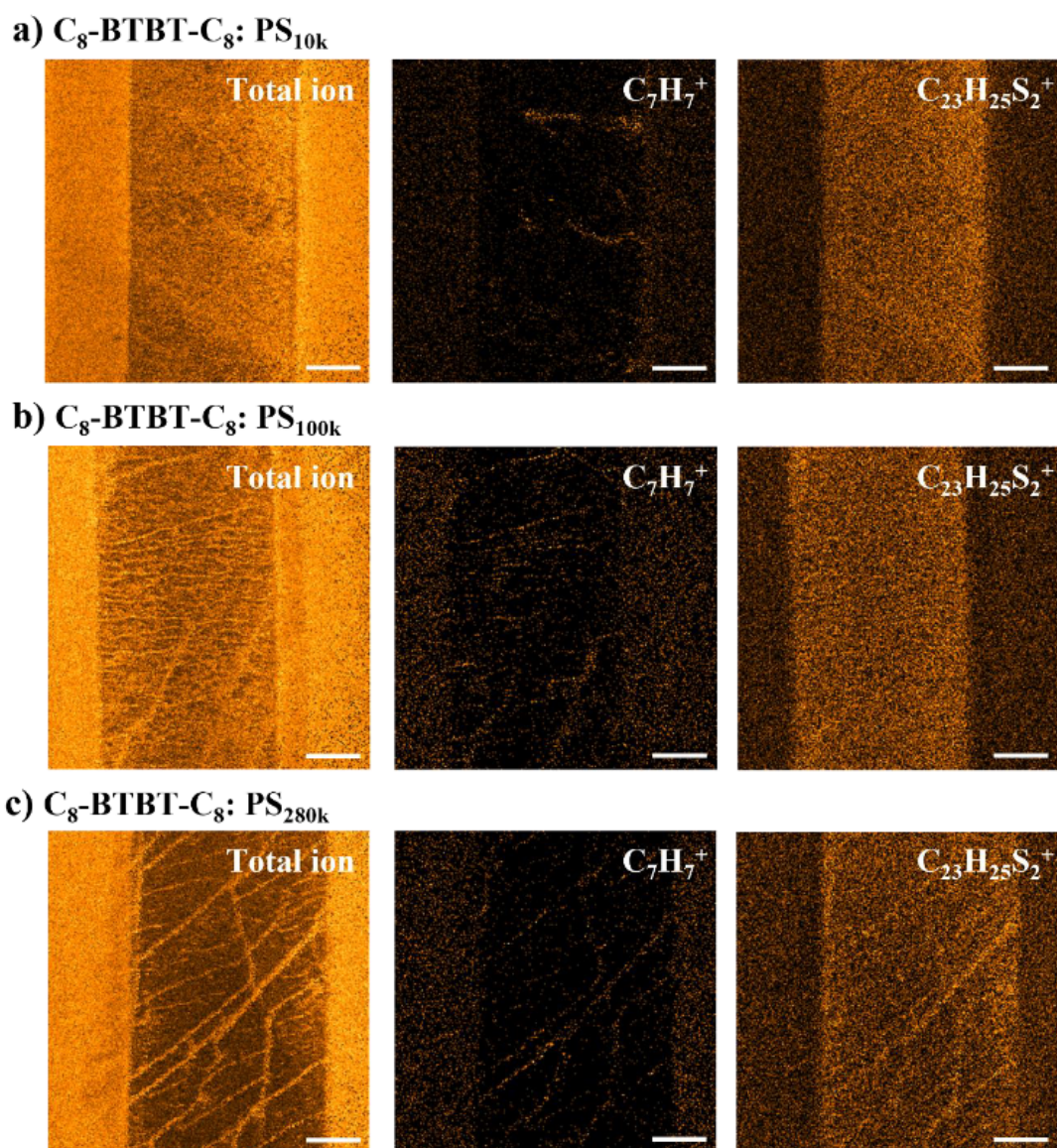


Figure 3.16 TOF-SIMS surface chemical maps in positive polarity. The total ion $C_7H_7^+$, and $C_{23}H_{25}S_2^+$ signals are reported: **(a)** C_8 -BTBT- C_8 :PS_{10k}, **(b)** C_8 -BTBT- C_8 :PS_{100k}, and **(c)** C_8 -BTBT- C_8 :PS_{280k}. Scale bar 25 μm [82].

Moving beyond surface analysis, we performed the study of the chemical vertical distribution. Depth profiling experiments, conducted $10\ \mu\text{m}$ from the gold electrode, provided a detailed cross-section of the material layers. The resulting depth profiles, depicted in **Fig. 3.17**, span pristine $\text{C}_8\text{-BTBT-C}_8$ (**Fig. 3.17a**), and blend samples with $\text{PS}_{10\text{K}}$ (**Fig. 3.17b**), $\text{PS}_{100\text{K}}$ (**Fig. 3.17c**), and $\text{PS}_{280\text{K}}$ (**Fig. 3.17d**).

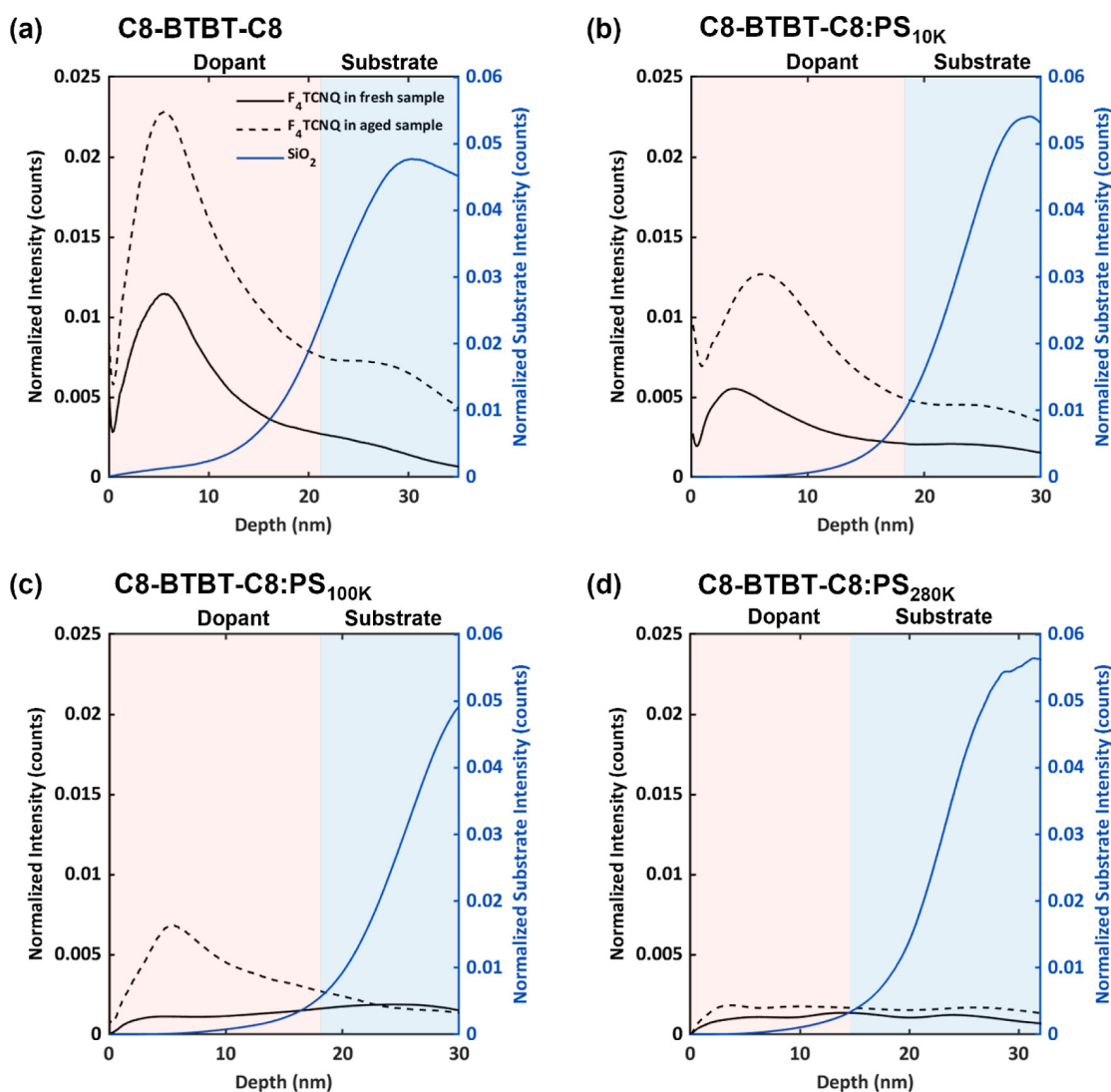


Figure 3.17 TOF-SIMS depth profiles of: (a) pristine $\text{C}_8\text{-BTBT-C}_8$, (b) $\text{C}_8\text{-BTBT-C}_8\text{:PS}_{10\text{K}}$, (c) $\text{C}_8\text{-BTBT-C}_8\text{:PS}_{100\text{K}}$, and (d) $\text{C}_8\text{-BTBT-C}_8\text{:PS}_{280\text{K}}$. The depth profiling experiments were performed in the channel between the two gold electrodes, $10\ \mu\text{m}$ away from the gold electrode, approximately. CN^- at $m/z\ 26.00$ (F_4TCNQ) and SiO_2^- at $m/z\ 59.97$ (substrate) profiles were normalized to total counts. Normalized secondary ion intensities of CN^- and SiO_2^- are plotted vs depth. The ion signal intensity of the F_4TCNQ dopant is reported for the fresh sample (dashed black line) and the 3-week aged sample (solid black line). The normalized ion signal intensity of the F_4TCNQ dopant (black lines) and substrate (blue line) are reported on the left and right y-axis, respectively [82].

The CN^- ($m/z = 26.00$) ion was selected as a representative signal for F4TCNQ in fresh (black solid lines) and aged sample (black dashed lines), while the SiO_2^- ($m/z = 59.97$) for the substrate (blue curves). The depth profile of CN^- shows that in the pristine $\text{C}_8\text{-BTBT-C}_8$ the dopant is highly present on the surface, sub-surface (2–10 nm), and the bulk (10–20 nm) of the OSCs layer (**Fig. 3.17a**).

This distribution was consistent even in aged samples, with a noticeable increase in dopant concentration over time. In contrast, samples blended with $\text{PS}_{10\text{K}}$ exhibited a halved intensity of the F4TCNQ signal, both before and after aging, when compared to the pristine samples.

However, a marked difference was observed in $\text{C}_8\text{-BTBT-C}_8$ samples blended with $\text{PS}_{100\text{K}}$ and $\text{PS}_{280\text{K}}$. Here, the dopant signal intensity significantly dropped and showed a more uniform distribution throughout the active layer. This uniformity can be attributed to the effective confinement of the dopant by the presence of HMWPS, leading to a general reduction in diffusion phenomena.

TOF-SIMS depth profiles of OSCs and PS in (a) $\text{C}_8\text{-BTBT-C}_8$, (b) $\text{C}_8\text{-BTBT-C}_8\text{:PS}_{10\text{K}}$, (c) $\text{C}_8\text{-BTBT-C}_8\text{:PS}_{100\text{K}}$, and (d) $\text{C}_8\text{-BTBT-C}_8\text{:PS}_{280\text{K}}$ are shown in **Fig. 3.18** to evaluate the presence of the vertical phase segregation, phenomenon that will be discussed in **Chapter 4** of this work.

The MCs_n^+ adducts were employed to attenuate matrix effects. SCs_3^+ at m/z 430.65, and $\text{SiO}_2\text{Cs}_3^+$ at m/z 458 were selected to represent $\text{C}_8\text{-BTBT-C}_8$ and substrate, respectively. For the PS polymer, several characteristic ion signals were aggregated to amplify signal intensity: C_2Cs_3^+ (m/z 422.68), C_2HCs_3^+ (m/z 423.68), C_3Cs_3^+ (m/z 434.68), C_3HCs_3^+ (m/z 435.68), C_4Cs_3^+ (m/z 446.68), C_4HCs_3^+ (m/z 447.68), C_6Cs_3^+ (m/z 470.68), and $\text{C}_7\text{H}_8\text{Cs}_3^+$ (m/z 490.68). The vertical distribution of OSCs and PS remained consistent in both fresh and aged samples. Furthermore, while the upper part of the active layer is mostly constituted by the OSCs, the lower part is characterized by the segregation of the polymer, which is in agreement with the AFM data. In conclusion, we observed two effects due to the presence of the polymer in the blend formulation:

- When the OSCs is blended with PS, a general decrease of the diffusion phenomena of the dopant is revealed. This is more evident when HMWPS is used in the blend formulation.
- In the OSCs/PS blend films, the upper part of the active layer is mostly constituted by the OSCs, while the lower part is characterized by the segregation of PS. Consequently, the in-depth dopant diffusion can be efficiently limited in the lower part of the active layer by the higher presence of the polymer. However, this effect can be observed even in the upper part where the PS is less present.

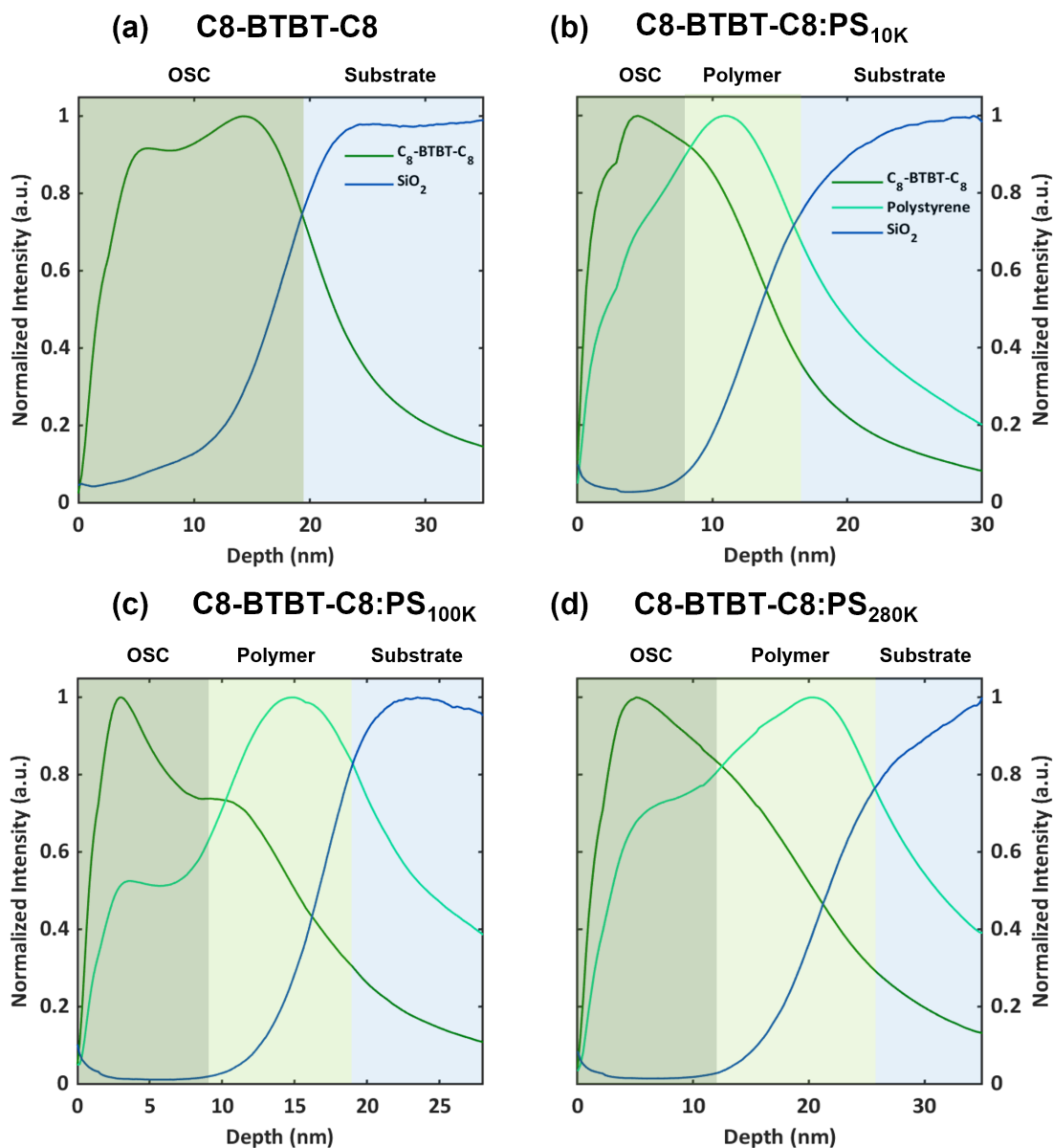


Figure 3.18 TOF-SIMS depth profiles of: (a) pristine C₈-BTBT-C₈, (b) C₈-BTBT-C₈:PS_{10K}, (c) C₈-BTBT-C₈:PS_{100K}, and (d) C₈-BTBT-C₈:PS_{280K}. To mitigate matrix effects and prevent detector saturation, MC_n⁺ adducts were employed. The ion signals SC₃⁺ at m/z 430.65, and SiO₂CS₃⁺ at m/z 458.77 were chosen to represent C₈-BTBT-C₈ and the substrate, respectively. For the PS polymer, several characteristic ion signals were aggregated to amplify signal intensity: C₂CS₃⁺ (m/z 422.68), C₂HCS₃⁺ (m/z 423.68), C₃CS₃⁺ (m/z 434.68), C₃HCS₃⁺ (m/z 435.68), C₄CS₃⁺ (m/z 446.68), C₄HCS₃⁺ (m/z 447.68), C₆CS₃⁺ (m/z 470.68), and C₇H₈CS₃⁺ (m/z 490.68). The MC_n⁺ profiles were normalized to their maximum values and plotted against depth to elucidate the distribution characteristics of the materials within the channel [82].

Experimental Methods

TOF-SIMS measurements were performed using a TOF.SIMS5 (ION-TOF GmbH, Münster, Germany) secondary ion mass spectrometer. A low-energy electron flood gun (20 V) was used for charge compensation. Surface analysis data were acquired in high lateral resolution mode using Bi_3^{++} (30 keV) with a pulse width of 18.4 ns and a current emission of 0.4 pA. The lateral resolution of the surface chemical maps was estimated to be $\simeq 150$ nm. The analyzed area is equal to $250 \times 250 \mu\text{m}^2$. Depth profiling measurements were performed in dual-beam mode using Bi_3^{++} as the primary ion gun and low energy Cs^+ (250 eV, current: 1.6 nA) gun as sputtering beam. The area of analysis ($50 \times 50 \mu\text{m}^2$) was selected in the middle of the sputtering region according to a ratio of 1/3 with the sputtering area of $200 \times 200 \mu\text{m}^2$. The chemical maps were collected at a resolution of 256×256 pixels. Secondary ions were extracted at 2 kV and detected with a ToF mass analyzer with a cycle time of 100 μs [(1 \div 800) m/z mass range]. Mass spectra, with a mass resolution higher than 5000 m/ Δ m for all masses, were calibrated using CN^- , S^- , and $\text{C}_{12}\text{F}_4\text{N}_4^-$. Five measurements were collected in different areas for each. Data were exported for further analysis by SurfaceLab v6.5 software (IONTOF GmbH, Münster, Germany).

3.6 Conclusions: The Impact of Polystyrene in Inhibiting Dopant Diffusion

This study explores Organic Field-Effect Transistors, focusing on the innovative strategy of molecular contact doping to enhance device performance. A significant highlight of this research is the incorporation of a dopant layer between the Organic Semiconductors and the top gold contacts. This strategic position of the dopant layer crucially reduces the energy barriers associated with charge injection and release, thereby markedly boosting the overall efficiency of OFETs.

However, the implementation of molecular contact doping is not free from challenges. A primary concern is the tendency of the dopant to diffuse into the OFETs channel over time, leading to an unintentional doping of the OSCs. This diffusion process poses a significant threat to the device's functionality, particularly affecting on/off switching capabilities. To address this issue, our study explores several devices where Polystyrene is utilized as a diffusion-blocking agent. The introduction of PS in various molecular weights into the OFETs structure has been fundamental to inhibiting the dopant diffusion. This strategy was significantly effective in maintaining the dopant within the intended layers, thereby preserving the device's integrity and performance.

Time-of-Flight Secondary Ion Mass Spectrometry studies provide critical insights into the surface and in-depth distribution of the dopant, further confirming the effectiveness of our approach. We have been able to demonstrate that in thin films of OSCs blends with High-Molecular-Weight Polystyrene PS, the dopant remains drastically confined to the contact areas. This confinement is reflected in the enhanced long-term stability and capability of the devices.

The results of this work represent a significant advancement in the development of OFETs. By successfully mitigating the issue of dopant diffusion, we have opened up new paths for the development of more stable and efficient organic electronic devices. This breakthrough in molecular contact doping, not only enhances the mobility of OFETs, but also sets a precedent for future research and development of organic semiconductors.

In addition, our results suggest that the method of doping and the choice of dopant material are critical parameters that influence the performance and stability of OFETs. The use of PS as a dopant-blocking layer offers a novel way to fine-tune these devices, potentially leading to more precise control of electrical properties. This could pave the way for the development of OFETs with customizable performance characteristics, tailored for specific applications in flexible electronics, display technology, and beyond.

Furthermore, our research opens up possibilities for exploring other polymer materials as potential diffusion-blocking agents. The effectiveness of PS in this role encourages a broader investigation into polymers with varying properties, which could lead to the discovery of even more efficient materials for enhancing OFETs performance. This investigation stream could significantly contribute to organic electronics, providing a deeper understanding and novel solutions to the challenges faced in device fabrication and optimization.

In conclusion, the insights gained from this study not only address a critical challenge in OFETs technology but also provide a foundation for future innovations in organic electronics. The role of PS in inhibiting dopant diffusion is a key discovery that has implications for the design and development of next-generation electronic devices, marking a significant step forward in the evolution of organic semiconductor technology.

4

Evaluation of Blended and Non-Blended Thin Films

The blending of semiconductor and polymer materials has proven to be a good approach for enhancing the performance of Organic Field-Effect Transistors [80]. This technique requires combining an OSCs with a polymer to improve the overall characteristics of the OFETs. The primary goal of this blend is to optimize the interface between the semiconductor and the dielectric layer, which is a crucial factor for an efficient charge transport [118, 119, 120]. This optimization leads to a reduction in the threshold voltage and an increase in the charge carrier mobility, therefore significantly boosting the performance of the devices [80].

However, a lot of challenges arise to achieve an ideal blend, primarily related to the compatibility and to the distribution of the semiconductor and polymer materials. To overcome these challenges, we have adopted an innovative approach in our OFETs fabrication process using advanced OSCs. Our method incorporates a precise blending technique, which was successful in achieving uniform semiconductor-polymer blends, as well as ensuring consistent device performance and enhanced operational stability.

4.1 Introduction and Objectives

Solution-based deposition techniques for small molecule Organic Semiconductors are increasingly attractive, requiring a low cost for manufacturing of Organic Field-Effect Transistors [121]. These methods are particularly compatible with high-throughput processes and flexible substrates, offering a promising opportunity for scalable production. However, challenges such as dewetting, along with limited control over nucleation and growth of molecular crystallites, do not always assure the reproducibility and homogeneity of the crystalline films [122, 123]. Such inconsistencies can lead to significant performance variability among different devices.

To overcome these issues, a novel approach was developed, involving the blending of small semiconducting molecules with amorphous insulating polymers [80, 124]. This strategy

synergizes the high carrier mobility of crystalline OSCs with the enhanced processability provided by the polymer. Notably, this blending technique has determined a substantial improvement in charge carrier mobility, device reproducibility, and stability. The enhanced performance of OSCs blend OFETs is largely attributed to the vertical phase separation of the two material components [124]. This results in a stratified structure, with a polymeric layer underlying the OSCs/dielectric interface, which effectively passivates the interface and ensures a low density of traps. Such stratification has been confirmed by various ex-situ measurements, including transmission electron microscopy, Secondary Ion Mass Spectrometry, neutron reflectivity, and variable angle spectroscopic ellipsometry [125, 126, 127].

The OSCs family of acenes, like 6,13-bis(triisopropylsilylethynyl)pentacene (TIPS) and 1,4,8,11-Tetramethyl-6,13-triethylsilylethynylpentacene (TMTES), has demonstrated exceptional performing devices, becoming one of the most promising small semiconducting molecules due to high hole mobility [122]. Blends utilizing TMTES and Polystyrene (PS) have shown enhanced film reproducibility, homogeneity, and remarkable field-effect mobilities [80, 124].

Despite these advancements, a comprehensive understanding of the detailed vertical structure of these films at the nanometer scale remains not clearly understood. To address this knowledge gap, Time-of-Flight Secondary Ion Mass Spectrometry (TOF-SIMS) techniques have been employed and have been recognized as a powerful tool. TOF-SIMS provides the needed precision to analyze the nanoscale structure of these blended films and therefore contributed significantly to the optimization of solution-based deposition techniques for OFETs [95].

The main aim of this chapter is to conduct an in-depth nanoscale analysis of the vertical distribution of TMTES and PS within blended thin films. This examination is crucial for the comprehension of the variability in the macroscopic electrical performance observed when these materials are utilized as active layers in Organic Field-Effect Transistors devices. Moreover, the chapter focuses on the electrical characterization of thin films, which were prepared using solutions with varying TMTES:PS weight ratios (specifically, 1:0 and 2:1) and deposited via Bar-Assisted Meniscus Shearing (BAMS) method [128, 129, 112].

4.2 Device Fabrication

1,4,8,11-Tetramethyl-6,13-triethylsilylethynylpentacene (TMTES) and Polystyrene (PS) with a molecular weight of 280,000 g/mol were acquired from Ossila and Sigma–Aldrich respectively (chemical formula in **Fig. 4.1a**). Solutions of TMTES and PS were prepared in

anhydrous chlorobenzene at a concentration of 2.0% w/w. For blending, the TMTES and PS solutions were combined in 2:1 volume ratios of TMTES to PS. Before deposition, these solutions were heated to the substrate temperature designated for the coating process.

Interdigitated gold electrodes were fabricated on heavily n-doped Si wafers (Si-Mat) covered with a 200 nm thick SiO₂ layer, using photolithography. The electrodes comprised a 5 nm chromium layer for adhesion, topped with a 40 nm layer of gold, both thermally evaporated onto the Si wafer. The channel lengths (L) of the electrodes varied between 25 and 200 μm, maintaining a constant width-to-length ratio of 100 (W/L). The substrates were subsequently cleaned through sonication in acetone and isopropanol of HPLC grade, followed by drying under a nitrogen flow.

To modify the electrode surfaces, a self-assembled monolayer of 2,3,4,5,6-pentafluorothiophenol (PFBT) was applied. The gold surfaces underwent a 25-minute exposure to ultraviolet ozone cleaning, followed by a 15-minute immersion in a 15×10^{-3} M PFBT solution in isopropanol. The substrates were then washed with pure isopropanol to eliminate excess PFBT and dried under nitrogen.

The deposition of the TMTES solutions onto these substrates was executed using Bar-Assisted Meniscus Shearing (BAMS) (**Fig. 4.1b**) at a substrate temperature of 105 °C and with coating speeds of 10 mm/s. It's noteworthy that the entire fabrication procedure was performed under ambient conditions, and no post-thermal treatments were necessary.

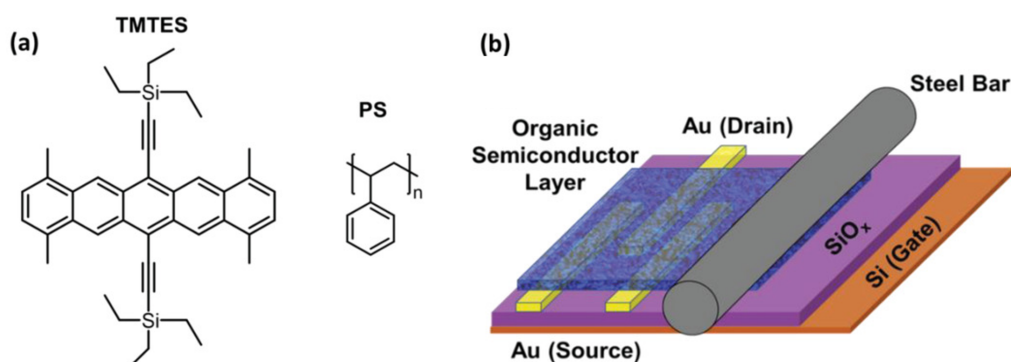


Figure 4.1 (a) Chemical structures of TMTES and PS. (b) Scheme of the BAMS technique for the deposition of the active layer [116].

4.3 Thin Films Characterization

To understand the influence of the vertical phase separation in each film and the related effect on the electrical properties of the devices, a morphological characterization has been performed. The polarized optical microscopy images, displayed in **Fig. 4.2**, reveal that all

the films exhibit polycrystalline spherulitic domains. These domains do not show any clear preferential orientation of the crystals, a morphology that is in alignment with what has been previously observed in TIPS films, as referenced in studies [112, 130]. Notably, the grain size within the channel area appears smaller compared to the SiO_2 regions distant from the electrodes. This difference in grain size can likely be attributed to the gold PFBT treatment, which is known to promote nucleation [131, 132, 133].

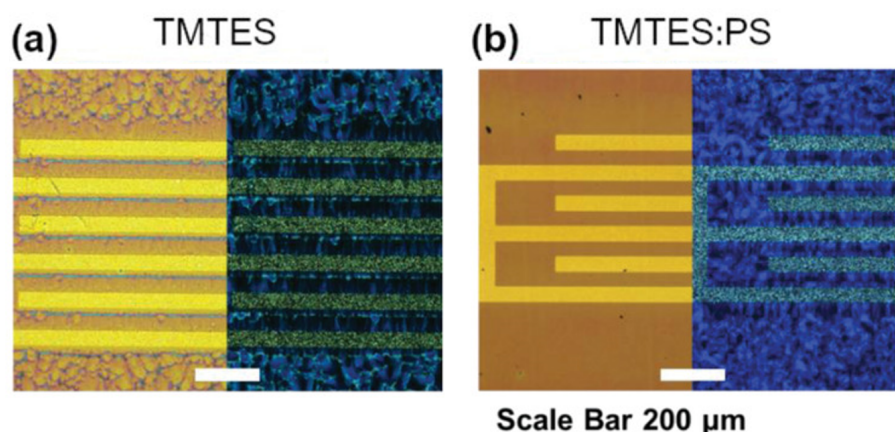


Figure 4.2 Optical microscope images (left) and cross-polarized optical microscope images (right) of (a) TMTES and (b) TMTES:PS thin films deposited by BAMS on a Si/SiO₂ substrate with pre-patterned interdigitated gold electrodes [116].

Further characterization of TMTES and TMTES:PS thin films was conducted using Atomic Force Microscopy, the results of which are presented in **Fig. 4.3**.

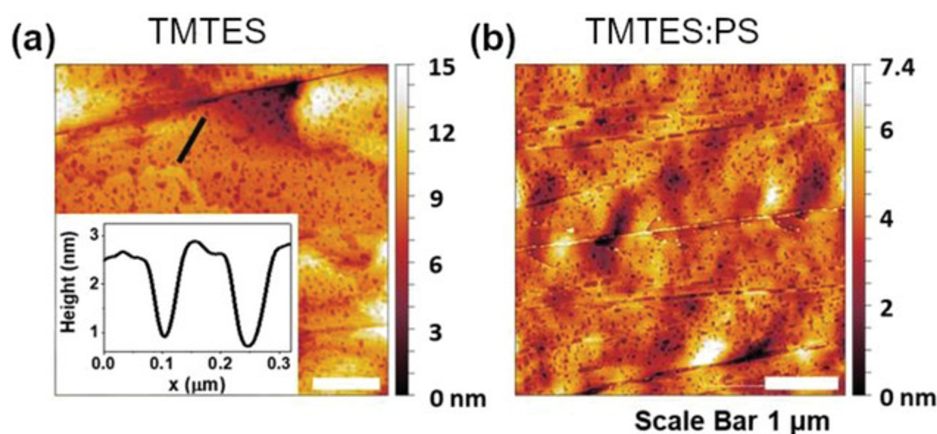


Figure 4.3 AFM topography images of TMTES (a) and TMTES:PS (b) thin films. The inset in (a) corresponds to the height profile along the black line in the figure [116].

The films consistently exhibited step edges with an approximate height of 1.7 ± 0.1 nm, well correlated with the length of an extended molecule, as depicted in the inset of **Fig. 4.3a**. The surface roughness was measured and resulted relatively low, with values of 6.5 ± 1.2 nm for TMTES films and 7.0 ± 3.8 nm for TMTES:PS films. Additionally, the thicknesses of the TMTES and TMTES:PS films were determined to be 22 ± 6 nm and 32 ± 7 nm, respectively.

In literature, two distinct TMTES polymorphs have been identified [134, 135, 136]. TMTES films created from solutions such as drop casting or spin coating are observed to crystallize in the same phase as the previously resolved single crystal structure, referred to as Polymorph I (PI) [134, 135]. This polymorph crystallizes forming a slip-stack structure. More recently, TMTES microcrystals grown from solutions and examined using transmission electron microscopy revealed a novel structure, known as Polymorph II (PII), characterized by a herringbone molecular stacking pattern [136]. X-ray diffraction analysis of the films prepared here indicates that TMTES and also TMTES:PS blend films consistently crystallize in the PII phase (**Fig. 4.4**, **Fig. 4.5**).

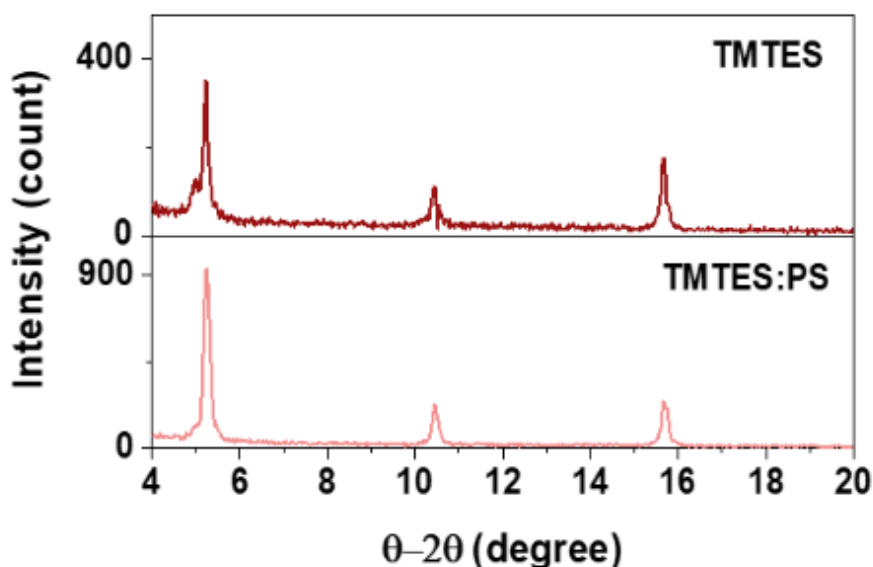


Figure 4.4 X-ray diffractograms of TMTES and TMTES:PS thin films deposited by BAMS [116].

This is demonstrated by the exclusive observation of the (001) reflection peaks, confirming that the crystals align with the *ab* plane parallel to the substrate. This orientation is particularly advantageous for charge transport. Indeed, polymorphism significantly influences device performance [137, 138, 139]. To compare the hole transport characteristics of the two TMTES polymorphs, we analyzed all independent pairwise HOMO-HOMO intermolecular electronic couplings (J_{HOMO}) in both crystal structures using Density Functional Theory (DFT)

based calculations (**Fig. 4.5b** and **Table 4.1**). For the TMTES-PI polymorph, our results revealed a highly anisotropic one-dimensional electronic structure, characterized by a single dominant J_{HOMO} value of 105 meV along the a-axis. In contrast, TMTES-PII demonstrates stronger intermolecular intra-stack couplings ($J_{\text{HOMO}} = 172$ meV), coupled with significant inter-stack electronic interactions. The electronic couplings in PII are distributed across the entire ab plane, indicative of a two-dimensional electronic isotropy, which is more desirable for charge transport [140, 141].

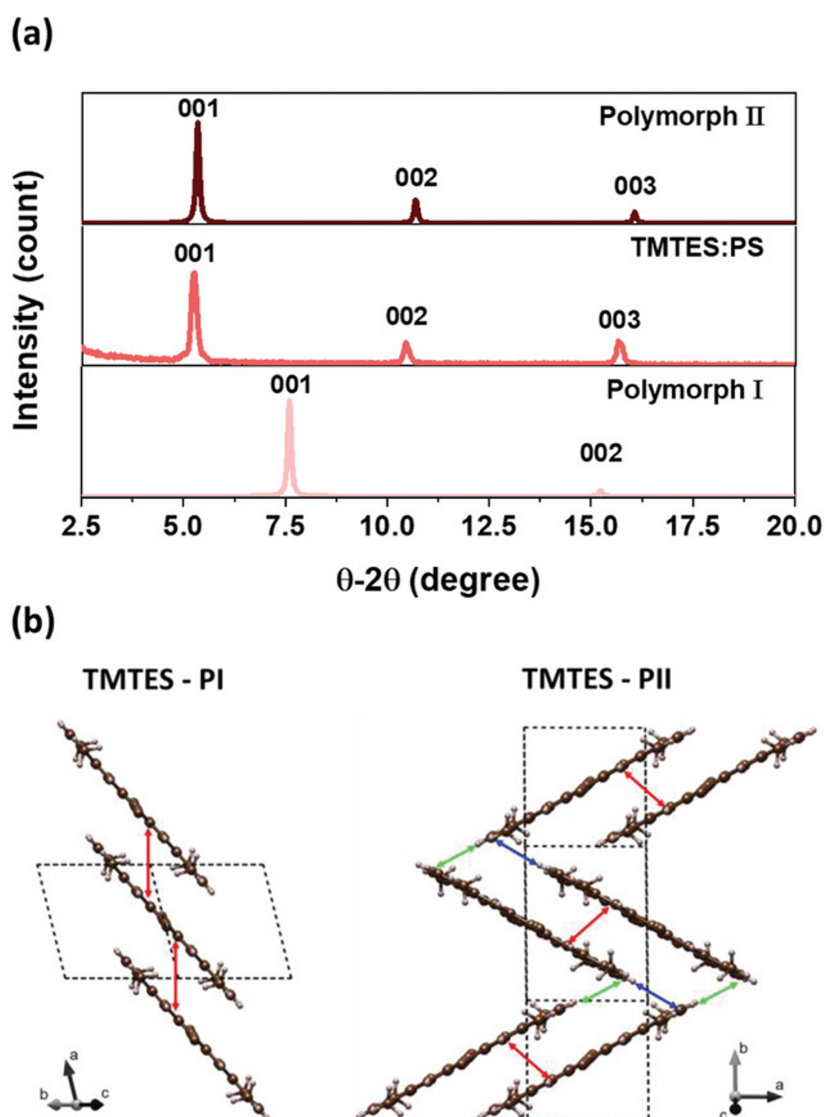


Figure 4.5 (a) X-ray diffractogram of a representative TMTES:PS film together with the simulated diffractograms of the reported polymorphs in the (00l) plane. (b) Crystal packing of TMTES polymorphs PI and PII. The arrows of each color indicate non-equivalent interactions between pairs of molecules in each polymorph respectively [116].

TMTES	Dimer interaction	J_{HOMO} [meV]
PI	1	105
PII	1	172
	2	17
	3	17

Table 4.1 Transfers integrals calculated for non-equivalent dimer interactions in the two polymorphs TMTES-PI and TMTES-PII. The color-coding of the dimer interaction numbers corresponds to the colored arrows in **Fig. 4.5**, indicating different interactions between pairs of molecules

Experimental Methods

The optical microscopy images were taken using an Olympus BX51 equipped with a polarizer and an analyzer. Surface topographies of the thin films were examined by a 5500LS Scanning Probe Microscopy system from Agilent Technologies and subsequent data analysis was performed by using Gwyddion 2.56 software. X-ray diffraction measurements were carried out with a PANalytical X'Pert Pro MRD (Materials Research Diffractometer) diffractometer. The Cu K-alpha radiation 1.54187 \AA was used.

4.4 Electrical Characterization

In our investigation into the electrical behavior of Organic Field-Effect Transistors, we explored the properties of devices with and without PS under ambient conditions. **Table 4.2** collects the electrical parameters extracted for all the devices. In **Fig. 4.6**, transfer and output characteristics of representative OFETs based on both formulations.

TMTES-based OFETs, without the PS binding polymer, show an average mobility of $0.10 \pm 0.03 \text{ cm}^2/\text{Vs}$ and a high positive threshold voltage (V_{th}) of $27 \pm 9 \text{ V}$. This high V_{th} suggests possible unintentional doping of the semiconductor, most likely due to water infiltration at the dielectric interface. Conversely, OFETs using TMTES:PS as the active layer exhibited enhanced performance, operating within a reduced voltage window (5 V) and displaying superior electrical characteristics with less hysteresis and minimal gate voltage-dependent mobility. The threshold voltages for these devices were near 0 V, ranging from -0.5 to -1 V, which supports the beneficial effects of PS in semiconductor processing under environmental conditions.

The TMTES:PS devices showed a high average mobility of $2.6 \pm 0.6 \text{ cm}^2/\text{Vs}$ (maximum mobility found: $3.1 \text{ cm}^2/\text{Vs}$). Anisotropy in mobility, defined as the ratio between mobilities parallel and perpendicular to the coating direction, ranged from 1.4 to 1.2 for TMTES films and 1.1 to 1.3 for TMTES:PS films.

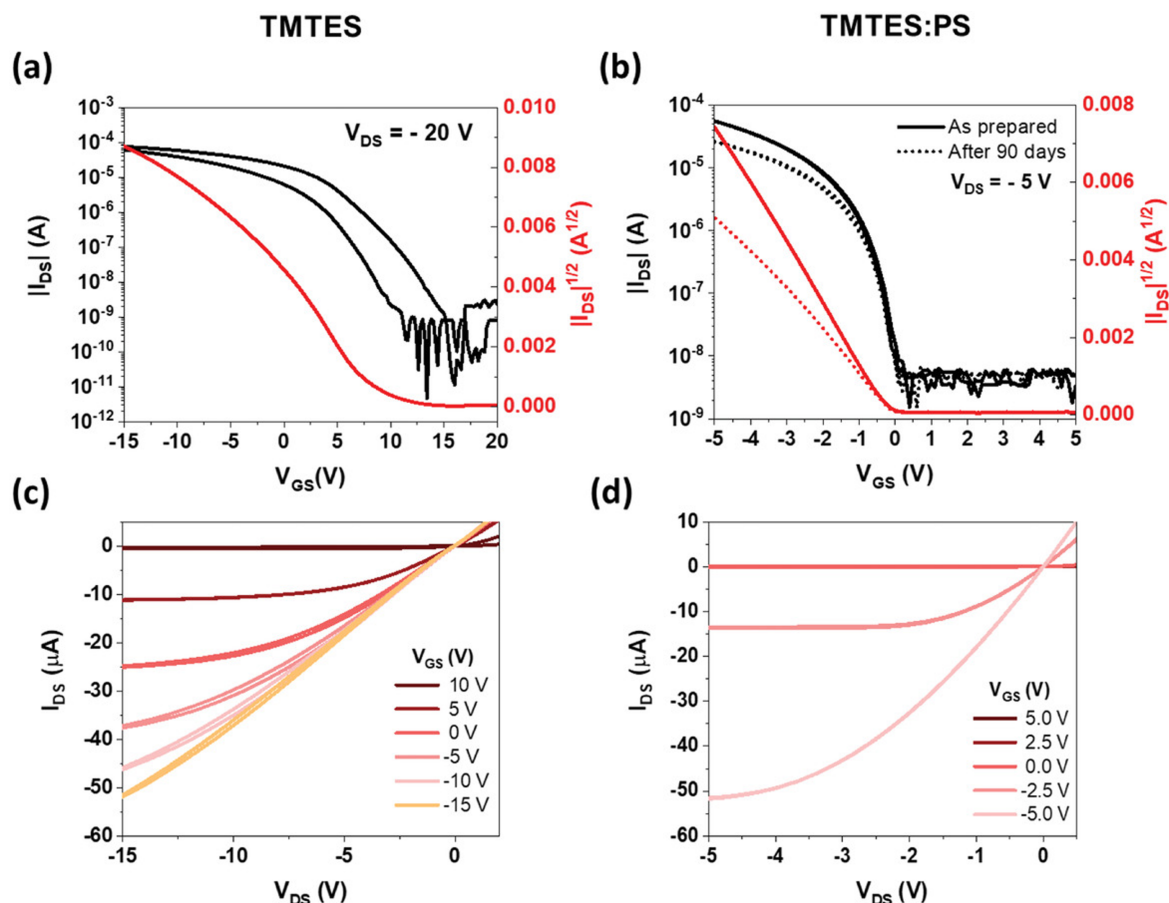


Figure 4.6 Electrical performance of the OFETs devices. Transfer characteristics in saturation regime of representative (a) TMTES and (b) TMTES:PS based OFETs. For the blended films, the device characteristics after 90 days are shown (dashed lines). Output characteristics of representative (c) TMTES and (d) TMTES:PS based OFETs [116].

Furthermore, the majority of charge carrier traps, specifically for holes, estimated from the sub-threshold slope, were one order of magnitude lower in TMTES:PS films (3.9 ± 0.9) $\times 10^{11} \text{ eV}^{-1} \text{ cm}^{-2}$, compared to TMTES films without PS (6.3 ± 1.1) $\times 10^{12} \text{ eV}^{-1} \text{ cm}^{-2}$. This result confirms that the passivation of the dielectric with PS is responsible for the reduction of interfacial traps. The shelf-stability tests also indicated that TMTES:PS devices retained over 50% mobility after 90 days, while the TMTES OFETs exhibited a substantial positive shift in V_{th} over the same period as shown in Fig. 4.7.

Ink Formulation	Mobility ($\text{cm}^2 \text{V}^{-1} \text{s}^{-1}$)	V_{th} (V)	On/Off	μ_{sat} ($\text{cm}^2 \text{V}^{-1} \text{s}^{-1}$)
TMTES	$(1.0 \pm 0.3) \cdot 10^{-1}$	27 ± 9	10^3	0.2 ± 0.3
TMTES:PS	2.6 ± 0.6	-1.1 ± 0.2	10^5	3.1 ± 0.2
TMTES \perp	$(7.4 \pm 1.9) \cdot 10^{-2}$	34 ± 9	10^3	0.1 ± 0.2
TMTES:PS \perp	2.1 ± 0.6	-1.0 ± 0.1	10^5	2.8 ± 0.3

Table 4.2 Electrical parameters of OFETs based on films of TMTES and TMTES:PS. The parameters are calculated for OFETs with the conducting channel parallel (||) and perpendicular (\perp) to the coating direction.

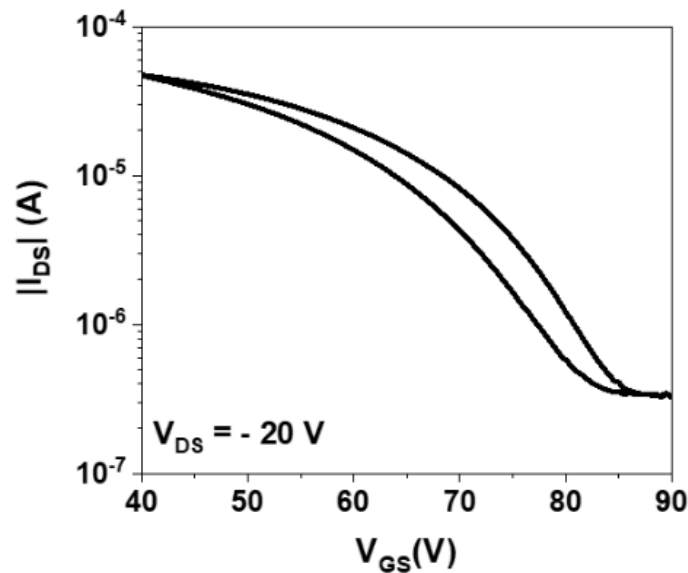


Figure 4.7 Transfer characteristics in saturation regime of TMTES devices measured 90 days after their fabrication [116].

In addition, bias stress measurements under ambient conditions for TMTES:PS OFETs showed only a 1.4 V shift in V_{th} after 5 hours, with saturation mobility decreasing by just 15% (**Fig. 4.8**).

Based on these values, TMTES:PS films can be evaluated as top-performing semiconductors, especially considering the fact that they are produced using a low-cost method that is scalable for commercial manufacturing processes (**Table 4.3**).

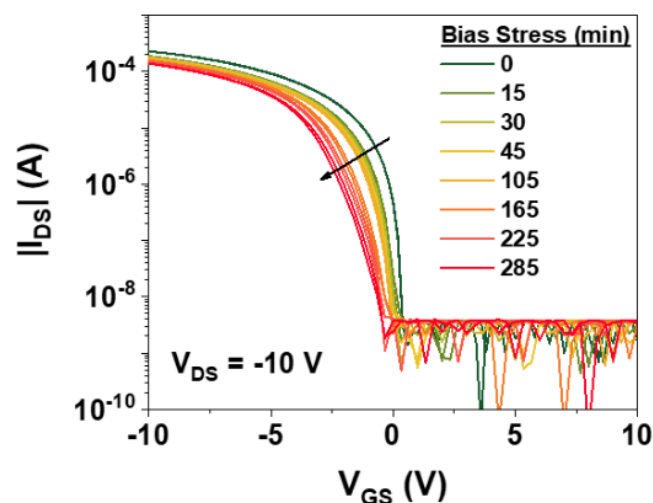


Figure 4.8 Consecutive transfer characteristics of the films TMTES:PS under bias stress ($V_{GS} = -10$ V and $V_{DS} = -1$ V) [116].

OSC Formulation	Scalable to Roll-to-Roll	Binder	μ ($\text{cm}^2\text{V}^{-1}\text{s}^{-1}$)	V_{th} (V)	Ref
2.0 wt % CB (2:1) PS	YES	YES	2.6 ± 0.6	-1	This work
2.0 wt % CB	YES	NO	0.10 ± 0.03	~ 30	This work
0.5 wt % TL	NO	NO	1.3 ± 0.4	NA	[142]
1.2 wt % TE (1:2)	NO	YES	4.3 ± 0.3	~ 10	[143]
4-iPrCN-TAA/C8-Flu (70:30)					
TE	NO	NO	2.6 ± 3.5	~ 40	[144]
1wt % TE	NO	NO	0.3	~ 0	[145]
1 wt% TE (1:1) (iPVN)	NO	YES	0.07	~ 0	[145]
n.r.	NO	NO	1.9		[146]

Table 4.3 Comparison of our results with the electrical transport parameters of solution-processed OFETs based on TMTES reported in literature. Specifically, for OSC Formulation: (CB) chlorobenzene, (TL) toluene, (TE) tetralin, (iPVN) isotactic poly(α -vinyl naphthalene, (4- iPrCN-TAA/C8-Flu) 4-isopropylcyano triarylamine/n-octyl Fluorene, 70/30 copolymer, and n.r. not reported.

For comparison, TIPS OFETs processed with the same PS blending and deposition technique achieved mobilities between 0.5-1 cm^2/Vs and trap densities of $(9.2 \pm 2.8) \times 10^{11} \text{eV}^{-1} \text{cm}^{-2}$ [80]. TMTES films, however, exhibited greater mobilities (from two to four), attributable to the favorable 2D herringbone crystal packing and the reduced interfacial hole traps.

Experimental Methods

These measurements were performed using an Agilent B1500A semiconductor device analyzer connected to the samples with a Karl SÜSS probe station, at ambient conditions. The characteristic field-effect mobility (μ) and threshold voltage (V_{th}) parameters were obtained in saturation regime using the mentioned equation **Eq. (1.14)**. For each ink formulation, the device parameters were extracted from at least 30 devices from two substrates to ensure thin film homogeneity and reproducibility.

The interfacial trap density for the majority charge carriers (i.e., holes) per unit area (N_T) was extracted directly to Subthreshold Swing (SS), and has been estimated using the mentioned equations: **Eq. (1.15)** and **Eq. (1.16)**.

4.5 Chemical Characterization

The surface chemical compositions of TMTES and TMTES:PS films were analyzed using Time-of-Flight Secondary Ion Mass Spectrometry, with the results presented in **Fig. 4.9**.

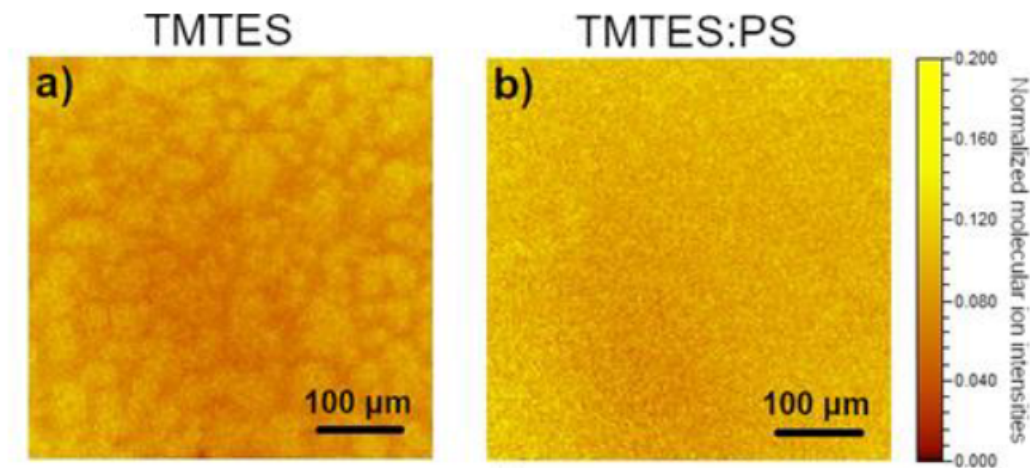


Figure 4.9 TOF-SIMS 2D surface chemical maps of TMTES and TMTES:PS thin films deposited by BAMS at coating speed of 10 mm/s. Normalized (to total counts) sum of $\text{Si}_2\text{C}_{42}\text{H}_{50}^+$ ($m/z = 610.34$), $\text{Si}_2^{13}\text{CC}_{41}\text{H}_{50}^+$ ($m/z = 611.35$), $\text{Si}_2^{13}\text{C}_2\text{C}_{40}\text{H}_{50}^+$ ($m/z = 612.35$), $^{30}\text{SiSi}^{13}\text{CC}_{41}\text{H}_{50}^+$ ($m/z = 613.34$), $^{30}\text{SiSi}^{13}\text{C}_2\text{C}_{40}\text{H}_{50}^+$ ($m/z = 614.35$), and $^{30}\text{SiSi}^{13}\text{C}_3\text{C}_{39}\text{H}_{50}^+$ ($m/z = 615.35$) secondary ion signals from (a) TMTES and (b) TMTES:PS surface acquired outside the interdigitated electrodes [116].

The molecular ion fragment characteristic of TMTES (SiC_3H_9^+ $m/z = 73.05$) was employed to trace the semiconductor distribution over a $500\mu\text{m} \times 500\mu\text{m}$ area. For the blended TMTES:PS film, the TMTES ion signal was found to be uniformly distributed across the surface, indicating an absence of horizontal phase segregation.

To study the vertical distribution of the insulating polymer, TOF-SIMS depth profiling was conducted on the TMTES:PS film (**Fig. 4.10**).

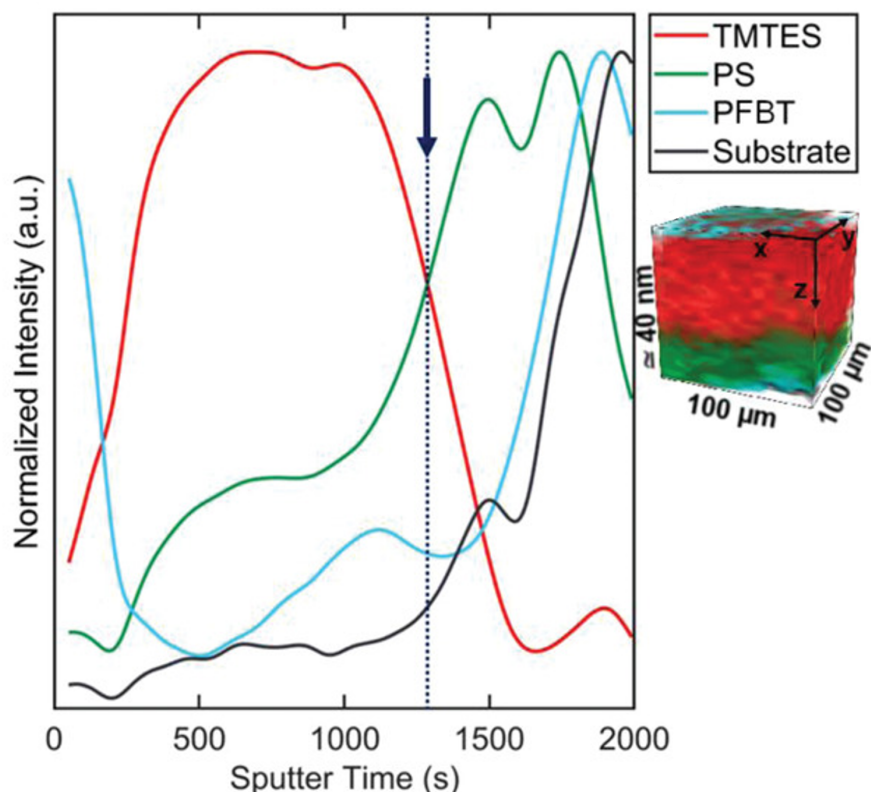


Figure 4.10 TOF-SIMS study of the TMTES:PS thin films. Normalized (to maximum) TOF-SIMS depth profile acquired in the channel area of the OFET starting from the surface and reaching the SiO_2 substrate (black curve). The TMTES signal (red curve) includes the SiC^- , SiCH^- , SiC_2H^- , SiC_5H_2^- , SiC_7H_2^- species; the PS signal (green curve) includes the C_3H_3^- , C_4H_3^- , C_5H_3^- , C_6H_3^- , C_7H_3^- species; the PFBT signal (light blue curve) includes the F^- and S^- species. On the right, 3D rendering of the same species just mentioned, as the sputter time is proportional to the Z-profiling of the layers. The analyzed thickness (40 ± 12 nm) was multiplied by a factor of $2.5 \cdot 10^4$ to better appreciate the multilayer architecture in the 3D rendering. The dashed line and arrow indicate the TMTES-PS transition region [116].

Four representative profiles were taken, corresponding to TMTES, PS, PFBT, and the SiO_2 substrate, by averaging the signal intensities of characteristic secondary ions from each stratified material in the OFETs channel area. Analysis of the characteristic fragments from TMTES and PS confirmed the simultaneous presence of the OSCs and of the insulator. Progressing deeper into the film towards the substrate, the PS ion signals diverged from those

of the OSCs, delineating a well-defined TMTES-PS transition region. Here, the TMTES signal reduced significantly, whereas the PS signal increased. Additionally, the PFBT signal profile revealed an intermediate layer between the PS and the Si/SiO₂ substrate, confirming the effectiveness of electrode functionalization which was applied to enhance charge injection and semiconductor crystallization [132, 133]. The 3D TOF-SIMS map reconstruction of the overlaid signals from the thin film profile is depicted in **Fig. 4.10**. These results, consistent with the previous studies [80, 142], confirm that PS serves as a dielectric passivating layer.

Experimental Methods

TOF-SIMS measurements were performed using a TOF SIMS V instrument (ION-TOF GmbH, Muenster, Germany). The base pressure of the analysis chamber during the TOF-SIMS data acquisition was equal to 1.3×10^{-9} mbar. Bi₃⁺⁺ primary ions at 30 keV provided by a liquid metal ion gun (LMIG) were used for surface analysis. For depth profiling in dual-beam mode, the analysis beam was combined with a sputter ion gun producing Cs⁺ ions at 500 eV. The analysis area of the surface chemical maps was 500 μm × 500 μm. Sputtering was carried out over 300 μm × 300 μm areas inside the OFET active layer. Depth profiles were acquired over 100 μm × 100 μm areas within the center of the sputter crater. The analysis beam (pulse width: 18.4 ns, current: 0.3 pA) and the sputtering beam (current: 6 nA) were employed in non-interlaced mode (1 analysis frame, 1 s sputter, and 1 s pause per cycle) for sample charge compensation. Secondary ions were extracted at 2 kV and detected with a time-of-flight mass analyzer. A cycle time of 100 μs allowed to obtain a mass range from 1 to 900 m/z. The detected secondary ions had negative and positive polarity. Negative and positive mass spectra were calibrated using CH⁻, Si⁻, C₅⁻, and C₄₂H₅₀Si₂⁻, and H⁺, CH⁺, CH₃⁺, and C₄₂H₅₀Si₂⁺ signal peaks, respectively. The mass resolution achieved was more than 6000 m/Δm for all the analyzed masses. Mass spectra and depth profile signals were exported for further analysis by SurfaceLab v6.5 software. A list of characteristic secondary ions was obtained for TMTES and PS mass spectra through a multivariate analysis approach.

4.6 X-Ray Detection

In this section, the application of Organic Field-Effect Transistors as X-ray detectors will be briefly discussed. This aspect will be explored in depth in **Chapter 5** of this thesis where a work-in-progress study related to the optimization of OFETs as X-ray detectors will be shown.

The enhanced transport characteristics of TMTES:PS films, suggested the use of this organic thin film as X-ray detectors. These devices, when irradiated and operating in the

saturation regime ($V_{DS} = -15$ V and $V_{GS} = -20$ V), displayed measurable currents between the source and drain during successive beam on/off cycles. Real-time current responses to varying radiation dose rates revealed photoconversion dynamics typical of organic microcrystalline thin films, influenced by a photoconductive gain attributed to minority carrier traps within the semiconducting layer (**Fig. 4.11**) [147]. This facilitates the detection of high-energy photons using low-absorbing, tissue-equivalent materials like full-organic thin films.

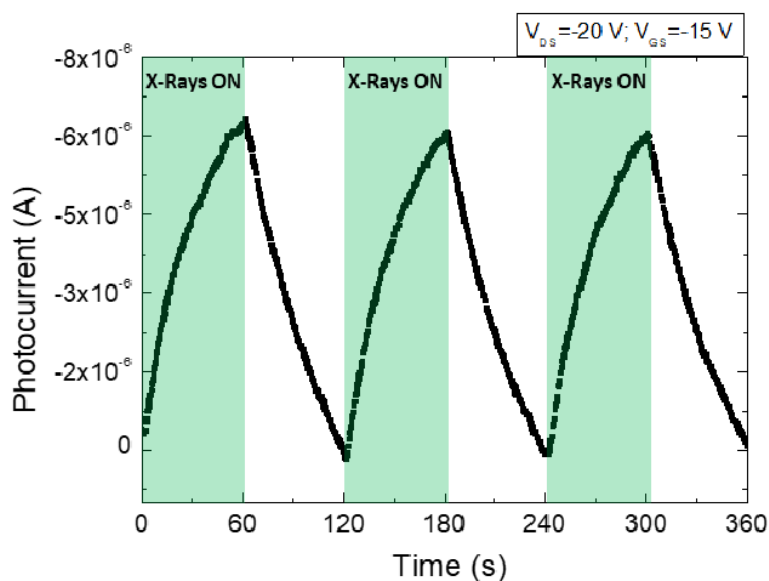


Figure 4.11 X-ray induced photocurrent response of a TMTES:PS BAMS-coated device upon three on/off switching cycles (green areas correspond to time windows of 60 s) employing a dose rate of 9.8 mGys^{-1} [116].

The photocurrent gain, a critical factor for sensitivity, is the ratio of the minority charge carriers' lifetime (τ_r), trapped within the material, to the majority charge carriers' transit time across the channel (τ_t). The transit time depends on the charge transport efficacy and it is inversely proportional to the mobility of the majority carriers ($\tau_t = L^2/\mu V$, where L is the channel length and V the applied bias). Sensitivity can thus be amplified by modulating electron trap density, such as by adjusting grain boundary density, and by refining hole transport in the active layer through structural and interfacial enhancements [80].

Sensitivity to X-rays was quantified by the photocurrent's dose rate-dependent slope, reaching $(4.10 \pm 0.05) \times 10^{10} \mu\text{C Gy}^{-2} \text{ cm}^{-3}$ as shown in **Fig. 4.12a**. This is better than previous benchmarks for fully organic, tissue-equivalent active layers and also exceeds the sensitivity of many perovskite-based detectors (**Fig. 4.12b**).

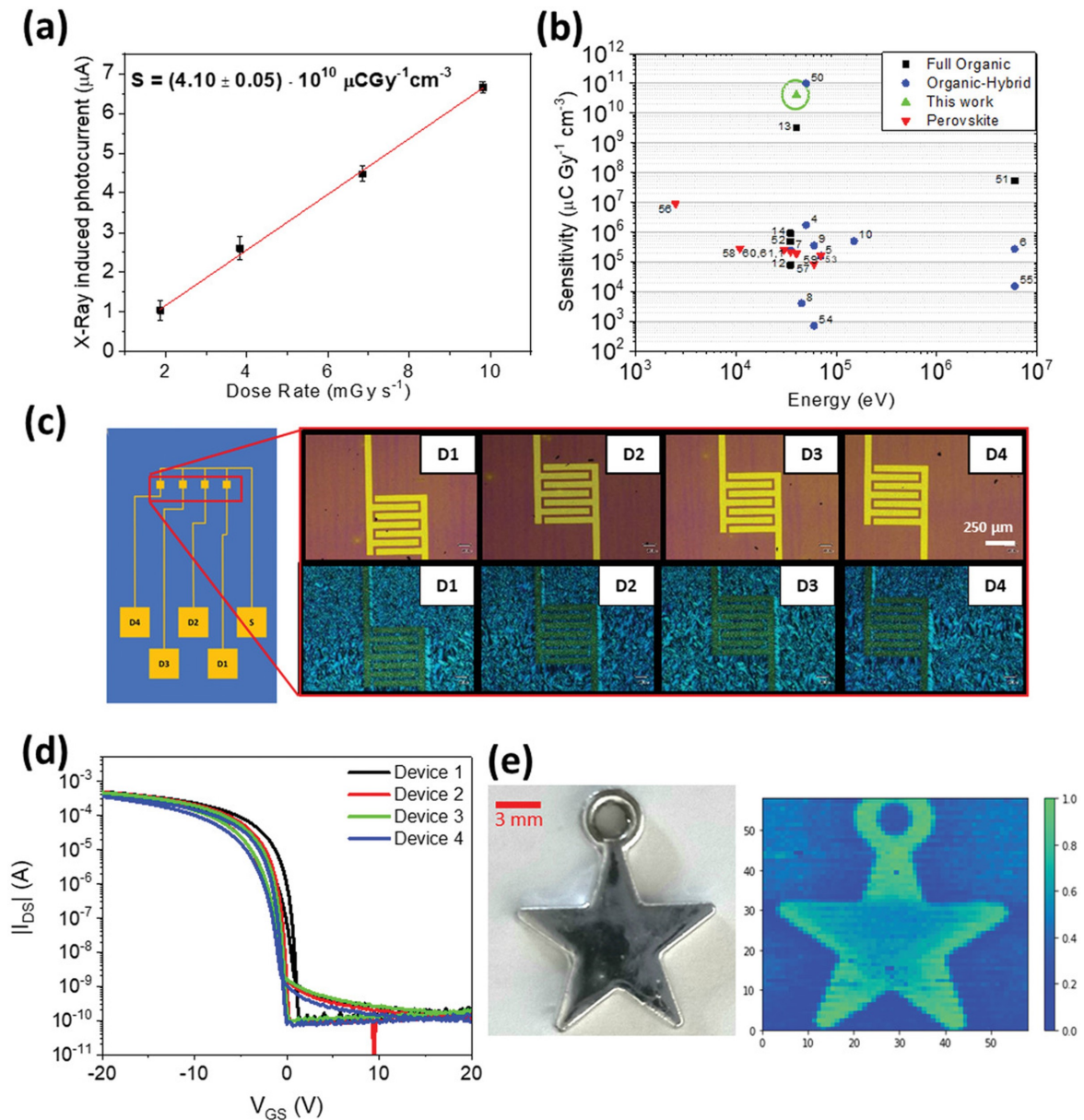


Figure 4.12 X-ray detection of TMTES:PS film-based devices. **(a)** X-ray induced photocurrent as a function of the dose rate. The sensitivity is estimated as the slope of the linear fit of the experimental points and results in the top value reported in the inset. **(b)** Comparison of the sensitivity values per unit volume achieved in this work (green triangle), with those reported at the state of the art for thin film detectors based on perovskite (red triangles), organic-hybrid (blue circles), and full-organic (black squares) active layers. **(c)** Layout and POM images of the 4 pixels array BAMS printed TMTES:PS detector. **(d)** OFETs transfer characteristics of the 4 pixels of the array. **(e)** Photograph (right) and corresponding X-ray image by a single pixel device (left) of an aluminum star [116].

Despite the ultra-thin profile of our films, the sensitivity per unit area remains remarkable. Notably, the sensitivity is comparable to that of hybrid organic-perovskite thin film detectors, traditionally deposited via non-scalable spin coating processes [148]. Moreover, the exclusion

of lead-halide perovskite from the active layer maintains the tissue equivalence of the detector, a significant advantage for medical dosimetry applications.

The high detection capabilities of the TMTES:PS thin films are attributed to their excellent transport properties, resulting from the production of highly crystalline films, and their electrical stability, enhanced by the passivating effect of PS, experimentally demonstrated from TOF-SIMS depth-profiling measurements.

Demonstrating the practical application and reliability of our devices as large-area detectors for medical purposes, we constructed a 4-pixel array and conducted tests at the Synchrotron Radiation for Medical Physics (SYRMEP) beamline of the ELETTRA light source in Trieste, Italy. SYRMEP was an ideal test for its capabilities in biomedical imaging research, offering an X-ray energy range of 8.5–35 keV and dose rates suitable for diagnostic mammography (0.05–35 mGy/s).

The uniformity of the coating, resulting from the employment Bar-Assisted Meniscus Shearing technique, was evident in the consistent morphologies captured in Polarized Optical Microscopy (POM) images. Furthermore, the congruent OFETs transfer characteristics of the 4 pixels, as illustrated in **Fig. 4.12c** and **Fig. 4.12d**, corroborate the uniformity.

The X-ray projection image of a star-shaped metal object, displayed in **Fig. 4.12e**, reveals sharp contrast and confirms the detector's consistent performance across 3600 exposures under identical experimental conditions. The achieved lateral resolution of 250 μm , limited by the device's dimensions and the collimation of the X-ray beam, is notable. Remarkably, the high X-ray sensitivity of the TMTES-based detectors allowed to use sub-millimeter pixel sizes, which is highly advantageous for the development of portable, large-area X-ray panels.

Experimental methods

Two different X-ray beam sources were employed for the characterization of the detectors:

- Hamamatsu L12161 X-ray tube with tungsten target was used at fixed 40 kV operating voltage the filament current was changed between 100 and 500 μA leading to an incident dose rate on the samples between 318 and 1665 $\mu\text{Gy s}^{-1}$. The dose rate calibrations were previously performed employing the Barracuda radiation detector. The modulation of the beam was obtained with a mechanical lead shutter placed close to the X-ray tube window. Keithley SMU 2614 was used in combination with a LabVIEW program for electrical signal acquisition.
- A monochromatic and aligned synchrotron X-ray beam with energy of 12 keV and dose rate in the range 0.05–35 mGy s^{-1} . Synchrotron measurements were carried out at ELETTRA (Trieste), in the SYRMEP beamline equipped with an ionization chamber

for real-time dose rate monitoring. In addition, precision slits and a CCD camera allow to focus the beam and to control the irradiated area of the samples.

4.7 Conclusions: Role of Vertical Phase Segregation on Performance and Stability

In this work, we explored the fabrication and application of thin films made from OSCs TMTES and TMTES blended with PS, using an advanced high-throughput printing technique. These thin films demonstrate a unique herringbone crystallization pattern, fostering two-dimensional electronic interactions. A central aspect of our investigation is the role of PS in these blended films. Notably, OFETs incorporating these blended films outperformed those made from unblended OSCs in terms of device performance and stability. The TMTES:PS based OFETs particularly excelled, showing almost zero threshold voltage, low operation voltage, and an impressive average mobility of $2.6 \text{ cm}^2 \text{ V}^{-1} \text{ s}^{-1}$. Additionally, the inclusion of PS significantly reduced the density of hole traps, attributed to vertical phase separation during crystallization, which effectively passivates the dielectric surface.

A pioneering aspect of this research involved the application of these OFETs devices as X-ray detectors. They exhibited extraordinary X-ray sensitivity, reaching $(4.10 \pm 0.05) \times 10^{10} \mu\text{C Gy}^{-1} \text{ cm}^{-3}$, surpassing most perovskite film-based detectors in this domain. To illustrate the potentiality of the X-ray detector, we designed an array of four pixels to image a metallic object in an X-ray beamline, simulating a medical radiography scenario. This research underscores the vast potential of using high-performance, cost-effective OFETs with human-tissue equivalent organic materials as active layers. Such devices promise revolutionary advancements in large-area, highly sensitive X-ray detectors, opening new horizons in medical dosimetry and diagnostic imaging applications.

5

Optimization of PS Concentration and PS Molecular Weight in Blended Thin Films

Building upon the investigations presented previously (**Chapter 4**), in this chapter, ionizing radiation detectors, key elements for the application for the Organic Field-Effect Transistors (OFETs) are examined. In particular, the effect of Polystyrene (PS) concentration and molecular weight variations on the different TMTES:PS ratios, on the influence of the efficacy of OFETs in detecting ionizing radiation will be studied.

The study is focused on three specific ratios (4:1, 2:1, and 1:2) each of one combined with PS of different molecular weights (M_w): 280,000 g/mol, 100,000 g/mol, and 10,000 g/mol. This approach allows us to investigate how the concentration and molecular weight of PS affect the electrical properties and stability of OFETs devices.

The purpose is to determine the optimal conditions for PS incorporation that enhance OFETs performance, particularly in applications involving X-ray detection. This research is pivotal in advancing our understanding of the interplay between semiconductor materials and polymer additives, potentially leading to a significant improvement in the functionality and efficiency of organic electronic devices.

5.1 Ionizing Radiation Detectors

The detection of ionizing radiation, encompassing high-energy photons like X- and gamma-rays and particles such as neutrons or electrons, is a critical process with widespread applications in various industrial and socially significant fields. This includes microelectronics, quality control, nuclear waste monitoring, and medical imaging [149]. Effective radiation detection systems are important to ensure safety, accuracy, and innovative solutions.

Historically, inorganic semiconductor materials, such as silicon, have been at the forefront of radiation detection technologies [150]. Due to the properties in charge, the inorganic semiconductor materials have been chosen and they showed remarkable detecting performances. However, despite this significant performance, some challenges have to be faced, particularly

in maintaining the purity and uniformity of the material, which often determines significant costs. In light of cost reduction, materials like amorphous silicon (a-Si), amorphous selenium (a-Se), and polycrystalline Cadmium Zinc Telluride (poly-CZT) have been employed for the realization of large-area detectors, achieving a good balance between performance and costs [151].

Solid-state ionizing radiation detectors, pivotal in numerous applications ranging from medical imaging to security, are broadly classified into two categories, indirect detection, and direct detection (see **Fig. 5.1**) [151]. The first category, indirect detection, employs a two-step process. Initially, high-energy radiation is converted into visible photons by scintillating materials [151]. These photons are then detected by a photodiode, which converts them into an electrical output signal. Scintillators, such as sodium iodide (NaI) doped with thallium or bismuth germinate (BGO), are chosen for the high photon yield and compatibility with the spectral response of the photodiode, typically a photomultiplier tube or a solid-state photodiode. This indirect method is particularly advantageous in applications requiring high sensitivity and large-area coverage, as in medical imaging modalities like Positron Emission Tomography (PET) and Computed Tomography (CT) scans [152].

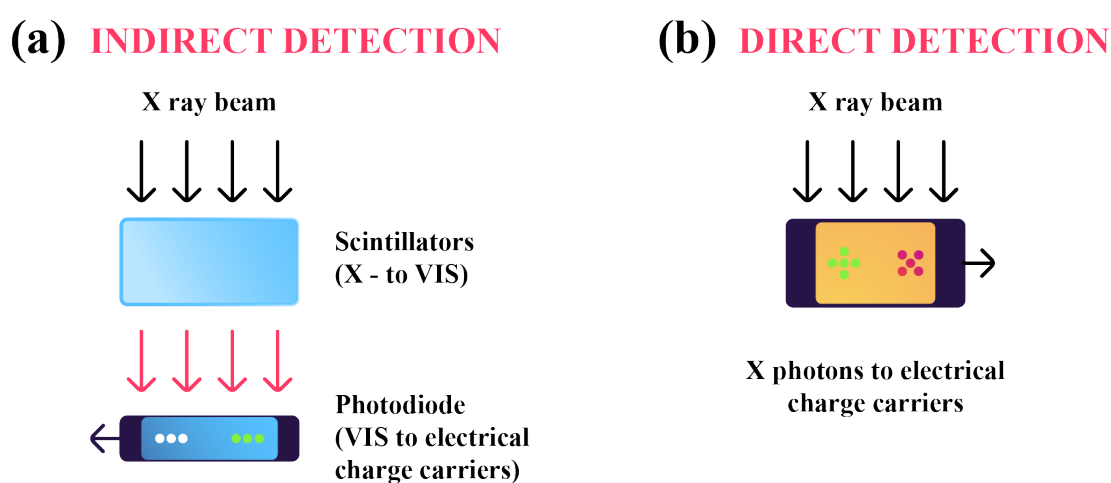


Figure 5.1 Schematic illustration of the (a) indirect and (b) direct radiation detection mechanisms

Direct detectors, as the name suggests, directly transduce high-energy radiation into an electrical output signal through a single-step process. In this mechanism, semiconducting materials, such as silicon, germanium, or Cadmium Zinc Telluride (CZT), absorb the ionizing radiation and generate electron-hole pairs [151]. The quantity of these pairs is proportional to the energy of the incident radiation, thereby providing a direct measure of the intensity. This direct conversion provides advantages in terms of energy resolution and response time,

and therefore it is highly suitable for applications requiring high precision and real-time detection, such as gamma-ray spectroscopy and high-resolution radiography [147].

Each detection method has specific advantages and limitations. Indirect detectors, while beneficial for the high efficiency in photon conversion and suitability for large-area applications, often have limitations in spatial resolution and response speed. On the other hand, direct detectors, showing superior energy resolution and faster response times, are limited by factors like material cost, complexity in high-purity semiconductor fabrication, and challenges in scaling up for large-area coverage [153, 150].

Further advancements in material science, particularly developing new scintillators, with improved light yield, and semiconductors, with higher charge mobility, will enhance the performance of both indirect and direct radiation detectors. Additionally, emerging technologies such as hybrid detection systems, which combine the strengths of both indirect and direct methods, are being explored to overcome specific limitations and to provide more versatile and efficient detection solutions [154].

When high-energy radiation hits the sensor, it generates primary excitons. Then, these primary excitons interact with the active volume of the sensor, typically a semiconductor, producing a substantial number of secondary products, namely electron/hole pairs. In semiconductor detectors, an electric field is applied to separate these induced charges, enabling the measurement of a photocurrent proving the evidence of the absorbed high-energy radiation.

Several criteria have to be met to allow a semiconductor can act as an active material in radiation detection. The most critical one is a high atomic number (Z -number) and a substantial density to maximize the radiation absorption. Additionally, the semiconductor's energy gap should be ideally greater than 1.5 eV to reduce the intrinsic carrier concentration and thus lower the dark current, remaining below 5 eV to minimize the energy required for electron-hole pair generation [149]. The charge transport properties are important as well, particularly a high product of charge carrier mobility and lifetime, to ensure efficient collection of photogenerated charges.

This chapter will analyze the direct detection of radiation using organic semiconductor materials, a method characterized by rapid response and superior signal-to-noise ratio. The efficiency and effectiveness of this approach are highlighted by the fundamental interactions between high-energy radiation and the semiconductor sensor.

5.1.1 Detectors Based on Thin Films Organic Semiconductors

In recent years, an innovative approach has emerged with the employment of organic semiconductors as active materials in radiation detection systems [155, 156]. Organic semiconductors

offer the possibility to employ solution-based processing techniques, which are pivotal in fabricating large-area, low-cost, and flexible organic devices. This marks a significant departure from traditional inorganic semiconductor devices, which are typically characterized by rigidity, heaviness, high power consumption, and small active detection area. The intrinsic properties of organic materials, such as flexibility and the potential for large-scale production at a lower cost, pave the way to innovative applications. These span across various fields, including medical diagnostics, public safety, space exploration, cultural heritage preservation, and environmental monitoring.

The concept of using organic semiconductor materials for the indirect detection of ionizing radiation was first introduced in the early 1960s [152]. Initially, these materials were mainly considered for their scintillating properties. As illustrated in **Fig. 5.1a**, the indirect detection mechanism involves a two-step process where incoming ionizing radiation is first converted into visible photons by a scintillator and then transformed into an electrical signal by a photodiode. This process, although effective, has certain limitations in terms of efficiency and response time.

Conversely, the direct detection mechanism, as shown in **Fig. 5.1b**, offers a more streamlined approach by transducing ionizing radiation into an electrical signal within the same device. Actually, this method is largely employed in research due to the ability to enhance the signal-to-noise ratio and reduce the response time of the detection system. The integration of organic semiconductors in direct detection mechanisms represents a significant advancement, combining the benefits of organic materials with improved detection efficacy [147, 155].

Primarily, the need to mitigate the energy loss, due to charge recombination, needs a high charge carrier mobility for efficient charge collection. This is particularly critical in the context of organic semiconductor materials, where intrinsic properties, such as crystallinity, influence significantly the dynamics of charge transport. The enhancement of crystallinity facilitates charge transport and also optimizes the X-ray detection capabilities. For instance, a photodetector built on micro-crystalline 6,13-bis(triisopropylsilylethynyl)pentacene (TIPS) and deployed on flexible poly(ethyleneterephthalate) (PET) substrates demonstrated a noteworthy X-ray sensitivity of 200 nC/Gy [147]. Additionally, the integration of an OFETs architecture allowed for tunable detection capabilities under varying biasing conditions, leading to a significant sensitivity enhancement up to 1200 nC/Gy [157].

Furthermore, the challenge of low radiation absorption in organic materials, determined by the low atomic number (Z), requires innovative strategies to enhance the detection efficacy. Despite the use of thicker films that can increase active volume, these films adversely impact the device's bendability and require higher operating voltages. Therefore, alternative approaches, such as incorporating high- Z nanoparticles or quantum dots, or embedding

carbon nanotubes within the organic matrix, are needed. A notable advancement has been the molecular modification of TIPS to include heavier atoms (e.g., substituting Si with Ge to create TIPGe-pentacene), substantially enhancing sensitivity to a value of 4460 nC/Gy, rivaling even some advanced inorganic materials [158]. This represents a remarkable value for organic thin-film X-ray detectors and it is competitive with the performance of some state-of-the-art inorganic materials currently employed in the creation of large-area detectors [159].

Furthermore, the exploration of physical processes governing high-energy photon detection in low-Z molecular systems is crucial. Traditional understanding, based on electron-hole pair generation in inorganic semiconductors, needs to be reevaluated in the context of organic systems. A pioneering study by L. Basiricò et al. revealed that the photocurrent in micro-crystalline TIPS films was significantly higher than expected considering only the photogenerated charge collection [147]. This led to the hypothesis of a photoconductive gain effect: trapped electrons in deep states within the organic material induce a continuous emission of holes from the injecting electrode, thereby amplifying the photocurrent.

The possibility of obtaining a fine-tuning of electron trap density within the active material, to further enhance X-ray sensitivity in organic detectors, presents an interesting research perspective. Additionally, the impact of thin film morphology on X-ray sensitivity remains underexplored due to limitations in controlling morphological features in solution-based techniques. Innovative deposition techniques such as Bar-Assisted Meniscus Shearing (BAMS) have shown promise in achieving uniform, highly crystalline thin films, beneficial for OFETs with high field-effect mobility. Moreover, manipulating deposition parameters and ink formulations in BAMS can influence film morphology, while the use of blends comprising an organic semiconductor and an insulating polymer can improve the processability, homogeneity, and environmental stability of the thin films.

5.1.2 Photoconductive Gain Effect

In highly ordered crystalline semiconductors and polycrystalline film-based photodiodes, the detection mechanism of high-energy photons predominantly involves charge collection dynamics, as illustrated in **Fig. 5.2a**. On the contrary, a distinct phenomenon known as photoconductive gain, referenced in the literature as [123], plays a pivotal role in thin film-based semiconductor radiation detectors. **Fig. 5.2b** depicts this process: the generation of electron-hole pairs by absorbed radiation leads to the trapping of minority carriers, thereby amplifying the collected photo-charges by a factor G . To preserve charge neutrality, majority carriers are continually re-injected from the ohmic contacts into the conductive channel,

contributing repeatedly to the total photocurrent. This mechanism allows the internal quantum efficiency of the detector to surpass 100%, resulting in exceptionally high sensitivity values.

The internal amplification process can be quantitatively described by the gain factor G , defined as the ratio of the recombination time τ_r to the transit time τ_t , as shown below:

$$G = \frac{\tau_r}{\tau_t} \quad (5.1)$$

$$\tau_r = \frac{\alpha}{\gamma} \left[\ln \left(\frac{\rho_0}{\rho_X} \right) \right]^{1-\gamma} \quad (5.2)$$

$$\tau_t = \frac{L^2}{\mu V} \quad (5.3)$$

Here, α , γ , and ρ_0 are material-specific constants describing the characteristic timescale and the dispersion of trap states, along with a reference carrier density, respectively. ρ_X represents the photogenerated carrier concentration, L the channel length, μ the electrical mobility, and V the applied bias voltage.

The recombination and transit times are crucial to describe the dynamics of minority carrier recombination and the transit of majority carriers through the conductive channel, respectively.

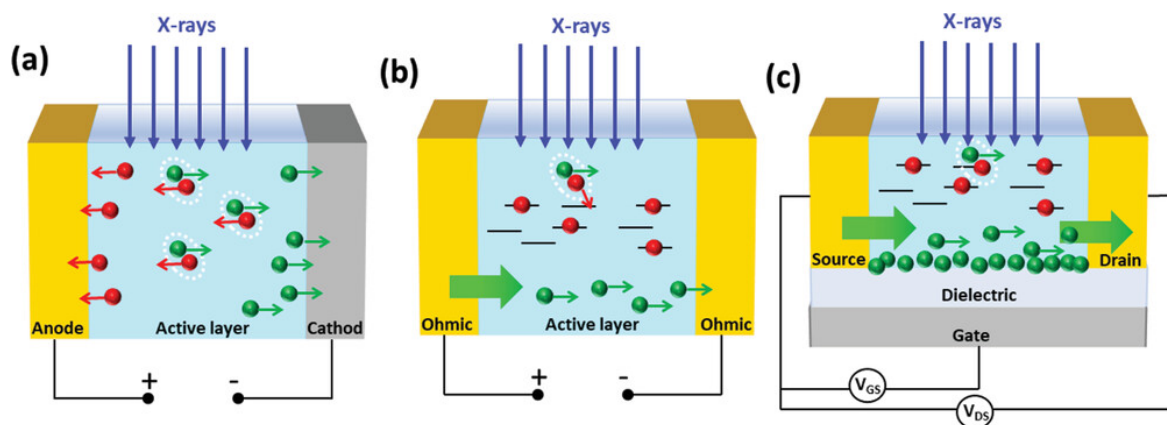


Figure 5.2 Schematics of the direct X-ray detection processes. (a) Charge collection in photodiode architecture. (b) Photoconductive gain in photoconductor architecture. (c) Photoconductive gain in phototransistor architecture [160].

In 2016, Basicicò et al. introduced a model to describe the photoconductive gain effect in organic thin film photoconductors based on TIPS-pentacene and derivatives, as referenced in [147]. Despite the minimal X-ray absorption (approximately 0.0015% for a 100 nm thick TIPS-pentacene polycrystalline film) attributable to low-Z elements in the absorbing material and the thin active layer, the model demonstrated the possibility of recording significantly

high photocurrents, resulting in high sensitivity values ($S = 7.7 \times 10^4 \mu\text{C Gy}^{-1}\text{cm}^{-3}$). The authors further elucidated the slow recombination dynamics using stretched exponential curves and calculated gain values up to 4.7×10^4 [147].

A primary strategy, to maximize the photoconductive gain mechanism, involves the use of a phototransistor architecture. As shown in **Fig. 5.2c**, the application of gate polarization enhances the charge density in the OFETs channel (i.e., ρ_0), promoting both minority carrier trapping as well as majority carrier conduction. Moreover, in the over-threshold condition, τ_t decreases. Utilizing these phenomena, Lai et al. in 2017 reported a higher gain factor ($G = 3 \times 10^5$) and increased sensitivity ($4.8 \times 10^5 \mu\text{C Gy}^{-1}\text{cm}^{-3}$) compared to the coplanar architecture, as referenced in [158].

5.2 Device Fabrication

1,4,8,11-Tetramethyl-6,13-triethylsilylethynylpentacene (TMTES) and Polystyrene (PS) with molecular weights of 280,000 g/mol, 100,000 g/mol, and 10,000 g/mol were acquired from Ossila and Sigma–Aldrich respectively (chemical formula in **Fig. 4.1a**). Solutions of TMTES and PS were prepared in anhydrous chlorobenzene at a concentration of 2.0% w/w. For blending, the TMTES and PS solutions were combined in different volume ratios of TMTES to PS, specifically 1:0, 4:1, 1:2, 2:1. Before the coating, these solutions were heated to reach the appropriate substrate temperature for the coating process.

The device fabrication is the same as reported in **Section 4.2**. For completeness, the chemical structures and the scheme of the device are reported in **Fig. 5.3**.

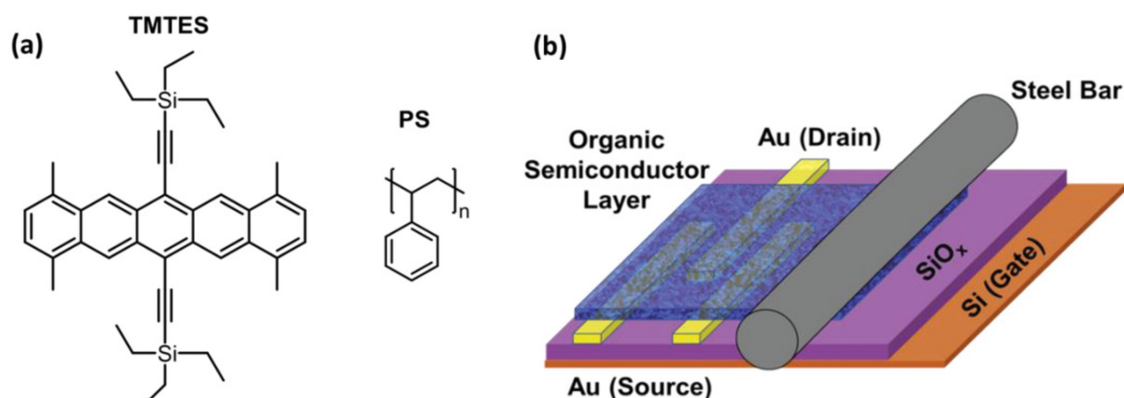


Figure 5.3 (a) Chemical structures of TMTES and PS. (b) Scheme of the BAMS technique for the deposition of the active layer [116].

Moreover, in this chapter, the experimental methods employed will not be detailed, as they are the same as those extensively described in the previous **Chapter 4**.

5.3 Thin Films Characterization

A morphological characterization has been performed to understand the role of the PS amount in each film and the related effect on the electrical properties of the devices. The optical microscopy and the polarized optical images are shown in **Fig. 5.4**, **Fig. 5.5**, and **Fig. 5.6**, following the order of the films from the lowest to the highest PS amount.

All the films exhibit polycrystalline spherulitic domains. These domains do not show any clear preferential orientation of the crystals, a morphology that aligns with what has been previously observed in **Section 4.3**. As previously observed, the grain size within the channel area appears smaller compared to the one observed in the regions far from the electrodes, due to the already mentioned nucleation phenomenon [131, 132, 133].

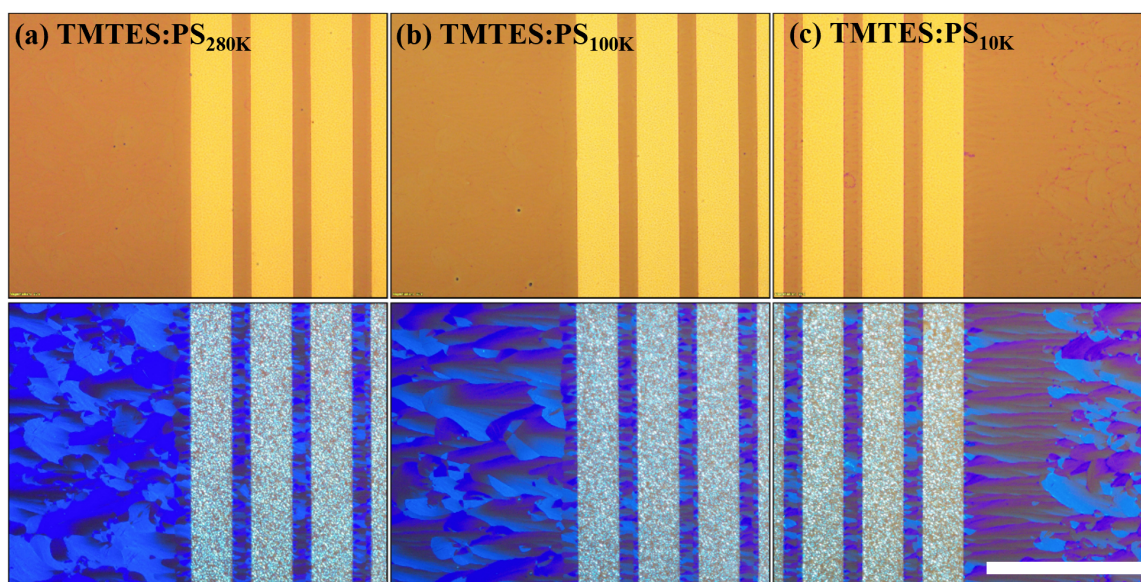


Figure 5.4 Optical (top) and polarized optical (bottom) microscopy of: **(a)** TMTES:PS_{280K}; **(b)** TMTES:PS_{100K}; **(c)** TMTES:PS_{10K}. Scale bar 200 μm . Solutions were combined in 4:1 volume ratios.

The samples with a 4:1 ratio (**Fig. 5.4**) exhibit plate-like crystals, and the surface appears smoother compared to the others. This observation needs further investigation through Atomic Force Microscopy (AFM) measurements. Additionally, variations in the molecular weight of PS within the same ratio did not result in significant morphological differences in the channel area.

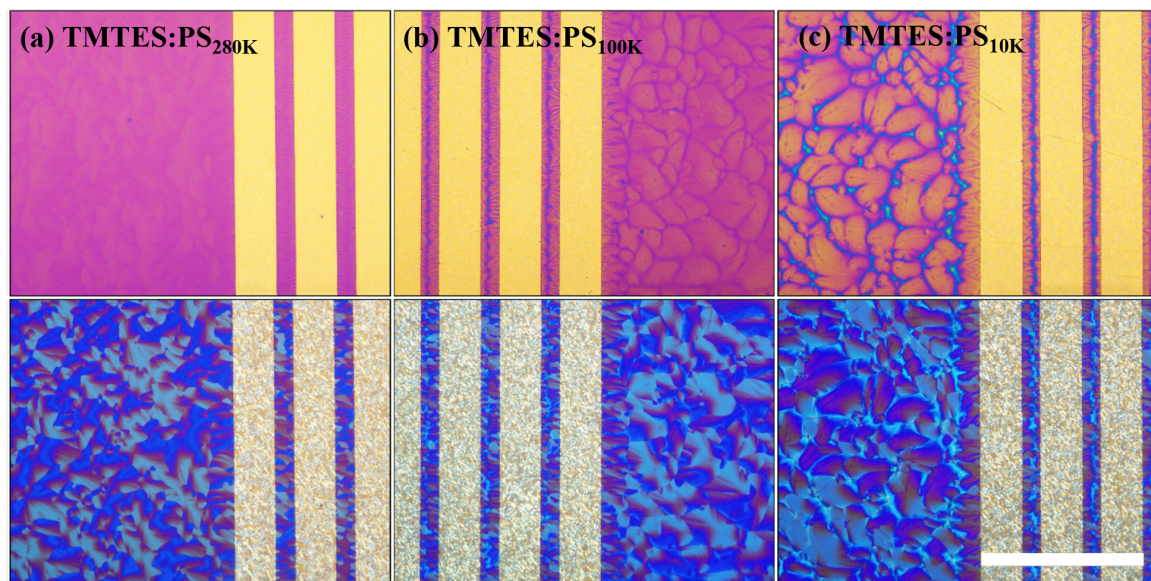


Figure 5.5 Optical (top) and polarized optical (bottom) microscopy of: (a) TMTES:PS_{280K}; (b) TMTES:PS_{100K}; (c) TMTES:PS_{10K}. Scale bar 200 μm . Solutions were combined in 2:1 volume ratios.

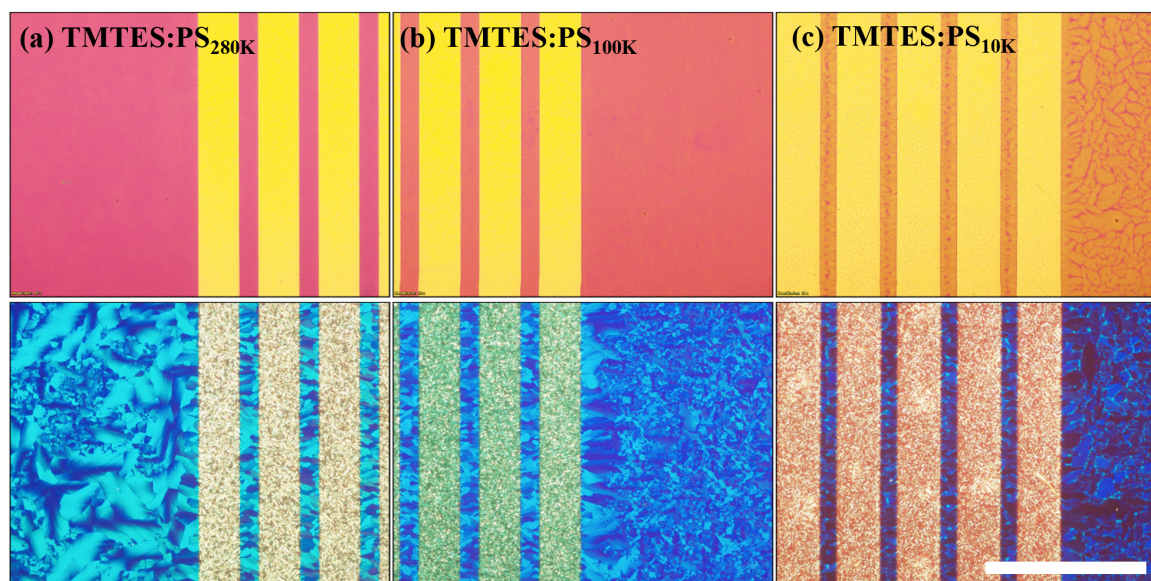


Figure 5.6 Optical (top) and polarized optical (bottom) microscopy of: (a) TMTES:PS_{280K}; (b) TMTES:PS_{100K}; (c) TMTES:PS_{10K}. Scale bar 200 μm . Solutions were combined in 1:2 volume ratios.

X-ray diffraction analysis (**Fig. 5.7**) of the realized films shows that all ratios of TMTES:PS blend films, with all PS molecular weights, consistently with our previous study (**Section 4.3**), crystallize in the Polymorph II phase, characterized by a herringbone molecular stacking pattern which is advantageous for charge transport (**Fig. 4.4**, **Fig. 4.5**).

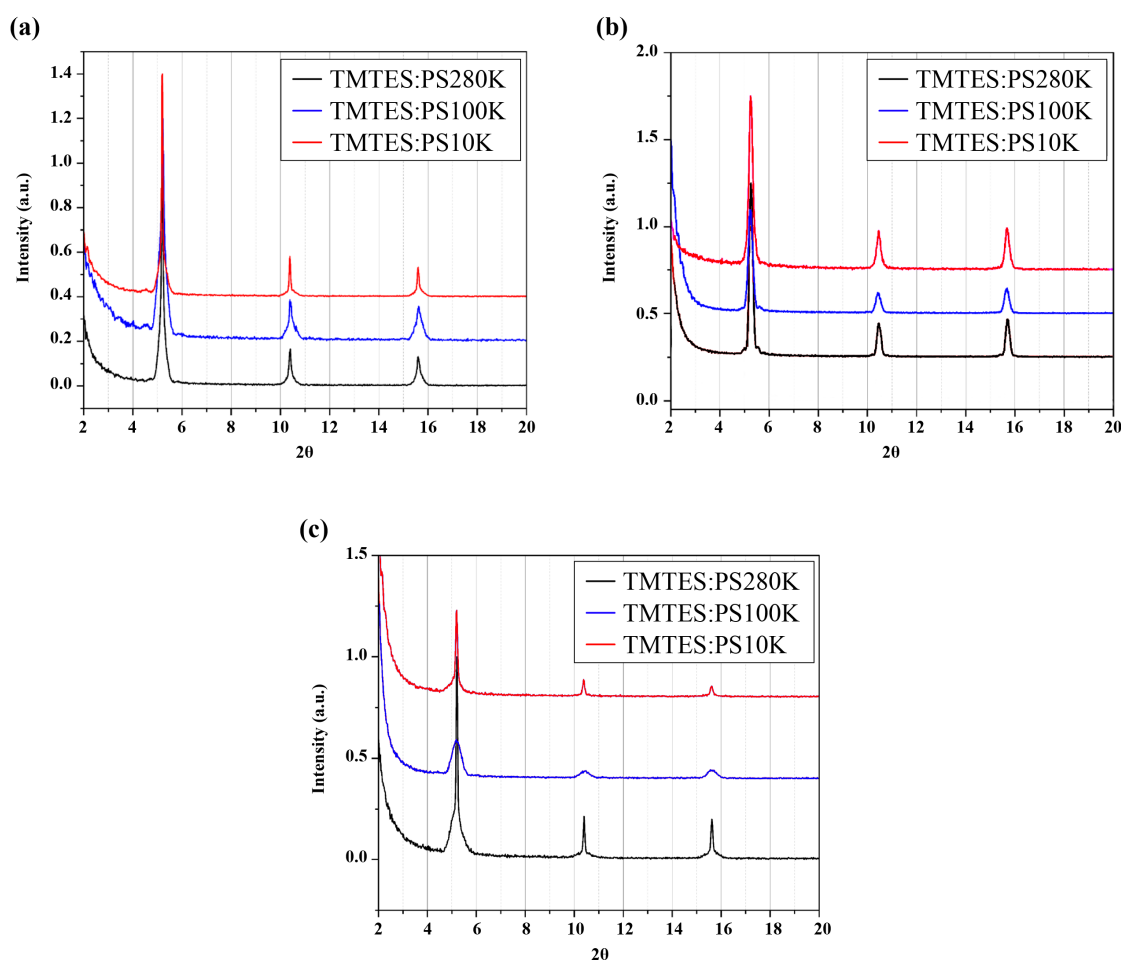


Figure 5.7 X-ray diffraction analysis of the films with all the volume ratios: (a) 4:1; (b) 2:1; (c) 1:2.

5.4 Electrical Characterization

In our study, related to the electrical behavior of OFETs, we explored the properties of devices under ambient conditions. Transfer and output characteristics of representative OFETs based on ratios 4:1, 2:1, and 1:2 are reported respectively in **Fig. 5.8**, **Fig. 5.9**, and **Fig. 5.10**. **Table 5.1**, **Table 5.2**, and **Table 5.3** collect the electrical parameters for all the devices based on ratios 4:1, 2:1, and 1:2 respectively.

We cannot directly compare the results obtained in this ongoing work (TMTES:PS_{280K}, ratio 1:2) with the results from the previous **Chapter 4**. This is primarily due to the fact that environmental factors, such as humidity, play a significant role in the fabrication process and can greatly influence the results.

The electrical characterization results of these studied devices reveal a correlation between the PS amount/PS molecular weight on device performance. For devices with a lower

concentration of PS (ratio 4:1), there is a marked performance improvement when the PS molecular weight is equal to 280,000 g/mol. A reduction in molecular weight is correlated with a decrease in the device's performance, indicating the critical role of molecular weight in the device's electrical properties.

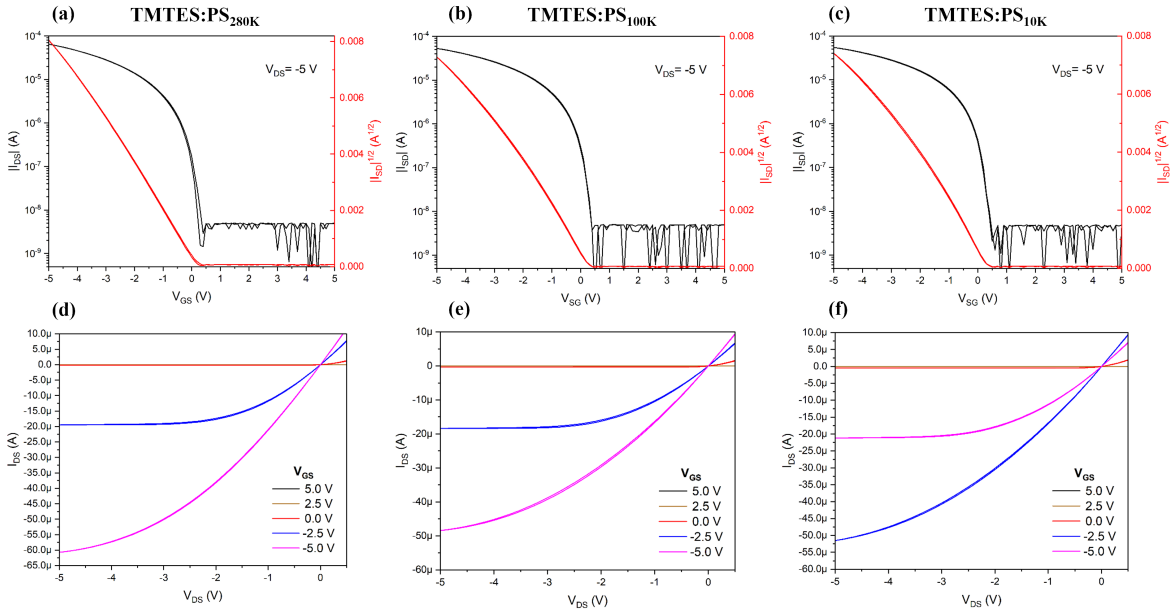


Figure 5.8 Electrical performance of the OFETs devices with solution combined in 4:1 volume ratio. Transfer characteristics in saturation regime of representative (a) TMTES:PS_{280K}, (b) TMTES:PS_{100K}, and (c) TMTES:PS_{10K} based OFETs. Output characteristics of representative (c) TMTES:PS_{280K}, (d) TMTES:PS_{100K}, and (e) TMTES:PS_{10K} based OFETs.

Table 5.1 Electrical parameters of OFETs based on films of TMTES:PS with a volume ratio equal to 4:1

Ink Formulation	Mobility ($\text{cm}^2 \text{V}^{-1} \text{s}^{-1}$)	V_{th} (V)	On/Off
TMTES:PS _{280K}	2.5 ± 0.2	0.37 ± 0.01	$1.2 \cdot 10^4$
TMTES:PS _{100K}	1.7 ± 0.3	0.50 ± 0.01	$1.0 \cdot 10^4$
TMTES:PS _{10K}	2.0 ± 0.2	0.55 ± 0.01	$1.1 \cdot 10^4$

Interestingly, this correlation is not linear and it exhibits a reverse trend when the PS concentration is increased, particularly in the ratios of 2:1 and, more notably, 1:2. In these scenarios, the PS molecular weight decrease enhances the electrical characteristics and charge mobility of the device. This suggests that an excessive presence of PS has a negative impact

on the device functionality. It is reasonable that a threshold exists beyond which PS acts as a passivating agent (as previously reported in **Chapter 4**), and PS does not interfere with the electrical transport properties of the semiconductor's charge carriers.

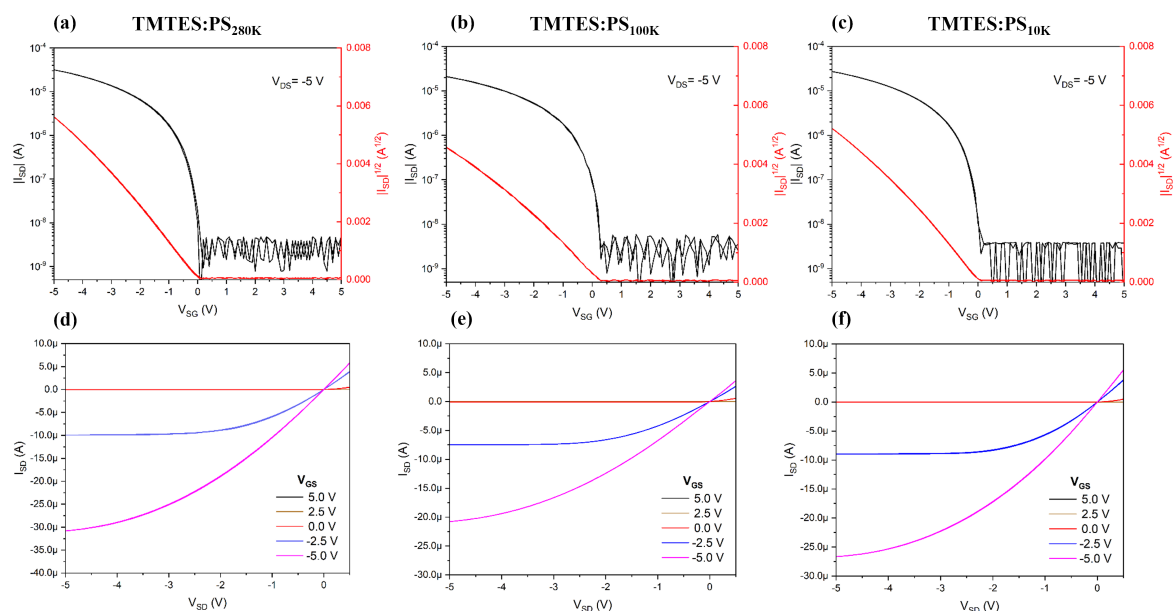


Figure 5.9 Electrical performance of the OFETs devices with solution combined in 2:1 volume ratio. Transfer characteristics in saturation regime of representative (a) TMTES:PS_{280K}, (b) TMTES:PS_{100K}, and (c) TMTES:PS_{10K} based OFETs. Output characteristics of representative (d) TMTES:PS_{280K}, (e) TMTES:PS_{100K}, and (f) TMTES:PS_{10K} based OFETs.

Table 5.2 collects the electrical parameters extracted for all the devices with a volume ratio equal to 2:1.

Table 5.2 Electrical parameters of OFETs based on films of TMTES:PS with a volume ratio equal to 2:1

Ink Formulation	Mobility ($\text{cm}^2 \text{V}^{-1} \text{s}^{-1}$)	V_{th} (V)	On/Off
TMTES:PS _{280K}	0.8 ± 0.3	0.10 ± 0.02	$5.0 \cdot 10^3$
TMTES:PS _{100K}	0.8 ± 0.2	0.33 ± 0.02	$6.0 \cdot 10^3$
TMTES:PS _{10K}	1.0 ± 0.2	0.37 ± 0.02	$8.0 \cdot 10^3$

This observation is aligned with the trend showing that when PS molecular weight is lower, PS is more fragmented within the semiconductor matrix because chain lengths are shorter; nevertheless, this does not block the charge mobility, leading to higher mobility

values. These data highlight the complex interaction between the quantity and molecular structure of PS within semiconductor devices; higher material amount and molecular size can inversely affect the electronic properties. Further research related to the threshold and the interaction mechanisms between PS and charge carriers could open new perspectives to optimize the composition of semiconductor materials and enhance the device's performance.

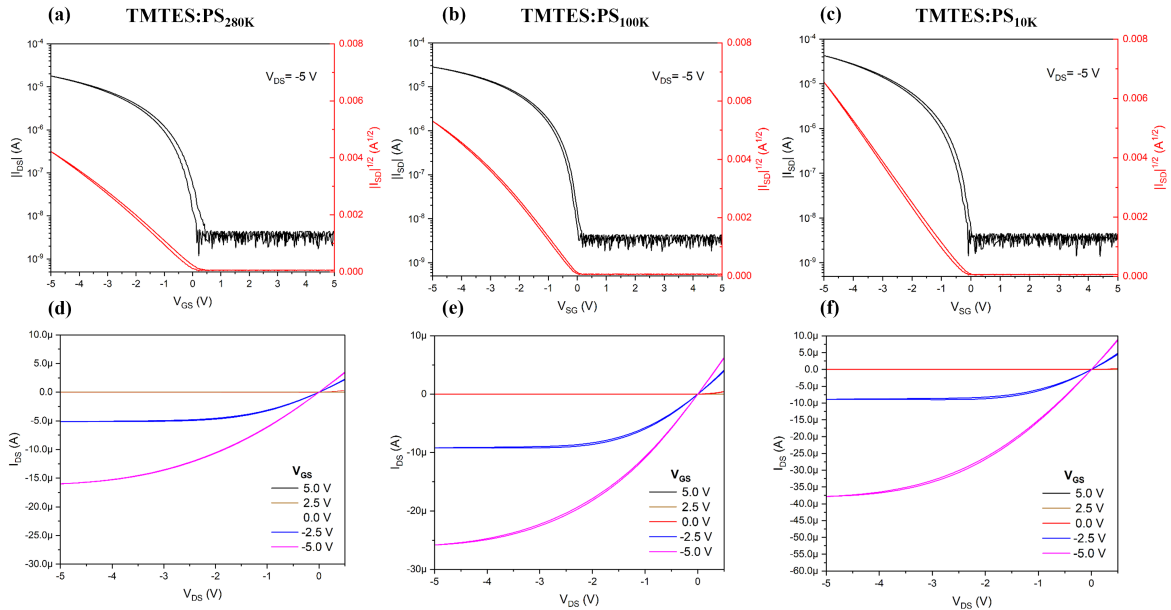


Figure 5.10 Electrical performance of the OFETs devices with solution combined in 1:2 volume ratio. Transfer characteristics in saturation regime of representative (a) TMTES:PS_{280K}, (b) TMTES:PS_{100K}, and (c) TMTES:PS_{10K} based OFETs. Output characteristics of representative (c) TMTES:PS_{280K}, (d) TMTES:PS_{100K}, and (e) TMTES:PS_{10K} based OFETs.

Table 5.3 collects the electrical parameters extracted for all the devices with a volume ratio equal to 1:2.

Table 5.3 Electrical parameters of OFETs based on films of TMTES:PS with a volume ratio equal to 1:2

Ink Formulation	Mobility ($\text{cm}^2 \text{V}^{-1} \text{s}^{-1}$)	V_{th} (V)	On/Off
TMTES:PS _{280K}	0.7 ± 0.2	0.13 ± 0.01	$5.3 \cdot 10^3$
TMTES:PS _{100K}	1.4 ± 0.2	0.14 ± 0.01	$7.8 \cdot 10^3$
TMTES:PS _{10K}	1.9 ± 0.2	0.11 ± 0.01	$1.1 \cdot 10^4$

Our investigation has discovered that the interaction between PS concentration and PS molecular weight critically determines the mobility of charge carriers within the semiconductor matrix. For blends with a lower proportion of PS, particularly with a 4:1 semiconductor-to-PS ratio, an enhanced device performance is observed when the molecular weight of PS is at 280,000 g/mol. This can be attributed to the longer PS chains forming a more efficient passivation layer over the semiconductor surface. The extended chains have a low capacity to blend into the semiconductor matrix, maintaining a distinct interface that can passivate the charge carriers effectively.

On the other side, PS chains of lower molecular weights such as 100,000 g/mol or 10,000 g/mol, tend to combine easily with the semiconductor matrix due to their shorter length. This determines a less distinct passivation layer, which could adversely affect the mobility of charge carriers due to the presence of trapping centers.

When the concentration of PS in the blend is increased, particularly in ratios of 2:1 and 1:2, the situation changes significantly. In these cases, a higher PS content inherently creates a more substantial passivation layer. However, longer PS chains at these higher concentrations are likely to phase-separate due to their bulkiness, leading to the formation of PS-rich domains [161]. These domains could act as traps for majority charge carriers, thus negatively impacting the charge mobility within the device.

Conversely, shorter PS chains, have an increased tendency to blend with the semiconductor, avoiding the formation of PS-rich domains which can act as majority charge traps. Therefore, at higher PS concentrations, shorter chains contribute to a more homogeneous TMTES:PS blend. This homogeneity is advantageous as it prevents the formation of large, discrete PS domains that can block charge transport. Thus, the blend with a lower molecular weight PS enhances the charge mobility by minimizing the disruptive PS accumulations [161].

Our results suggest that low PS content and higher molecular weight of PS are useful to form a distinct passivation layer that does not interfere with the semiconductor's charge carrier mobility. However, as the PS content increases, lower molecular weights PS are favored since they integrate more uniformly into the blend, avoiding the formation of charge-trapping PS accumulations and thereby maintaining or enhancing the mobility of the device.

This understanding of the interaction between PS concentration and PS molecular weight has significant implications for the design and optimization of TMTES:PS blends. It underlines the importance of tailoring the concentration of the polymer to achieve the desired balance between passivation and homogeneity, to optimize the charge transport properties of semiconductor devices.

In addition, bias stress measurements under ambient conditions for ratios 4:1, 2:1, and 1:2 are shown in **Fig. 5.11**, **Fig. 5.12**, and **Fig. 5.13** respectively. The interplay between the PS concentration and PS molecular weight within the semiconductor matrix has proven to be a critical factor of both initial charge mobility and long-term stability under bias stress.

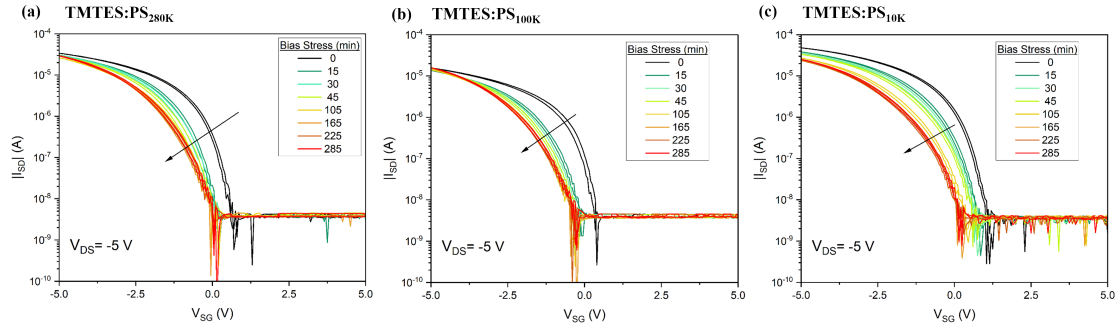


Figure 5.11 Bias-stress of the OFETs devices with solution combined in 4:1 volume ratio. Transfer characteristics in saturation regime of representative (a) TMTES:PS_{280K}, (b) TMTES:PS_{100K}, and (c) TMTES:PS_{10K} based OFETs.

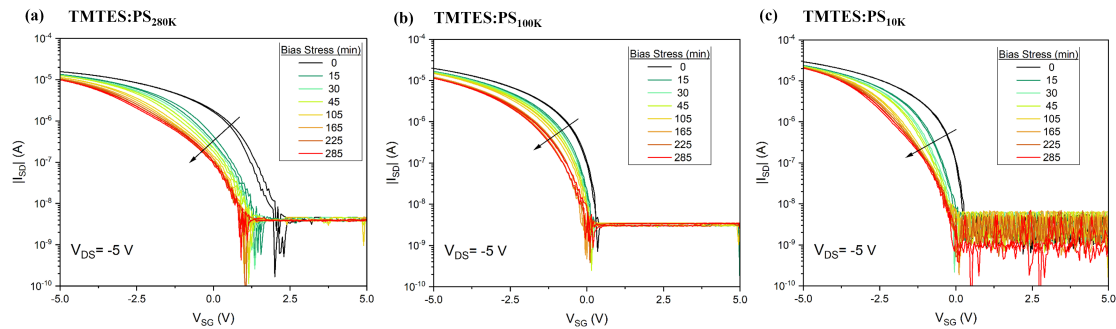


Figure 5.12 Bias-stress of the OFETs devices with solution combined in 2:1 volume ratio. Transfer characteristics in saturation regime of representative (a) TMTES:PS_{280K}, (b) TMTES:PS_{100K}, and (c) TMTES:PS_{10K} based OFETs.

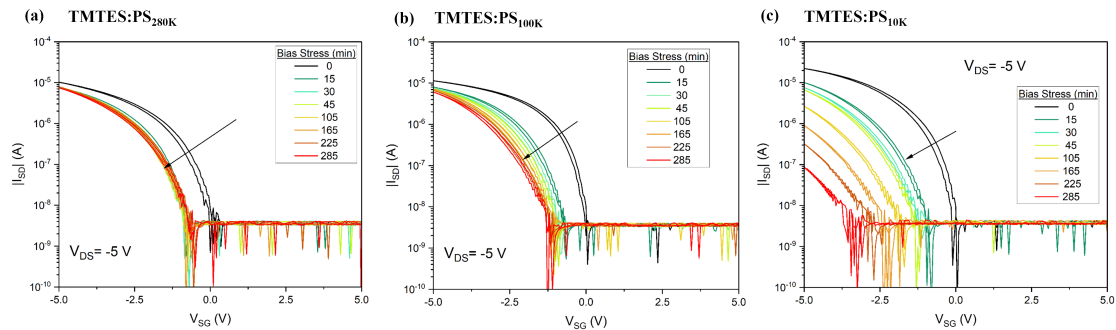


Figure 5.13 Bias-stress of the OFETs devices with solution combined in 1:2 volume ratio. Transfer characteristics in saturation regime of representative (a) TMTES:PS_{280K}, (b) TMTES:PS_{100K}, and (c) TMTES:PS_{10K} based OFETs.

OFETs devices with the ratio of 1:2 show a decrease in the molecular weight of PS leading to enhanced initial charge mobility. This is most likely due to the better uniform blending of shorter PS chains with the semiconductor, facilitating a smoother pathway for charge transport. However, when subjected to bias stress, an inverse trend is evident. Shorter PS chains (**Fig. 5.13c**), while beneficial for charge mobility under short-term operating conditions, may determine a greater vulnerability of the device over prolonged periods of bias. This increased susceptibility can be attributed to the fact that lower molecular weight PS chains may realize a passivation layer on the semiconductor surface less effective than one obtained with higher molecular weight PS; this could let the device degradation under long-term operating conditions. Indeed, higher molecular weight PS, ensured a long stability period due to an enhanced continuity of the PS-rich bottom layer in the vertically phase-separated films [161]. Thus, while facilitating greater initial charge mobility, shorter PS chains might also lead to worse performance over time.

It is noteworthy to mention that for OFETs devices with ratios of 4:1 and 2:1 (**Fig. 5.11**, **Fig. 5.12**), the bias stress performance remains stable across all molecular weights tested. This indicates that the bias stress is not significantly impacted by the PS molecular weight. This stability is indicative of an optimal balance between the PS passivation layer and the semiconductor interface, which appears to be less sensitive to the variations in PS molecular weight. The stability across different molecular weights for the 4:1 and 2:1 ratios could be due to a more robust passivation effect at these concentrations, which protects the semiconductor from bias-induced degradation. It seems that the passivation layer formed by the PS, regardless of its molecular weight, is sufficient to stabilize the interface and to prevent the formation of deep trap states that can significantly affect the OFETs's performance over time.

5.5 Chemical Characterization

Chemical TOF-SIMS maps of the TMTES:PS film were conducted to know the composition and the spatial distribution of compounds within the OFETs devices (**Fig. 5.14**). There is a decrease in homogeneity as the PS amount in the film increases. This trend is aligned with earlier observations, including those made using polarized optical microscopy, which also indicated that the most homogeneous film corresponds to the 4:1 TMTES:PS ratio.

The increased homogeneity in the 4:1 ratio film suggests a more uniform distribution of PS within the semiconductor matrix, which is a desirable characteristic for efficient charge transport and overall device performance. Conversely, as the PS concentration increases, the resulting film appears less homogeneous. This lack of uniformity can lead to the formation

of defects within the semiconductor layer, potentially creating barriers or traps for charge carriers, thereby adversely affecting the mobility of the device. To further support these results, AFM analysis will be performed.

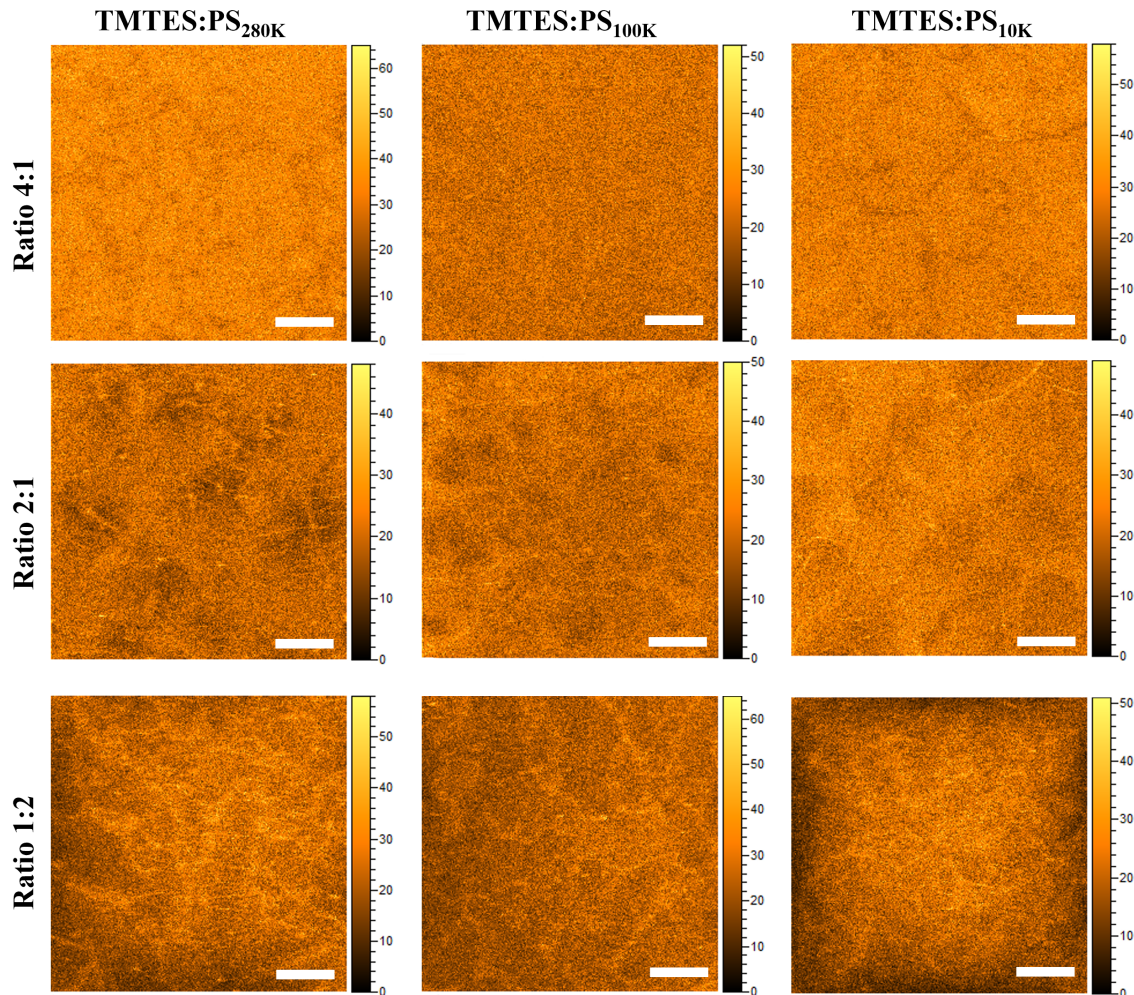


Figure 5.14 TOF-SIMS 2D surface chemical maps of TMTES:PS thin films deposited by BAMS at coating speed of 10 mm/s. Totally secondary ion signals from TMTES:PS surface acquired outside the interdigitated electrodes. Scale bar 20 μm

To study the vertical distribution of the insulating polymer, TOF-SIMS depth profiling was conducted on the TMTES:PS film (**Fig. 5.15**). Three representative profiles were taken, corresponding to TMTES, PS, and SiO_2 substrate, by averaging the signal intensities of characteristic secondary ions from each stratified material in the OFETs channel area. Analysis, of the characteristic fragments from TMTES and PS, confirmed the simultaneous presence of the OSCs and of the polymer. Progressing deeper into the film towards the substrate, the PS ion signals diverged from those of the OSCs, delineating a well-defined

TMTES-PS transition region. Here, the TMTES signal reduced significantly, whereas the PS signal increased. These results, consistent with our previous studies (Section 4.5), confirm that PS serves as a dielectric passivating layer.

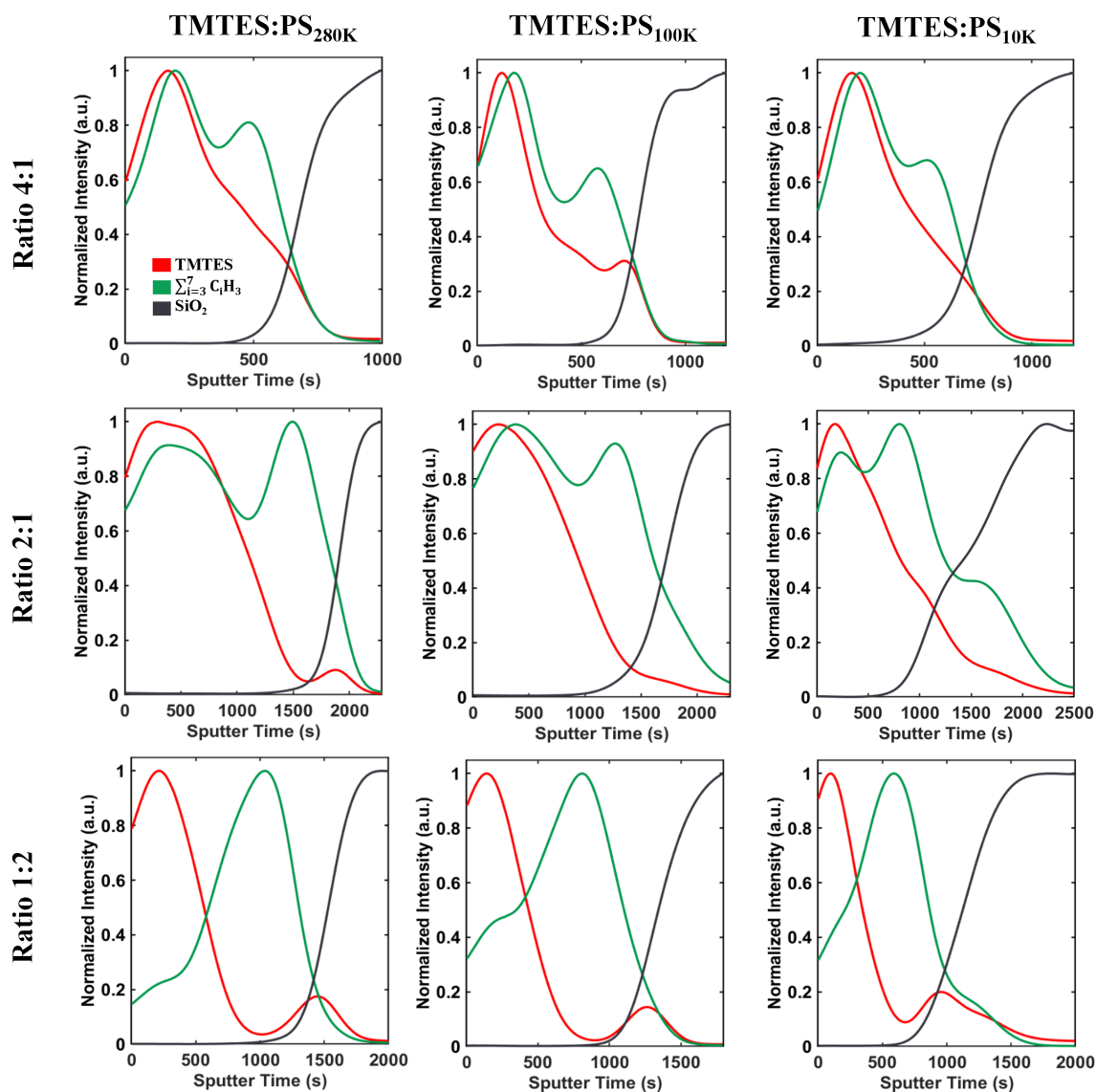


Figure 5.15 TOF-SIMS study of the TMTES:PS thin films. Normalized (to maximum) TOF-SIMS depth profile acquired in the channel area of the OFET starting from the surface and reaching the SiO₂ substrate (black curve). The TMTES signal (red curve) includes the SiC⁻, SiCH⁻, SiC₂H⁻, SiC₅H₂⁻, SiC₇H₂⁻ species; the PS signal (green curve) includes the C₃H₃⁻, C₄H₃⁻, C₅H₃⁻, C₆H₃⁻, C₇H₃⁻ species.

However, it's important to note that TOF-SIMS, while providing valuable insights into the distribution of components, is limited to providing precise quantitative analysis, due to the matrix effects (Section 2.2.3), especially in this context where the ratio of TMTES to PS

varies across samples. This variability affects the possibility to compare directly different samples, although comparisons within the same ratio with different molecular weights remain valid.

For the 4:1 TMTES:PS ratio, TOF-SIMS analysis revealed a clear phenomenon of PS segregation across all molecular weights, with the effect being slightly less pronounced at 10,000 g/mol. This result is aligned with the earlier observation of lower mobility at this molecular weight, suggesting a correlation between the segregation layer and the charge carrier mobility.

In the 2:1 ratio, the TOF-SIMS profiles indicated the presence of PS segregation, but no significant differences were observed across the different molecular weights.

The analysis of the 1:2 seems to exhibit the most pronounced phase segregation. A deeper evaluation shows that this conclusion is not completely accurate: the heightened intensity in the green signal, which was thought to be solely indicative of PS, in reality was due to a combination of signals from both PS and TMTES, and because the $\sum_{i=3}^7 C_i H_3$ fragmentations could be obtained both from TMTES and PS. In the 1:2 ratio, there is a higher concentration of PS compared to TMTES, resulting in a more intense signal in the segregated area where the intensity depends only on the PS contribution. Therefore, the apparent enhanced segregation is a direct consequence of the higher presence of PS in these samples in comparison with the TMTES semiconductor.

In conclusion, the chemical characterization reveals that phase segregation is a consistent phenomenon across all samples studied, indicating the presence of a passivation layer at the interface in the OFETs devices. Due to the technical limitations of this technique, we can state, with a good/high degree of confidence, that phase segregation occurs and impacts on interface passivation, while it is not yet completely clear how this segregation varies when ratios and molecular weights are modified.

To verify the effective passivation of the semiconductor/dielectric interface, the number of interfacial trap states was calculated. The interfacial trap density for the majority charge carriers (i.e., holes) per unit area (N_T) was extracted directly to Subthreshold Swing (SS), and has been estimated using the mentioned equations: **Eq. (1.15)** and **Eq. (1.16)**.

The results clearly show that the addition of PS leads to a consistent reduction in trap density, confirming the passivation effect (**Fig. 5.16**). This reduction is significant and comparable across various TMTES:PS ratios (and PS molecular weights) thereby demonstrating that the segregated PS effectively passivates the interface in all the samples confirming TOF-SIMS study: there aren't substantial differences between the different conditions presented.

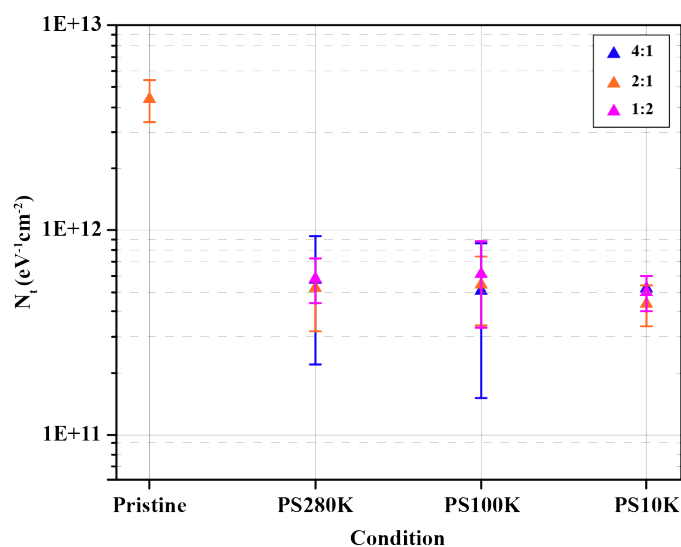


Figure 5.16 Interfacial trap states density for different TMTES:PS ratios and PS molecular weights.

5.6 X-ray Detection

Finally, X-ray measurements were conducted on the samples obtained by employing the above-mentioned ratios and molecular weights of PS. These devices were irradiated in the saturation regime with $V_{DS} = -2.5$ V and $V_{GS} = -10$ V. The sensitivity achieved for all devices is shown in **Fig. 5.17**, calculated using the methodologies outlined in **Section 4.6**.

It's important to note that X-ray detection was not possible for the devices with a semiconductor:PS ratio of 1:2 at 10,000 g/mol and 100,000 g/mol molecular weights. This absence of X-ray detection in these specific devices correlates with the bias stress performance observed in them, as reported in **Fig. 5.13**. This parallelism suggests that the film in these devices may not be enough stable to facilitate effective X-ray detection. The instability could arise from morphological inhomogeneity at the semiconductor interface, which is crucial for the efficient absorption and subsequent conversion of X-ray energy into an electrical signal.

The highest sensitivity achieved in our study was observed in the OFETs devices with a ratio of 4:1 at a molecular weight of 280,000 g/mol. This result is well aligned with the other results obtained in this study, notably the best mobility and a more homogeneous film structure as indicated by the TOF-SIMS surface analysis.

This combination of high sensitivity and excellent mobility demonstrates the significant potentiality of carefully engineered OFETs devices for advanced applications, particularly in fields requiring precise and efficient detection capabilities, such as X-ray imaging. The results emphasize the importance of fine-tuning material properties, such as the molecular

weight of polymer additives and their concentration within the semiconductor matrix, to achieve optimal device performance.

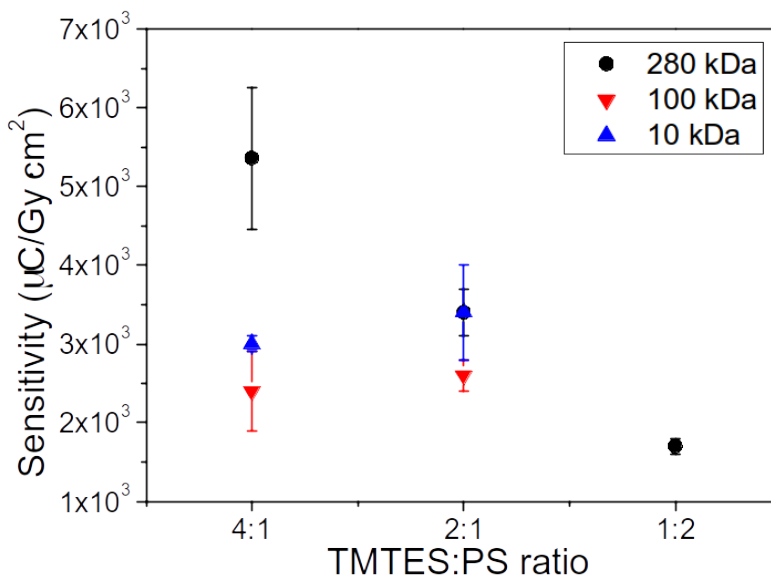


Figure 5.17 X-ray detection of TMTES:PS film-based device at different ratio and different PS molecular weight: 280,000 g/mol black marker, 100,000 g/mol red marker, and 10,000 g/mol blue marker.

5.7 Conclusions: PS Role for High X-Ray Sensitivity

In conclusion, our results underline the importance of a careful balance between molecular weight and concentration of PS within the semiconductor blend to achieve both high charge mobility, operational stability, and high X-ray sensitivity in OFETs devices. We have explored the properties and functionalities of TMTES:PS-based organic field-effect transistors across a range of TMTES:PS ratios (4:1, 2:1, and 1:2) and PS molecular weights (280,000 g/mol, 100,000 g/mol, and 10,000 g/mol).

Our study encompassed several key areas: film characterization, electrical characterization including bias stress analysis, chemical analysis, and a focused examination of X-ray detection capabilities, particularly relevant for potential medical applications.

Film and Electrical Characterization:

- The study revealed a consistent phase separation of PS at the semiconductor-dielectric interface in all samples, which served as an effective passivation layer, improving the charge mobility within the OFETs devices.
- Electrical performance results demonstrated that devices with a 4:1 TMTES:PS ratio exhibited the highest mobility. Following this, the 1:2 ratio samples at 100,000 and 10,000 g/mol also showed promising mobility levels.
- Significantly, the electrical characterization also involved bias stress tests, where the 1:2 ratio samples at 100,000 and 10,000 g/mol displayed suboptimal characteristics. This observation suggests potential limitations in their long-term stability and reliability in electronic applications.

X-ray Detection Analysis:

- The 4:1 ratio samples at 280,000 g/mol not only showed the best mobility but also the highest sensitivity to X-rays. This correlation highlighted the importance of achieving an optimal balance of material properties for effective X-ray detection.
- Interestingly, the devices that demonstrated poor bias stress performance (1:2 ratio at 100,000 and 10,000 g/mol) also failed to detect X-rays effectively. This result suggests that the factors contributing to bias stress susceptibility are potentially related to the structural and electronic integrity of the film, which also adversely impacts the device's ability to operate in X-ray detection applications.

In conclusion, this study of the TMTES:PS OFETs has revealed a relationship between material composition, electrical stability, and functional capabilities. The identification of an optimal blend that offers high charge mobility, bias stress resilience, and effective X-ray detection marks a significant step in developing OFETs for advanced medical applications. This research not only increases our understanding of organic electronics but also lays the base for innovative and reliable medical devices, particularly in diagnostic imaging.

Conclusions

The aim of this research was to enhance the performance of Organic Field-Effect Transistors (OFETs) in order to develop highly efficient devices. For this purpose, 1,4,8,11-Tetramethyl-6,13-triethylsilylethynylpentacene (TMTEs) and 2,7-dioctyl[1]benzothieno[3,2-b][1]benzothiophene (C_8 -BTBT- C_8) were blended with Polystyrene (PS): the materials chosen were strategic, and significant advancements in OFETs technology were achieved. The study, executed to enhance OFETs performance, particularly for applications in medical fields, has produced significant results regarding the role played by PS in the optimization of the device.

The innovative strategy of molecular contact doping, applied in this work, was the incorporation of a molecular contact dopant layer between the Organic Semiconductors (OSCs) and the top gold contacts. The position of the dopant layer crucially reduced the energy barriers associated with charge injection and release: the overall efficiency of OFETs was markedly boosted. It has to be underlined that the implementation of molecular contact doping presents several challenges, since, over time, the dopant tends to diffuse into the OFETs channel and an unintentional doping of the OSCs could occur. This diffusion process poses a significant threat to the device's functionality, particularly affecting the device's on/off switching capabilities.

To address this issue, our study explored several devices where PS was utilized as a diffusion-blocking agent. The introduction of PS with different molecular weights into the OFETs structure has been fundamental to inhibiting the diffusion of the dopant. Time-of-Flight Secondary Ion Mass Spectrometry (TOF-SIMS) studies provided critical insights into the surface and in-depth distribution of the dopant, further confirming the effectiveness of our approach. We have been able to demonstrate that in thin films of OSCs blends with high-molecular-weight PS, the dopant remains drastically confined to the contact areas, leading to an enhanced long-term stability and capability of the devices.

The results of this work represent a significant advancement in the field of OFETs. By successfully mitigating the dopant diffusion, we have opened up new paths for developing

more stable and efficient organic electronic devices. The molecular contact doping not only enhances the practical mobility of OFETs but also sets a milestone for future research and development of organic semiconductors. In addition, the obtained results suggest that the method of doping and the choice of dopant material are critical parameters that influence the performance and the stability of OFETs. The use of PS as a dopant-blocking layer offers a novel way to fine-tune these devices, potentially leading to more precise control of the electrical properties. This could pave the way for the development of OFETs with customizable performance characteristics, tailored for specific applications in flexible electronics, display technology, and beyond.

Furthermore, this research opens new possibilities for exploring other polymer materials as potential diffusion-blocking agents. The effectiveness of PS in this role encourages a broader investigation into polymers with varying properties, which could lead to the discovery of even more efficient materials for enhancing OFETs performance. This work stream could significantly contribute to the field of organic electronics, providing deeper understanding and novel solutions to the challenges faced in device fabrication and optimization.

In the second part of the study, we explored the fabrication and application of thin films made from TMTES and TMTES blended with PS, using Bar-Assisted Meniscus Shearing (BAMS), an advanced high-throughput printing technique. These thin films demonstrate a unique herringbone crystallization pattern, fostering two-dimensional electronic interactions. Notably, OFETs incorporating these blended films have higher performance when compared to those made from unblended OSCs, not only in terms of performance but also in stability. The TMTES:PS-based OFETs particularly excelled, showing almost zero threshold voltage, low operation voltage, and an impressive average mobility. The inclusion of PS significantly reduced the density of hole traps, most likely due to the vertical phase separation during crystallization, passivating effectively the dielectric surface.

A pioneering aspect of this research was the application of these OFETs devices as X-ray detectors. They exhibited extraordinary X-ray sensitivity, greater than the one shown by most of the perovskite film-based detectors. To illustrate the potentiality of the X-ray detector, we designed an array of four pixels to image a metallic object in an X-ray beamline, simulating a medical radiography scenario. This underscores the vast potential of using high-performance, cost-effective OFETs with human-tissue equivalent organic materials as active layers. Such devices promise revolutionary advancements in large-area, highly sensitive X-ray detectors, opening new horizons in medical dosimetry and diagnostic imaging applications.

In conclusion, it has become evident that the balance between the molecular weight and the PS concentration within the semiconductor blend is crucial for the optimization of OFETs. This balance is the key to ensuring high charge mobility, operational stability, and enhanced

X-ray sensitivity in OFETs devices. This investigation has spanned an extensive range of TMTES:PS ratios and PS molecular weights, examining their impact on OFETs performance and functionality.

Focusing on film characterization, we observed consistent phase separation of PS at the semiconductor-dielectric interface across all samples. This separation played a pivotal role in an effective passivation layer, which substantially improved the charge mobility within the OFETs devices. The achieved results were particularly important for the electrical performance understanding. Devices with a 4:1 TMTES:PS ratio showcased the highest mobility, a finding that underscores the importance of the materials proportion. We also explored bias stress analysis, revealing that the 1:2 ratio samples at 100,000 and 10,000 g/mol exhibited less optimal characteristics. This observation raises questions about the long-term stability and reliability, which are crucial for electronic applications.

Furthermore, this work extended into a detailed examination of X-ray detection capabilities, an area significantly relevant for medical applications. Here, we found that the 4:1 ratio samples at 280,000 g/mol not only excelled in mobility but also demonstrated the highest sensitivity to X-rays, highlighting the critical importance of optimal material balance for effective X-ray detection. Conversely, the samples that showed poor bias stress performance, specifically the 1:2 ratio samples at lower molecular weights, were less effective in detecting X-rays. This result suggests a potential link between the factors contributing to bias stress susceptibility and the structural and electronic integrity of the film, which in turn impacts the OFET's ability to function in X-ray detection applications.

In summary, the study of TMTES:PS-based OFETs has shown a relationship between material composition, electrical stability, and functional capabilities. Identifying the optimal blend that offers high charge mobility, bias stress resilience, and effective X-ray detection marks a significant advancement in the development of OFETs for advanced medical applications. This research not only enhances our understanding of organic electronics but also lays the groundwork for innovative and reliable medical devices, especially in the field of diagnostic imaging.

Bibliography

- [1] J. B. W. B. Shockley and W. H. Brattain. (1956) The nobel prize in physics 1956. Accessed: 2023-10-05. [Online]. Available: <https://www.nobelprize.org/prizes/physics/1956/summary/>
- [2] M. Tanenbaum, L. B. Valdes, E. Buehler, and N. B. Hannay, “Silicon n-p-n Grown Junction Transistors,” *Journal of Applied Physics*, vol. 26, no. 6, pp. 686–692, 05 2004. [Online]. Available: <https://doi.org/10.1063/1.1722071>
- [3] A. Kumar, S. Tripathi, M. Shkir, A. Alqahtani, and S. AlFaify, “Prospective and challenges for lead-free pure inorganic perovskite semiconductor materials in photovoltaic application: A comprehensive review,” *Applied Surface Science Advances*, vol. 18, p. 100495, 2023. [Online]. Available: <https://www.sciencedirect.com/science/article/pii/S2666523923001290>
- [4] T. Zhang, Z. Hou, R. Johnson, L. Del Castillo, A. Moussessian, R. Greenwell, and B. Blalock, “Flexible electronics: Thin silicon die on flexible substrates,” *Electronics Packaging Manufacturing, IEEE Transactions on*, vol. 32, pp. 291 – 300, 11 2009.
- [5] M. Müller, C. Kübel, and K. Müllen, “Giant polycyclic aromatic hydrocarbons,” *Chemistry – A European Journal*, vol. 4, no. 11, pp. 2099–2109, 1998. [Online]. Available: <https://chemistry-europe.onlinelibrary.wiley.com/doi/abs/10.1002/%28SICI%291521-3765%2819981102%294%3A11%3C2099%3A%3AAID-CHEM2099%3E3.0.CO%3B2-T>
- [6] P. Anderson, P. Lee, and M. Saitoh, “Remarks on giant conductivity in ttf-tcnq,” *Solid State Communications*, vol. 13, no. 5, pp. 595–598, 1973. [Online]. Available: <https://www.sciencedirect.com/science/article/pii/S0038109873800201>
- [7] H. Shirakawa, E. J. Louis, A. G. MacDiarmid, C. K. Chiang, and A. J. Heeger, “Synthesis of electrically conducting organic polymers: halogen derivatives of polyacetylene, (ch),” *J. Chem. Soc., Chem. Commun.*, pp. 578–580, 1977. [Online]. Available: <http://dx.doi.org/10.1039/C39770000578>
- [8] M. A. G. . S. H. Heeger A. J. (2000) Nobel prize in chemistry 2000. Accessed: 2023-10-07. [Online]. Available: <https://www.nobelprize.org/prizes/chemistry/2000/press-release/>
- [9] A. Salehi, X. Fu, D.-H. Shin, and F. So, “Recent advances in oled optical design,” *Advanced Functional Materials*, vol. 29, no. 15, p. 1808803, 2019. [Online]. Available: <https://onlinelibrary.wiley.com/doi/abs/10.1002/adfm.201808803>

- [10] H. Hoppe and N. S. Sariciftci, "Organic solar cells: An overview," *Journal of Materials Research*, vol. 19, no. 7, p. 1924–1945, 2004.
- [11] K. Liu, B. Ouyang, X. Guo, Y. Guo, and Y. Liu, "Advances in flexible organic field-effect transistors and their applications for flexible electronics," *npj Flexible Electronics*, vol. 6, 12 2022.
- [12] C. W. Tang and S. A. VanSlyke, "Organic electroluminescent diodes," *Applied Physics Letters*, vol. 51, no. 12, pp. 913–915, 09 1987. [Online]. Available: <https://doi.org/10.1063/1.98799>
- [13] B. Geffroy, P. le Roy, and C. Prat, "Organic light-emitting diode (oled) technology: materials, devices and display technologies," *Polymer International*, vol. 55, no. 6, pp. 572–582, 2006. [Online]. Available: <https://onlinelibrary.wiley.com/doi/abs/10.1002/pi.1974>
- [14] S. y. Lu, S. Mukhopadhyay, R. Froese, and P. Zimmerman, "Virtual screening of hole transport, electron transport, and host layers for effective oled design," *Journal of Chemical Information and Modeling*, vol. 58, 06 2018.
- [15] K. Ranabhat, L. Patrikeev, A. Revina, K. Andrianov, V. Lapshinsky, and E. Sofronova, "An introduction to solar cell technology," *Istrazivanja i projektovanja za privredu*, vol. 14, pp. 481–491, 01 2016.
- [16] L. Meng, Y. Zhang, X. Wan, C. Li, X. Zhang, Y. Wang, X. Ke, Z. Xiao, L. Ding, R. Xia, H.-L. Yip, Y. Cao, and Y. Chen, "Organic and solution-processed tandem solar cells with 17.3% efficiency," *Science*, vol. 361, no. 6407, pp. 1094–1098, 2018. [Online]. Available: <https://www.science.org/doi/abs/10.1126/science.aat2612>
- [17] A. Tsumura, H. Koezuka, and T. Ando, "Macromolecular electronic device: Field-effect transistor with a polythiophene thin film," *Applied Physics Letters*, vol. 49, no. 18, pp. 1210–1212, 11 1986. [Online]. Available: <https://doi.org/10.1063/1.97417>
- [18] L. Alcácer, *Electronic Structure of Organic Semiconductors*, ser. 2053-2571. Morgan & Claypool Publishers, 2018. [Online]. Available: <https://dx.doi.org/10.1088/2053-2571/aaddd8>
- [19] *Molecular Orbital Theory*. John Wiley & Sons, Ltd, 2010, ch. 1, pp. 1–67. [Online]. Available: <https://onlinelibrary.wiley.com/doi/abs/10.1002/9780470689493.ch1>
- [20] T. Clark and R. Koch, *Linear Combination of Atomic Orbitals*. Berlin, Heidelberg: Springer Berlin Heidelberg, 1999, pp. 5–22. [Online]. Available: https://doi.org/10.1007/978-3-662-13150-3_2
- [21] L. Pauling, "The nature of the chemical bond. application of results obtained from the quantum mechanics and from a theory of paramagnetic susceptibility to the structure of molecules," *Journal of the American Chemical Society*, vol. 53, no. 4, pp. 1367–1400, 1931. [Online]. Available: <https://doi.org/10.1021/ja01355a027>
- [22] M. Jafari, "Application of vibrational spectroscopy in organic electronics," Ph.D. dissertation, 11 2017.

- [23] K. Wijeratne, "Conducting polymer electrodes for thermogalvanic cells," Ph.D. dissertation, 12 2018.
- [24] M. Heydari Gharahcheshmeh and K. K. Gleason, "Recent progress in conjugated conducting and semiconducting polymers for energy devices," *Energies*, vol. 15, no. 10, 2022. [Online]. Available: <https://www.mdpi.com/1996-1073/15/10/3661>
- [25] A. Qin, J. W. Y. Lam, and B. Z. Tang, "Click polymerization," *Chem. Soc. Rev.*, vol. 39, pp. 2522–2544, 2010. [Online]. Available: <http://dx.doi.org/10.1039/B909064A>
- [26] C. Liu, K. Huang, W.-T. Park, M. Li, T. Yang, X. Liu, L. Liang, T. Minari, and Y.-Y. Noh, "A unified understanding of charge transport in organic semiconductors: the importance of attenuated delocalization for the carriers," *Mater. Horiz.*, vol. 4, pp. 608–618, 2017. [Online]. Available: <http://dx.doi.org/10.1039/C7MH00091J>
- [27] X. Chen, J. Guo, L. Peng, Q. Wang, S. Jiang, and Y. Li, "Charge transport in organic field-effect transistors," *Materials Today Electronics*, vol. 6, p. 100077, 2023. [Online]. Available: <https://www.sciencedirect.com/science/article/pii/S2772949423000530>
- [28] B. Movaghar, L. O. Jones, M. A. Ratner, G. C. Schatz, and K. L. Kohlstedt, "Are transport models able to predict charge carrier mobilities in organic semiconductors?" *The Journal of Physical Chemistry C*, vol. 123, no. 49, pp. 29 499–29 512, 2019. [Online]. Available: <https://doi.org/10.1021/acs.jpcc.9b06250>
- [29] N. F. Mott, "On the transition to metallic conduction in semiconductors," *Canadian Journal of Physics*, vol. 34, no. 12A, pp. 1356–1368, 1956. [Online]. Available: <https://doi.org/10.1139/p56-151>
- [30] E. M. Conwell, "Impurity band conduction in germanium and silicon," *Phys. Rev.*, vol. 103, pp. 51–61, Jul 1956. [Online]. Available: <https://link.aps.org/doi/10.1103/PhysRev.103.51>
- [31] A. Miller and E. Abrahams, "Impurity conduction at low concentrations," *Phys. Rev.*, vol. 120, pp. 745–755, Nov 1960. [Online]. Available: <https://link.aps.org/doi/10.1103/PhysRev.120.745>
- [32] T. Holstein, "Studies of polaron motion: Part i. the molecular-crystal model," *Annals of Physics*, vol. 8, no. 3, pp. 325–342, 1959. [Online]. Available: <https://www.sciencedirect.com/science/article/pii/0003491659900028>
- [33] S. Verlaak, V. Arkhipov, and P. Heremans, "Modeling of transport in polycrystalline organic semiconductor films," *Applied Physics Letters*, vol. 82, pp. 745–747, 02 2003.
- [34] G. Horowitz and M. E. Hajlaoui, "Mobility in polycrystalline oligothiophene field-effect transistors dependent on grain size," *Advanced Materials*, vol. 12, no. 14, pp. 1046–1050, 2000. [Online]. Available: <https://onlinelibrary.wiley.com/doi/abs/10.1002/1521-4095%28200007%2912%3A14%3C1046%3A%3AAID-ADMA1046%3E3.0.CO%3B2-W>

- [35] M. Goel, M. Siegert, G. Krauss, J. Mohanraj, A. Hochgesang, D. C. Heinrich, M. Fried, J. Pflaum, and M. Thelakkat, "Homo–homo electron transfer: An elegant strategy for p-type doping of polymer semiconductors toward thermoelectric applications," *Advanced Materials*, vol. 32, no. 43, p. 2003596, 2020. [Online]. Available: <https://onlinelibrary.wiley.com/doi/abs/10.1002/adma.202003596>
- [36] B. Shan and Q. Miao, "Molecular design of n-type organic semiconductors for high-performance thin film transistors," *Tetrahedron Letters*, vol. 58, no. 20, pp. 1903–1911, 2017. [Online]. Available: <https://www.sciencedirect.com/science/article/pii/S0040403917304549>
- [37] H. Sirringhaus, "25th anniversary article: Organic field-effect transistors: The path beyond amorphous silicon," *Advanced Materials*, vol. 26, no. 9, pp. 1319–1335, 2014. [Online]. Available: <https://onlinelibrary.wiley.com/doi/abs/10.1002/adma.201304346>
- [38] M. Mas-Torrent and C. Rovira, "Cheminform abstract: Novel small molecules for organic field-effect transistors: Towards processability and high performance," *Chemical Society reviews*, vol. 37, pp. 827–38, 05 2008.
- [39] H. Sirringhaus, P. Brown, R. Friend, M. Nielsen, K. Bechgaard, B. Langeveld-Voss, A. Spiering, R. Janssen, E. Meijer, P. Herwig, and D. Leeuw, "Two-dimensional charge transport in self-organized, high-mobility conjugated polymers," *Nature*, vol. 401, 10 1999.
- [40] I. McCulloch, M. Heeney, C. Bailey, K. Genevicius, I. MacDonald, M. Shkunov, D. Sparrowe, S. Tierney, R. Wagner, W. Zhang, M. Chabinyc, R. Kline, M. McGehee, and M. Toney, "Liquid-crystalline semiconducting polymers with high charge-carrier mobility," *Nature materials*, vol. 5, pp. 328–33, 05 2006.
- [41] H. Tsao, D. Cho, I. Park, M. R. Hansen, A. Mavrinskiy, D. Yoon, R. Graf, W. Pisula, H. Spiess, and K. Müllen, "Ultrahigh mobility in polymer field-effect transistors by design," *Journal of the American Chemical Society*, vol. 133, pp. 2605–12, 02 2011.
- [42] B. Stuhmann, "Self-organized active biopolymer networks in migrating living cells," Ph.D. dissertation, 08 2009.
- [43] Y. Diao, L. Shaw, Z. Bao, and S. Mannsfeld, "Morphology control strategies for solution-processed organic semiconductor thin films," *Energy & Environmental Science*, vol. 7, pp. 2145–2159, 07 2014.
- [44] F. G. del Pozo, S. Fabiano, R. Pfattner, S. Georgakopoulos, S. Galindo, X. Liu, S. Braun, M. Fahlman, J. Veciana, C. Rovira, X. Crispin, M. Berggren, and M. Mas-Torrent, "Single crystal-like performance in solution-coated thin-film organic field-effect transistors," *Advanced Functional Materials*, vol. 26, no. 14, pp. 2379–2386, 2016. [Online]. Available: <https://onlinelibrary.wiley.com/doi/abs/10.1002/adfm.201502274>
- [45] S.-J. Wang, M. Sawatzki, G. Darbandy, F. Tahnack, J. Vahland, M. Malfois, A. Kloes, S. Mannsfeld, H. Kleemann, and K. Leo, "Organic bipolar transistors," *Nature*, vol. 606, pp. 700–705, 06 2022.

- [46] G. Parthasarathy, C. Shen, A. Kahn, and S. R. Forrest, "Lithium doping of semiconducting organic charge transport materials," *Journal of Applied Physics*, vol. 89, no. 9, pp. 4986–4992, 05 2001. [Online]. Available: <https://doi.org/10.1063/1.1359161>
- [47] T. H. Kim, J. H. Kim, and K. Kang, "Molecular doping principles in organic electronics: fundamentals and recent progress," *Japanese Journal of Applied Physics*, vol. 62, no. SE, p. SE0803, mar 2023. [Online]. Available: <https://dx.doi.org/10.35848/1347-4065/acbb10>
- [48] A. D. Scaccabarozzi, A. Basu, F. Aniés, J. Liu, O. Zapata-Arteaga, R. Warren, Y. Firdaus, M. I. Nugraha, Y. Lin, M. Campoy-Quiles, N. Koch, C. Müller, L. Tsetseris, M. Heeney, and T. D. Anthopoulos, "Doping approaches for organic semiconductors," *Chemical Reviews*, vol. 122, no. 4, pp. 4420–4492, 2022, pMID: 34793134. [Online]. Available: <https://doi.org/10.1021/acs.chemrev.1c00581>
- [49] C. Kittel, *Introduction to solid state physics*. John Wiley & sons, inc, 2005.
- [50] H. Hase, J. T. Liu, P. Forgione, and I. Salzmann, "Formation of ion pairs and charge-transfer complexes in the p-doping of organic semiconductors," *ECS Meeting Abstracts*, vol. MA2020-01, no. 8, p. 760, may 2020. [Online]. Available: <https://dx.doi.org/10.1149/MA2020-018760mtgabs>
- [51] H. Méndez, G. Heimel, A. Opitz, K. Sauer, P. Barkowski, M. Oehzelt, J. Soeda, T. Okamoto, J. Takeya, J.-B. Arlin, J.-Y. Balandier, Y. Geerts, N. Koch, and I. Salzmann, "Doping of organic semiconductors: Impact of dopant strength and electronic coupling," *Angewandte Chemie International Edition*, vol. 52, no. 30, pp. 7751–7755, 2013. [Online]. Available: <https://onlinelibrary.wiley.com/doi/abs/10.1002/anie.201302396>
- [52] H. Yan and W. Ma, "Molecular doping efficiency in organic semiconductors: Fundamental principle and promotion strategy," *Advanced Functional Materials*, vol. 32, p. 2111351, 12 2021.
- [53] N. Jung, N. Kim, S. Jockusch, N. Turro, P. Kim, and L. Brus, "Charge transfer chemical doping of few layer graphenes: Charge distribution and band gap formation," *Nano letters*, vol. 9, pp. 4133–7, 10 2009.
- [54] D. Kiefer, R. Kroon, A. Hofmann, H. Sun, X. Liu, A. Giovannitti, D. Stegerer, A. Cano, J. Hynynen, L. Yu, Y. Zhang, D. Nai, T. Harrelson, M. Sommer, A. Moulé, M. Kemerink, S. Marder, I. McCulloch, M. Fahlman, and C. Müller, "Double doping of conjugated polymers with monomer molecular dopants," *Nature Materials*, vol. 18, 02 2019.
- [55] T. Menke, D. Ray, H. Kleemann, K. Leo, and M. Riede, "Determining doping efficiency and mobility from conductivity and seebeck data of n-doped c60 layers," *physica status solidi (b)*, vol. 252, no. 8, pp. 1877–1883, 2015. [Online]. Available: <https://onlinelibrary.wiley.com/doi/abs/10.1002/pssb.201552088>
- [56] C. Chan and A. Kahn, "N-doping of pentacene by decamethylcobaltocene," *Applied Physics A*, vol. 95, pp. 7–13, 2009. [Online]. Available: <https://api.semanticscholar.org/CorpusID:8871114>

- [57] H. Yan, Z. Chen, Y. Zheng, C. Newman, J. Quinn, F. Dötz, M. Kastler, and A. Facchetti, “A high-mobility electron-transporting polymer for printed transistors,” *Nature*, vol. 457, pp. 679–86, 02 2009.
- [58] Y. Qi, S. Mohapatra, S. Kim, S. Barlow, S. Marder, and A. Kahn, “Solution doping of organic semiconductors using air-stable n-dopants,” *APL: Organic Electronics and Photonics*, vol. 5, 02 2012.
- [59] B. Wegner, L. Grubert, C. Dennis, A. Opitz, A. Röttger, Y. Zhang, S. Barlow, S. R. Marder, S. Hecht, K. Müllen, and N. Koch, “Predicting the yield of ion pair formation in molecular electrical doping: redox-potentials versus ionization energy/electron affinity,” *J. Mater. Chem. C*, vol. 7, pp. 13 839–13 848, 2019. [Online]. Available: <http://dx.doi.org/10.1039/C9TC04500G>
- [60] I. Kymissis, *Organic Field Effect Transistors: Theory, Fabrication and Characterization*, ser. Integrated Circuits and Systems. Springer US, 2008. [Online]. Available: https://books.google.be/books?id=GD_ry6FtSEQC
- [61] L. Mariucci, M. Rapisarda, A. Valletta, and G. Fortunato, *Contact Effects in Organic Thin-Film Transistors: Device Physics and Modeling*. Cham: Springer International Publishing, 2016, pp. 945–969. [Online]. Available: https://doi.org/10.1007/978-3-319-14346-0_176
- [62] R. Pfattner, C. Rovira, and M. Mas-Torrent, “Organic metal engineering for enhanced field-effect transistor performance,” *Phys. Chem. Chem. Phys.*, vol. 17, pp. 26 545–26 552, 2015. [Online]. Available: <http://dx.doi.org/10.1039/C4CP03492A>
- [63] M.-T. Liu, C.-Y. Chi, M. Zharnikov, and Y. Tai, “Selective and non-selective modification of electrodes in organic thin film transistors by self-assembled monolayers,” *Journal of Materials Chemistry C*, vol. 11, 01 2023.
- [64] D. Bharti and S. P. Tiwari, “Crystallinity and performance improvement in solution processed organic field-effect transistors due to structural dissimilarity of the additive solvent,” *Synthetic Metals*, vol. 215, pp. 1–6, 2016. [Online]. Available: <https://www.sciencedirect.com/science/article/pii/S0379677916300133>
- [65] G. Horowitz, “Organic field-effect transistors,” *Advanced Materials*, vol. 10, no. 5, pp. 365–377, 1998. [Online]. Available: <https://onlinelibrary.wiley.com/doi/abs/10.1002/%28SICI%291521-4095%28199803%2910%3A5%3C365%3A%3AAID-ADMA365%3E3.0.CO%3B2-U>
- [66] T. Someya, A. Dodabalapur, J. Huang, K. C. See, and H. E. Katz, “Chemical and physical sensing by organic field-effect transistors and related devices,” *Advanced Materials*, vol. 22, no. 34, pp. 3799–3811, 2010. [Online]. Available: <https://onlinelibrary.wiley.com/doi/abs/10.1002/adma.200902760>
- [67] W. Tang, Y. Fu, Y. Huang, Y. Li, Y. Song, X. Xi, Y. Yu, Y. Su, F. Yan, and X. Guo, “Solution processed low power organic field-effect transistor bio-chemical sensor of high transconductance efficiency,” *npj Flexible Electronics*, vol. 6, p. 18, 03 2022.

- [68] K. Manoli, M. Magliulo, Y. Mulla, M. Singh, L. Sabbatini, G. Palazzo, and L. Torsi, "Printable bioelectronics to investigate functional biological interfaces," *Angewandte Chemie (International ed. in English)*, vol. 54, 09 2015.
- [69] W. Shi, X. Yu, Y. Zheng, and J. Yu, "Dna based chemical sensor for the detection of nitrogen dioxide enabled by organic field-effect transistor," *Sensors and Actuators B: Chemical*, vol. 222, pp. 1003–1011, 2016. [Online]. Available: <https://www.sciencedirect.com/science/article/pii/S0925400515303476>
- [70] W. Huang, K. Besar, R. LeCover, P. Dullloor, J. Sinha, J. F. Martínez Hardigree, C. Pick, J. Swavola, A. D. Everett, J. Frechette, M. Bevan, and H. E. Katz, "Label-free brain injury biomarker detection based on highly sensitive large area organic thin film transistor with hybrid coupling layer," *Chem. Sci.*, vol. 5, pp. 416–426, 2014. [Online]. Available: <http://dx.doi.org/10.1039/C3SC52638K>
- [71] C. Li, H. Wu, T. Zhang, Y. Liang, B. Zheng, J. Xia, J. Xu, and Q. Miao, "Functionalized π stacks of hexabenzoperylenes as a platform for chemical and biological sensing," *Chem*, vol. 4, no. 6, pp. 1416–1426, 2018. [Online]. Available: <https://www.sciencedirect.com/science/article/pii/S2451929418301207>
- [72] M. Magliulo, D. De Tullio, I. Vikholm-Lundin, M. Albers, T. Munter, K. Manoli, G. Palazzo, and L. Torsi, "Label-free c-reactive protein electronic detection with an electrolyte-gated organic field-effect transistor-based immunosensor," *Analytical and Bioanalytical Chemistry*, vol. 408, 03 2016.
- [73] E. Baglini, A. Loi, L. Basiricò, P. Cosseddu, S. Lai, M. Barbaro, A. Bonfiglio, P. Maiolino, S. Denei, F. Mastrogiovanni, and G. Cannata, "Organic bendable and stretchable field effect devices for sensing applications," *IEEE Sensors Journal*, vol. 13, pp. 4764–4772, 12 2013.
- [74] S. Lai, P. Cosseddu, A. Bonfiglio, and M. Barbaro, "Ultralow voltage pressure sensors based on organic fets and compressible capacitors," *IEEE Electron Device Letters*, vol. 34, pp. 801–803, 06 2013.
- [75] S. Yuvaraja, A. Nawaz, Q. Liu, D. Dubal, S. G. Surya, K. N. Salama, and P. Sonar, "Organic field-effect transistor-based flexible sensors," *Chem. Soc. Rev.*, vol. 49, pp. 3423–3460, 2020. [Online]. Available: <http://dx.doi.org/10.1039/C9CS00811J>
- [76] Q. Zhang, F. Leonardi, R. Pfattner, and M. Mas-Torrent, "A solid-state aqueous electrolyte-gated field-effect transistor as a low-voltage operation pressure-sensitive platform," *Advanced Materials Interfaces*, vol. 6, no. 16, p. 1900719, 2019. [Online]. Available: <https://onlinelibrary.wiley.com/doi/abs/10.1002/admi.201900719>
- [77] Y. H. Lee, M. Jang, M. Y. Lee, O. Y. Kweon, and J. H. Oh, "Flexible field-effect transistor-type sensors based on conjugated molecules," *Chem*, vol. 3, no. 5, pp. 724–763, 2017. [Online]. Available: <https://www.sciencedirect.com/science/article/pii/S2451929417304333>
- [78] G. Darlinski, U. Böttger, R. Waser, H. Klauk, M. Halik, U. Zschieschang, G. Schmid, and C. Dehm, "Mechanical force sensors using organic thin-film transistors," *Journal of Applied Physics*, vol. 97, no. 9, p. 093708, 04 2005. [Online]. Available: <https://doi.org/10.1063/1.1888046>

- [79] B. Fraboni, A. Ciavatti, F. Merlo, L. Pasquini, A. Cavallini, A. Quaranta, A. Bonfiglio, and A. Fraleoni-Morgera, "Organic semiconducting single crystals as next generation of low-cost, room-temperature electrical x-ray detectors," *Advanced Materials*, vol. 24, no. 17, pp. 2289–2293, 2012. [Online]. Available: <https://onlinelibrary.wiley.com/doi/abs/10.1002/adma.201200283>
- [80] I. Temiño, L. Basiricò, I. Fratelli, A. Tamayo, A. Ciavatti, M. Mas-Torrent, and B. Fraboni, "Morphology and mobility as tools to control and unprecedentedly enhance x-ray sensitivity in organic thin-films," *Nature Communications*, vol. 11, p. 2136, 05 2020.
- [81] F. Zanderigo, S. Ferrari, G. Queirolo, C. Pello, and M. Borgini, "Quantitative tof-sims analysis of metal contamination on silicon wafers," *Materials Science and Engineering: B*, vol. 73, no. 1, pp. 173–177, 2000. [Online]. Available: <https://www.sciencedirect.com/science/article/pii/S0921510799004560>
- [82] J. Li, E. Colantoni, I. Temiño, P. Branchini, L. Tortora, and M. Mas-Torrent, "Dopant diffusion inhibition in organic field-effect transistors using organic semiconductor/high-molecular-weight polymer blends," *Chemistry of Materials*, vol. 35, no. 4, pp. 1527–1536, 2023. [Online]. Available: <https://doi.org/10.1021/acs.chemmater.2c02780>
- [83] S. Van Nuffel, "Three-dimensional time-of-flight secondary ion mass spectrometry imaging of primary neuronal cell cultures," Ph.D. dissertation, 07 2017.
- [84] S. Schwarz, "Secondary ion mass spectroscopy," in *Encyclopedia of Materials: Science and Technology*, K. J. Buschow, R. W. Cahn, M. C. Flemings, B. Iilschner, E. J. Kramer, S. Mahajan, and P. Veysseyre, Eds. Oxford: Elsevier, 2001, pp. 8283–8290. [Online]. Available: <https://www.sciencedirect.com/science/article/pii/B0080431526014820>
- [85] R. W. Welker, "Chapter 4 - size analysis and identification of particles," in *Developments in Surface Contamination and Cleaning*, R. Kohli and K. Mittal, Eds. Oxford: William Andrew Publishing, 2012, pp. 179–213. [Online]. Available: <https://www.sciencedirect.com/science/article/pii/B9781437778830000043>
- [86] V. Mazel and P. Richardin, *ToF-SIMS Study of Organic Materials in Cultural Heritage: Identification and Chemical Imaging*, 10 2009, pp. 433 – 457.
- [87] G. Ziegler and H. Hutter, "Correction of topographic artefacts of tof-sims element distributions," *Surface and Interface Analysis*, vol. 45, no. 1, pp. 457–460, 2013. [Online]. Available: <https://analyticalsciencejournals.onlinelibrary.wiley.com/doi/abs/10.1002/sia.5127>
- [88] W. Eckstein, *Sputtering Yields*, 07 2007, vol. 82, pp. 33–187.
- [89] P. Sigmund, "Mechanisms and theory of physical sputtering by particle impact," *Nuclear Instruments and Methods in Physics Research Section B: Beam Interactions with Materials and Atoms*, vol. 27, no. 1, pp. 1–20, 1987. [Online]. Available: <https://www.sciencedirect.com/science/article/pii/0168583X87900048>

- [90] W. Gerhard and C. Plog, "Secondary ion emission by nonadiabatic dissociation of nascent ion molecules with energies depending on solid composition," *Zeitschrift für Physik B Condensed Matter*, vol. 54, pp. 59–70, 1983. [Online]. Available: <https://api.semanticscholar.org/CorpusID:119547750>
- [91] R. Cooks and K. Busch, "Matrix effects, internal energies and ms/ms spectra of molecular ions sputtered from surfaces," *International Journal of Mass Spectrometry and Ion Physics*, vol. 53, pp. 111–124, 1983. [Online]. Available: <https://www.sciencedirect.com/science/article/pii/0020738183851067>
- [92] A. Benninghoven, "The analysis of monomolecular layers of solids by secondary ion emission." *Z. Phys.* 230: 403-17(1970)., 1 1970. [Online]. Available: <https://www.osti.gov/biblio/4754683>
- [93] ———, "Analysis of submonolayers on silver by negative secondary ion emission," *physica status solidi (b)*, vol. 34, no. 2, pp. K169–K171, 1969. [Online]. Available: <https://onlinelibrary.wiley.com/doi/abs/10.1002/pssb.19690340267>
- [94] T. Sarkar, E. Stein, J. Vinokur, and G. Frey, "Universal electrode for ambipolar charge injection in organic electronic devices," *Materials Horizons*, vol. 9, 05 2022.
- [95] L. Tortora, M. Urbini, A. Fabbri, P. Branchini, L. Mariucci, M. Rapisarda, M. Barra, F. Chiarella, A. Cassinese, F. Di Capua, and A. Aloisio, "Three-dimensional characterization of otft on modified hydrophobic flexible polymeric substrate by low energy cs+ ion sputtering," *Applied Surface Science*, vol. 448, pp. 628–635, 2018. [Online]. Available: <https://www.sciencedirect.com/science/article/pii/S0169433218310572>
- [96] J. Brison, S. Muramoto, and D. G. Castner, "Tof-sims depth profiling of organic films: A comparison between single-beam and dual-beam analysis," *The Journal of Physical Chemistry C*, vol. 114, no. 12, pp. 5565–5573, 2010, PMID: 20383274. [Online]. Available: <https://doi.org/10.1021/jp9066179>
- [97] A. M. Kia, N. Haufe, S. Esmaili, C. Mart, M. Utriainen, R. L. Puurunen, and W. Weinreich, "Tof-sims 3d analysis of thin films deposited in high aspect ratio structures via atomic layer deposition and chemical vapor deposition," *Nanomaterials*, vol. 9, no. 7, 2019. [Online]. Available: <https://www.mdpi.com/2079-4991/9/7/1035>
- [98] C. Guyot, J.-P. Barnes, O. Renault, and T. Maindron, "Time-of-flight secondary ion mass spectrometry and x-ray photoelectron spectroscopy protocol for the analysis of organic multilayers," *Surface and Interface Analysis*, vol. n/a, no. n/a. [Online]. Available: <https://analyticalsciencejournals.onlinelibrary.wiley.com/doi/abs/10.1002/sia.7277>
- [99] K. E. Mayerhofer, J. Heier, Y. Maniglio, and B. A. Keller, "Three dimensional analysis of self-structuring organic thin films using time-of-flight secondary ion mass spectrometry," *Thin Solid Films*, vol. 519, no. 18, pp. 6183–6189, 2011. [Online]. Available: <https://www.sciencedirect.com/science/article/pii/S0040609011008303>
- [100] G. Trindade, M.-L. Abel, and J. Watts, "simsuva: A tool for multivariate analysis of tof-sims datasets," *Chemometrics and Intelligent Laboratory Systems*, vol. 182, 10 2018.

- [101] D. J. Graham, M. S. Wagner, and D. G. Castner, "Information from complexity: Challenges of tof-sims data interpretation," *Applied Surface Science*, vol. 252, pp. 6860–6868, 2006. [Online]. Available: <https://api.semanticscholar.org/CorpusID:27475734>
- [102] H. Ebata, T. Izawa, E. Miyazaki, K. Takimiya, M. Ikeda, H. Kuwabara, and T. Yui, "Highly soluble [1]benzothieno[3,2-b]benzothiophene (btbt) derivatives for high-performance, solution-processed organic field-effect transistors," *Journal of the American Chemical Society*, vol. 129, no. 51, pp. 15 732–15 733, 2007, pMID: 18044892. [Online]. Available: <https://doi.org/10.1021/ja074841i>
- [103] T. Mori, T. Nishimura, T. Yamamoto, I. Doi, E. Miyazaki, I. Osaka, and K. Takimiya, "Consecutive thiophene-annulation approach to -extended thienoacene-based organic semiconductors with [1]benzothieno[3,2-b][1]benzothiophene (btbt) substructure," *Journal of the American Chemical Society*, vol. 135, no. 37, pp. 13 900–13 913, 2013, pMID: 24010738. [Online]. Available: <https://doi.org/10.1021/ja406257u>
- [104] D. He, J. Qiao, L. Zhang, J. Wang, T. Lan, J. Qian, Y. Li, Y. Shi, Y. Chai, W. Lan, L. K. Ono, Y. Qi, J.-B. Xu, W. Ji, and X. Wang, "Ultrahigh mobility and efficient charge injection in monolayer organic thin-film transistors on boron nitride," *Science Advances*, vol. 3, no. 9, p. e1701186, 2017. [Online]. Available: <https://www.science.org/doi/abs/10.1126/sciadv.1701186>
- [105] J. Soeda, Y. Hirose, M. Yamagishi, A. Nakao, T. Uemura, K. Nakayama, M. Uno, Y. Nakazawa, K. Takimiya, and J. Takeya, "Solution-crystallized organic field-effect transistors with charge-acceptor layers: High-mobility and low-threshold-voltage operation in air," *Advanced Materials*, vol. 23, no. 29, pp. 3309–3314, 2011. [Online]. Available: <https://onlinelibrary.wiley.com/doi/abs/10.1002/adma.201101027>
- [106] A. F. Paterson, Y.-H. Lin, A. D. Mottram, Z. Fei, M. R. Niazi, A. R. Kirmani, A. Amassian, O. Solomeshch, N. Tessler, M. Heeney, and T. D. Anthopoulos, "The impact of molecular p-doping on charge transport in high-mobility small-molecule/polymer blend organic transistors," *Advanced Electronic Materials*, vol. 4, no. 10, p. 1700464, 2018. [Online]. Available: <https://onlinelibrary.wiley.com/doi/abs/10.1002/aelm.201700464>
- [107] Y. Kim, S. Chung, K. Cho, D. Harkin, W.-T. Hwang, D. Yoo, J.-K. Kim, W. Lee, Y. Song, H. Ahn, Y. Hong, H. Sirringhaus, K. Kang, and T. Lee, "Enhanced charge injection properties of organic field-effect transistor by molecular implantation doping," *Advanced Materials*, vol. 31, no. 10, p. 1806697, 2019. [Online]. Available: <https://onlinelibrary.wiley.com/doi/abs/10.1002/adma.201806697>
- [108] Y. Kim, K. Broch, W. Lee, H. Ahn, J. Lee, D. Yoo, J. Kim, S. Chung, H. Sirringhaus, K. Kang, and T. Lee, "Highly stable contact doping in organic field effect transistors by dopant-blockade method," *Advanced Functional Materials*, vol. 30, no. 28, p. 2000058, 2020. [Online]. Available: <https://onlinelibrary.wiley.com/doi/abs/10.1002/adfm.202000058>
- [109] T. Minari, P. Darmawan, C. Liu, Y. Li, Y. Xu, and K. Tsukagoshi, "Highly enhanced charge injection in thienoacene-based organic field-effect transistors with chemically

- doped contact,” *Applied Physics Letters*, vol. 100, no. 9, p. 093303, 02 2012. [Online]. Available: <https://doi.org/10.1063/1.3690949>
- [110] I. E. Jacobs and A. J. Moulé, “Controlling molecular doping in organic semiconductors,” *Advanced Materials*, vol. 29, no. 42, p. 1703063, 2017. [Online]. Available: <https://onlinelibrary.wiley.com/doi/abs/10.1002/adma.201703063>
- [111] Y. Xu, H. Sun, A. Liu, H.-H. Zhu, W. Li, Y.-F. Lin, and Y.-Y. Noh, “Doping: A key enabler for organic transistors,” *Advanced Materials*, vol. 30, no. 46, p. 1801830, 2018. [Online]. Available: <https://onlinelibrary.wiley.com/doi/abs/10.1002/adma.201801830>
- [112] I. Temiño, F. G. Del Pozo, M. R. Ajayakumar, S. Galindo, J. Puigdollers, and M. Mas-Torrent, “A rapid, low-cost, and scalable technique for printing state-of-the-art organic field-effect transistors,” *Advanced Materials Technologies*, vol. 1, no. 5, p. 1600090, 2016. [Online]. Available: <https://onlinelibrary.wiley.com/doi/abs/10.1002/admt.201600090>
- [113] K. Pei, A. H. Y. Lau, and P. K. L. Chan, “Understanding molecular surface doping of large bandgap organic semiconductors and overcoming the contact/access resistance in organic field-effect transistors,” *Phys. Chem. Chem. Phys.*, vol. 22, pp. 7100–7109, 2020. [Online]. Available: <http://dx.doi.org/10.1039/D0CP00487A>
- [114] J. Li, A. Babuji, I. Temiño, T. Salzillo, F. D’Amico, R. Pfattner, C. Ocal, E. Barrena, and M. Mas-Torrent, “Chemical doping of the organic semiconductor c8-btbt-c8 using an aqueous iodine solution for device mobility enhancement,” *Advanced Materials Technologies*, vol. 7, no. 8, p. 2101535, 2022. [Online]. Available: <https://onlinelibrary.wiley.com/doi/abs/10.1002/admt.202101535>
- [115] M. Waldrip, O. D. Jurchescu, D. J. Gundlach, and E. G. Bittle, “Contact resistance in organic field-effect transistors: Conquering the barrier,” *Advanced Functional Materials*, vol. 30, no. 20, p. 1904576, 2020. [Online]. Available: <https://onlinelibrary.wiley.com/doi/abs/10.1002/adfm.201904576>
- [116] A. Tamayo, I. Fratelli, A. Ciavatti, C. Martínez-Domingo, P. Branchini, E. Colantoni, S. De Rosa, L. Tortora, A. Contillo, R. Santiago, S. T. Bromley, B. Fraboni, M. Mas-Torrent, and L. Basiricò, “X-ray detectors with ultrahigh sensitivity employing high performance transistors based on a fully organic small molecule semiconductor/polymer blend active layer,” *Advanced Electronic Materials*, vol. 8, no. 10, p. 2200293, 2022. [Online]. Available: <https://onlinelibrary.wiley.com/doi/abs/10.1002/aelm.202200293>
- [117] H. Hasegawa, T. Ohta, K. Ito, and H. Yokoyama, “Stress-strain measurement of ultra-thin polystyrene films: Film thickness and molecular weight dependence of crazing stress,” *Polymer*, vol. 123, pp. 179–183, 2017. [Online]. Available: <https://www.sciencedirect.com/science/article/pii/S0032386117306778>
- [118] R. Hamilton, J. Smith, S. Ogier, M. Heeney, J. E. Anthony, I. McCulloch, J. Veres, D. D. C. Bradley, and T. D. Anthopoulos, “High-performance polymer-small molecule blend organic transistors,” *Advanced Materials*, vol. 21, no. 10-11, pp. 1166–1171, 2009. [Online]. Available: <https://onlinelibrary.wiley.com/doi/abs/10.1002/adma.200801725>

- [119] W. H. Lee, J. A. Lim, D. Kwak, J. H. Cho, H. S. Lee, H. H. Choi, and K. Cho, "Semiconductor-dielectric blends: A facile all solution route to flexible all-organic transistors," *Advanced Materials*, vol. 21, no. 42, pp. 4243–4248, 2009. [Online]. Available: <https://onlinelibrary.wiley.com/doi/abs/10.1002/adma.200900277>
- [120] S. Riera-Galindo, F. Leonardi, R. Pfattner, and M. Mas-Torrent, "Organic semiconductor/polymer blend films for organic field-effect transistors," *Advanced Materials Technologies*, vol. 4, no. 9, p. 1900104, 2019. [Online]. Available: <https://onlinelibrary.wiley.com/doi/abs/10.1002/admt.201900104>
- [121] Y. Xu, C. Liu, D. Khim, and Y.-Y. Noh, "Development of high-performance printed organic field-effect transistors and integrated circuits," *Phys. Chem. Chem. Phys.*, vol. 17, pp. 26 553–26 574, 2015. [Online]. Available: <http://dx.doi.org/10.1039/C4CP02413C>
- [122] M. Mas-Torrent and C. Rovira, "Novel small molecules for organic field-effect transistors: towards processability and high performance," *Chem. Soc. Rev.*, vol. 37, pp. 827–838, 2008. [Online]. Available: <http://dx.doi.org/10.1039/B614393H>
- [123] Y. Diao, L. Shaw, Z. Bao, and S. C. B. Mannsfeld, "Morphology control strategies for solution-processed organic semiconductor thin films," *Energy Environ. Sci.*, vol. 7, pp. 2145–2159, 2014. [Online]. Available: <http://dx.doi.org/10.1039/C4EE00688G>
- [124] M. Khan Niazi, R. Li, E. Li, A. Kirmani, M. Abdelsamie, Q. Wang, W. Pan, M. Payne, J. Anthony, D.-M. Smilgies, S. Thoroddsen, E. Giannelis, and A. Amassian, "Solution-printed organic semiconductor blends exhibiting transport properties on par with single crystals," *Nature Communications*, vol. 6, p. 8598, 11 2015.
- [125] Y. Yuan, G. Giri, A. Ayzner, A. Zoombelt, S. Mannsfeld, J. Chen, D. Nordlund, M. Toney, J. Huang, and Z. Bao, "Ultra-high mobility transparent organic thin film transistors grown by an off-centre spin-coating method," *Nature communications*, vol. 5, p. 3005, 01 2014.
- [126] T. Ohe, M. Kuribayashi, R. Yasuda, A. Tsuboi, K. Nomoto, K. Satori, M. Itabashi, and J. Kasahara, "Solution-processed organic thin-film transistors with vertical nanophase separation," *Applied Physics Letters*, vol. 93, no. 5, p. 053303, 08 2008. [Online]. Available: <https://doi.org/10.1063/1.2966350>
- [127] N. Shin, J. Kang, L. J. Richter, V. M. Prabhu, R. J. Kline, D. A. Fischer, D. M. DeLongchamp, M. F. Toney, S. K. Satija, D. J. Gundlach, B. Purushothaman, J. E. Anthony, and D. Y. Yoon, "Vertically segregated structure and properties of small molecule–polymer blend semiconductors for organic thin-film transistors," *Advanced Functional Materials*, vol. 23, no. 3, pp. 366–376, 2013. [Online]. Available: <https://onlinelibrary.wiley.com/doi/abs/10.1002/adfm.201201389>
- [128] F. G. del Pozo, S. Fabiano, R. Pfattner, S. Georgakopoulos, S. Galindo, X. Liu, S. Braun, M. Fahlman, J. Veciana, C. Rovira, X. Crispin, M. Berggren, and M. Mas-Torrent, "Single crystal-like performance in solution-coated thin-film organic field-effect transistors," *Advanced Functional Materials*, vol. 26, no. 14, pp. 2379–2386, 2016. [Online]. Available: <https://onlinelibrary.wiley.com/doi/abs/10.1002/adfm.201502274>

- [129] A. Tamayo, S. Hofer, T. Salzillo, C. Ruzié, G. Schweicher, R. Resel, and M. Mas-Torrent, "Mobility anisotropy in the herringbone structure of asymmetric ph-btbt-10 in solution sheared thin film transistors," *J. Mater. Chem. C*, vol. 9, pp. 7186–7193, 2021. [Online]. Available: <http://dx.doi.org/10.1039/D1TC01288F>
- [130] J. Lee, Y. Seo, Y. Park, J. Anthony, D. Kwak, J. Lim, S. Ko, H. Jang, K. Cho, and W. Lee, "Effect of crystallization modes in tips-pentacene/insulating polymer blends on the gas sensing properties of organic field-effect transistors," *Scientific Reports*, vol. 9, 01 2019.
- [131] T. Salzillo, N. Montes, R. Pfattner, and M. Mas-Torrent, "Selection of the two enantiotropic polymorphs of dif-tes-adt in solution sheared thin film transistors," *J. Mater. Chem. C*, vol. 8, pp. 15 361–15 367, 2020. [Online]. Available: <http://dx.doi.org/10.1039/D0TC03222K>
- [132] M. R. Niazi, R. Li, M. Abdelsamie, K. Zhao, D. H. Anjum, M. M. Payne, J. Anthony, D.-M. Smilgies, and A. Amassian, "Contact-induced nucleation in high-performance bottom-contact organic thin film transistors manufactured by large-area compatible solution processing," *Advanced Functional Materials*, vol. 26, no. 14, pp. 2371–2378, 2016. [Online]. Available: <https://onlinelibrary.wiley.com/doi/abs/10.1002/adfm.201502428>
- [133] D. Gundlach, J. Royer, S. Park, S. Subramanian, O. Jurchescu, B. Hamadani, A. Moad, R. Kline, L. Teague, O. Kirillov, C. Richter, J. Kushmerick, L. Richter, S. Parkin, T. Jackson, and J. Anthony, "Contact-induced crystallinity for high-performance soluble acene-based transistors and circuits," *Nature Materials*, vol. 7, pp. 216–221, 02 2008.
- [134] G. R. Llorente, M.-B. Dufourg-Madec, D. J. Crouch, R. G. Pritchard, S. Ogier, and S. G. Yeates, "High performance, acene-based organic thin film transistors," *Chem. Commun.*, pp. 3059–3061, 2009. [Online]. Available: <http://dx.doi.org/10.1039/B901448A>
- [135] J.-F. Chang, T. Sakanoue, Y. Olivier, T. Uemura, M.-B. Dufourg-Madec, S. G. Yeates, J. Cornil, J. Takeya, A. Troisi, and H. Sirringhaus, "Hall-effect measurements probing the degree of charge-carrier delocalization in solution-processed crystalline molecular semiconductors," *Phys. Rev. Lett.*, vol. 107, p. 066601, Aug 2011. [Online]. Available: <https://link.aps.org/doi/10.1103/PhysRevLett.107.066601>
- [136] S. Illig, A. Eggeman, A. Troisi, L. Jiang, C. Warwick, M. Nikolka, G. Schweicher, S. Yeates, Y. Geerts, J. Anthony, and H. Sirringhaus, "Reducing dynamic disorder in small-molecule organic semiconductors by suppressing large-amplitude thermal motions," *Nature Communications*, vol. 7, p. 10736, 02 2016.
- [137] S. Riera-Galindo, A. Tamayo, and M. Mas-Torrent, "Role of polymorphism and thin-film morphology in organic semiconductors processed by solution shearing," *ACS Omega*, vol. 3, pp. 2329–2339, 02 2018.
- [138] H. Chung and Y. Diao, "Polymorphism as an emerging design strategy for high performance organic electronics," *J. Mater. Chem. C*, vol. 4, pp. 3915–3933, 2016. [Online]. Available: <http://dx.doi.org/10.1039/C5TC04390E>

- [139] R. Pfattner, S. T. Bromley, C. Rovira, and M. Mas-Torrent, "Tuning crystal ordering, electronic structure, and morphology in organic semiconductors: Tetrathiafulvalenes as a model case," *Advanced Functional Materials*, vol. 26, no. 14, pp. 2256–2275, 2016. [Online]. Available: <https://onlinelibrary.wiley.com/doi/abs/10.1002/adfm.201502446>
- [140] G. Schweicher, V. Lemaur, C. Niebel, C. Ruzié, Y. Diao, O. Goto, W.-Y. Lee, Y. Kim, J.-B. Arlin, J. Karpinska, A. R. Kennedy, S. R. Parkin, Y. Olivier, S. C. B. Mannsfeld, J. Cornil, Y. H. Geerts, and Z. Bao, "Bulky end-capped [1]benzothieno[3,2-b]benzothiophenes: Reaching high-mobility organic semiconductors by fine tuning of the crystalline solid-state order," *Advanced Materials*, vol. 27, no. 19, pp. 3066–3072, 2015. [Online]. Available: <https://onlinelibrary.wiley.com/doi/abs/10.1002/adma.201500322>
- [141] P. J. Skabara, J.-B. Arlin, and Y. H. Geerts, "Close encounters of the 3d kind – exploiting high dimensionality in molecular semiconductors," *Advanced Materials*, vol. 25, no. 13, pp. 1948–1954, 2013. [Online]. Available: <https://onlinelibrary.wiley.com/doi/abs/10.1002/adma.201200862>
- [142] G. R. Llorente, M.-B. Dufourg-Madec, D. J. Crouch, R. G. Pritchard, S. Ogier, and S. G. Yeates, "High performance, acene-based organic thin film transistors," *Chem. Commun.*, pp. 3059–3061, 2009. [Online]. Available: <http://dx.doi.org/10.1039/B901448A>
- [143] K. L. McCall, S. R. Rutter, E. L. Bone, N. D. Forrest, J. S. Bissett, J. D. E. Jones, M. J. Simms, A. J. Page, R. Fisher, B. A. Brown, and S. D. Ogier, "High performance organic transistors using small molecule semiconductors and high permittivity semiconducting polymers," *Advanced Functional Materials*, vol. 24, no. 20, pp. 3067–3074, 2014. [Online]. Available: <https://onlinelibrary.wiley.com/doi/abs/10.1002/adfm.201303336>
- [144] J. Chang, T. Sakanoue, Y. Olivier, T. Uemura, M. Dufourg-Madec, S. Yeates, J. Cornil, J. Takeya, A. Troisi, and H. Sirringhaus, "Hall-effect measurements probing the degree of charge-carrier delocalization in solution-processed crystalline molecular semiconductors," *Physical Review Letters*, vol. 107, no. 6, Aug. 2011.
- [145] M. Ibrahim, A. Maciel, C. Watson, M.-B. Madec, S. Yeates, and D. Taylor, "Thermomechanical stabilisation of a crystalline organic semiconductor for robust large area electronics," *Organic Electronics*, vol. 11, no. 7, pp. 1234–1241, 2010. [Online]. Available: <https://www.sciencedirect.com/science/article/pii/S1566119910001606>
- [146] A. Y. B. Meneau, Y. Olivier, T. Backlund, M. James, D. W. Breiby, J. W. Andreasen, and H. Sirringhaus, "Temperature dependence of charge localization in high-mobility, solution-crystallized small molecule semiconductors studied by charge modulation spectroscopy," *Advanced Functional Materials*, vol. 26, no. 14, pp. 2326–2333, 2016. [Online]. Available: <https://onlinelibrary.wiley.com/doi/abs/10.1002/adfm.201502502>
- [147] L. Basiricò, A. Ciavatti, T. Cramer, P. Cosseddu, A. Bonfiglio, and B. Fraboni, "Direct x-ray photoconversion in flexible organic thin film devices operated below 1 v," *Nature Communications*, vol. 7, 10 2016.
- [148] Y. Gao, Y. Ge, X. Wang, J. Liu, W. Liu, Y. Cao, K. Gu, Z. Guo, Y.-M. Wei, N. Zhou, D. Yu, H. Meng, X.-F. Yu, H. Zheng, W. Huang, and J. Li, "Ultrathin

- and ultrasensitive direct x-ray detector based on heterojunction phototransistors,” *Advanced Materials*, vol. 33, no. 32, p. 2101717, 2021. [Online]. Available: <https://onlinelibrary.wiley.com/doi/abs/10.1002/adma.202101717>
- [149] F. Smith, *Industrial applications of X-ray diffraction*. CRC press, 1999.
- [150] B. Milbrath, A. Peurrung, M. Bliss, and W. Weber, “Radiation detector materials: An overview,” *Journal of Materials Research*, vol. 23, 10 2008.
- [151] P. Zygmanski, C. Abkai, Z. Han, Y. Shulevich, D. Menichelli, and J. Hesser, “Low-cost flexible thin-film detector for medical dosimetry applications,” *Journal of Applied Clinical Medical Physics*, vol. 15, no. 2, pp. 311–326, 2014. [Online]. Available: <https://aapm.onlinelibrary.wiley.com/doi/abs/10.1120/jacmp.v15i2.4454>
- [152] M. Kabir and S. Kasap, *Photoconductors for X-Ray Image Detectors*, 01 2017, pp. 1–1.
- [153] A. Intaniwet, J. Keddie, M. Shkunov, and P. Sellin, “High charge-carrier mobilities in blends of poly(triarylamine) and tips-pentacene leading to better performing x-ray sensors,” *Organic Electronics - ORG ELECTRON*, vol. 12, pp. 1903–1908, 11 2011.
- [154] B. Fraboni, A. Fraleoni-Morgera, and N. Zaitseva, “Ionizing radiation detectors based on solution-grown organic single crystals,” *Advanced Functional Materials*, vol. 26, no. 14, pp. 2276–2291, 2016. [Online]. Available: <https://onlinelibrary.wiley.com/doi/abs/10.1002/adfm.201502669>
- [155] M. J. Griffith, S. Cottam, J. Stamenkovic, J. A. Posar, and M. Petasecca, “Printable organic semiconductors for radiation detection: from fundamentals to fabrication and functionality,” *Frontiers in Physics*, vol. 8, p. 22, 2020.
- [156] S. Calvi, L. Basiricò, S. M. Carturan, I. Fratelli, A. Valletta, A. Aloisio, S. De Rosa, F. Pino, M. Campajola, A. Ciavatti, L. Tortora, M. Rapisarda, S. Moretto, M. Verdi, S. Bertoldo, O. Cesarini, P. Meo, M. Chiari, F. Tommasino, and B. Fraboni, “Flexible fully organic indirect detector for megaelectronvolts proton beams,” *npj Flexible Electronics*, vol. 7, p. 5, 02 2023.
- [157] H. Koezuka, A. Tsumura, and T. Ando, “Field-effect transistor with polythiophene thin film,” *Synthetic Metals*, vol. 18, no. 1, pp. 699–704, 1987, proceedings of the International Conference of Science and Technology of Synthetic Metals. [Online]. Available: <https://www.sciencedirect.com/science/article/pii/0379677987909647>
- [158] S. Lai, P. Cosseddu, L. Basiricò, A. Ciavatti, B. Fraboni, and A. Bonfiglio, “A highly sensitive, direct x-ray detector based on a low-voltage organic field-effect transistor,” *Advanced Electronic Materials*, vol. 3, no. 8, p. 1600409, 2017. [Online]. Available: <https://onlinelibrary.wiley.com/doi/abs/10.1002/aelm.201600409>
- [159] M. Kabir and S. Kasap, *Photoconductors for X-Ray Image Detectors*, 01 2017, pp. 1–1.

-
- [160] L. Basiricò, A. Ciavatti, and B. Fraboni, “Solution-grown organic and perovskite x-ray detectors: A new paradigm for the direct detection of ionizing radiation,” *Advanced Materials Technologies*, vol. 6, no. 1, p. 2000475, 2021. [Online]. Available: <https://onlinelibrary.wiley.com/doi/abs/10.1002/admt.202000475>
- [161] L. Janasz, M. Borkowski, P. W. M. Blom, T. Marszalek, and W. Pisula, “Organic semiconductor/insulator blends for elastic field-effect transistors and sensors,” *Advanced Functional Materials*, vol. 32, no. 7, p. 2105456, 2022. [Online]. Available: <https://onlinelibrary.wiley.com/doi/abs/10.1002/adfm.202105456>

Acknowledgements

Thinking about these three years, so intensive, remarkable, challenging, and satisfying, I feel a deep sense of gratitude towards those who have been part of this journey. This experience, both professionally and personally, has been incredibly educational and I want to mention those who have guided, supported, and inspired me along the way.

First and foremost, my deepest gratitude to my advisor, Dr. Paolo Branchini, and to my co-advisor Dr. Luca Tortora, for your invaluable guidance, unwavering support, and insightful advice throughout my Ph.D. Your expertise and mentorship shaped my research path. Thank you for your constant mentorship in Rome, as well as for the opportunity to work with other national and international research groups.

Special thanks to Prof. Gianlorenzo Bussetti, who hosted me at the SoLINano laboratory at Politecnico di Milano. Your constant encouragement and support have been really important in learning and discovering the deep sense of scientific research.

I am deeply grateful to Prof. Marta Mas-Torrent for welcoming me into her laboratory and her group at eMolMat in Barcelona. Collaboration with you and your international team, out of my comfort zone, was powerful to broaden my horizons and to interact with an open and exciting environment. In particular, I would like to thank Carme, Betty, Maria, and Dean, who have always helped me. The knowledge and skills I gained through my interactions with each of you have been invaluable, contributing greatly to my development.

I would also like to express my sincere thanks to Prof. Beatrice Fraboni, Dr. Laura Basiricò, and Dr. Ilaria Fratelli for your collaboration, which marked the beginning as well as the ending of my Ph.D. journey. The meetings and discussions with you have opened my eyes to the world of applications of OFETs devices as detectors.

I wish to extend my deep gratitude to all my fellow travelers. A special mention goes to my office colleague, Matteo and Nina, without you these three years would not have been the same. Your presence and support have been a constant source of joy and motivation.

I am also profoundly grateful to all the members of the LASR3 laboratory at Roma Tre University, you have been an integral part of this experience. Your friendship and support

have lightened the difficult moments and turned achievements into celebrations. The sense of community and mutual support we shared in the lab has been invaluable.

Last but certainly not least, a special thanks to Dr. Stefania De Rosa and Dr. Giacomo De Pietro. Your professionalism, dedication, and insights have been not only an example to inspire to but also a guiding light throughout my journey.

Thank you all again, each one of you has left an indelible mark on my life, both professionally and personally, and for that, I am really grateful.